Early Detection of Cracking in Grapes under Field Conditions using Hyperspectral Imaging and Machine Learning

By Yovel Gani

Supervised by:

Dr. Alon Sela, Prof. Victor Alchanatis, Prof. Irad Ben-Gal

August 2026

A thesis submitted toward the degree of Master of Science (M.Sc.)

Abstract

Grape cracking is a severe physiological disorder that leads to significant economic losses in the viticulture industry by reducing marketable yield and increasing susceptibility to secondary infections like sour rot. Early and non-destructive assessment is critical for implementing preventative measures. This research explores the feasibility of using hyperspectral imaging (HSI; VNIR 400–1000 nm), coupled with machine learning, to detect and identify crack-related spectral signatures at the time of measurement under field conditions, including both early- and late-stage acquisitions (initial/minimal vs. advanced cracking). Throughout the thesis, all spectral analyses are restricted to 450–925 nm with per-spectrum Standard Normal Variate (SNV) normalization.

The study followed a multi-stage approach: initial identification, system-level field inference, and comparative analysis of spectral signatures. For the identification task, a pixel-level dataset was meticulously created by manually selecting and labeling pixels from healthy and cracked berries. An XGBoost classifier trained on these spectral signatures achieved outstanding performance, with an accuracy of approximately 97% and an AUC of 0.99, demonstrating that a distinct spectral difference exists between intact and cracked grape tissue.

However, applying this pixel-level model to whole-image segmentation proved challenging. The model produced noisy results, often misclassifying background elements such as plastic ties or dry twigs, which exhibited spectral signatures similar to those of decay associated with cracks. To address this gap between pixel-level signature discrimination and field-scene inference, the research developed a whole-image crack-detection pipeline. The approach aggregates pixel-level classifier outputs using spatial post-processing (thresholding, morphological filtering, and patch/blob-based decision rules) to obtain an image-level decision, and was evaluated separately under early- and late-stage acquisition conditions. System-level performance was reported with emphasis on the *Cracked* class, using $F1_{\mathrm{CRACK}}$ and MCC alongside precision and recall. On the held-out test row, the pipeline achieved $F1_{\mathrm{CRACK}}$=0.704 (MCC=0.504) under early-stage acquisition and $F1_{\mathrm{CRACK}}$=0.818 (MCC=0.598) under late-stage acquisition. In addition, wavelength-selection experiments quantify the extent to which crack-detection performance can be retained using reduced spectral-band subsets, supporting a pathway toward compact sensing configurations for field deployment.

Contents

1 Introduction **11**

1.1 The Problem of Fruit Cracking 11

1.2 Economic Impact 11

1.3 Research Motivation 11

1.3.1 Main Research Question 13

1.4 Research Objectives and Hypotheses 13

1.4.1 Research Objectives 13

1.4.2 Contributions 13

2 Literature Review **15**

2.1 Grape Cracking as an Agricultural and Physiological Problem 15

2.1.1 Definition and visual manifestation of fruit cracking 15

2.1.2 Phenological timing (veraison, late ripening stages) 15

2.1.3 Environmental and agronomic triggers 16

2.2 Economic Impact and Practical Consequences 16

2.2.1 Yield losses and reduction in marketable produce 16

2.2.2 Quality degradation and shelf-life reduction 16

2.2.3 Limitations of reactive management strategies 17

2.3 Physiological and Biomechanical Mechanisms of Grape Cracking 17

2.3.1 Berry water relations and turgor pressure dynamics 18

2.3.2 Cuticle structure, micro-cracks, and mechanical failure 18

2.3.3 Hormonal influences and agronomic interventions 19

2.3.4 Cultivar-dependent susceptibility and variability 19

2.3.5 Skin pathology as an indicator of structural instability 19

2.3.6 Summary 20

2.4 Precision Agriculture and Non-Destructive Sensing 20

2.4.1 Principles of precision agriculture and data-driven crop management 20

2.4.2 Role of proximal and remote sensing technologies 20

2.4.3 Limitations of conventional physiological measurements 21

2.4.4 Computer Vision and AI in Agriculture 21

2.5 Hyperspectral Imaging for Agricultural Applications 22
2.5.1 Fundamentals of Reflectance and Spectral Signatures 22
2.5.2 Spectral Imaging Modalities and the Electromagnetic Spectrum . 22
2.5.3 Advantages of Hyperspectral Imaging over RGB Imaging 24
2.5.4 VIS–NIR Sensitivity to Physiological and Structural Changes . . 24
2.5.5 Applications in Fruit Quality Assessment and Defect Detection . . 24
2.6 Machine Learning for Hyperspectral Data Analysis 25
2.6.1 Deep learning and non-linear models 26
2.6.2 Pixel-level versus image-level modeling paradigms 27
2.6.3 Challenges: class imbalance, background clutter, and generalization 28
2.7 Related Work on Fruit Defect Detection and Early-Stage Detection . . . 28
2.7.1 HSI-based detection of visible fruit defects 29
2.7.2 Attempts Toward Early and Pre-Symptomatic Defect Detection . 30
2.7.3 Limitations of Existing Approaches under Field Conditions 30
2.8 Research Gap and Study Positioning 32
2.8.1 Summary of Established Knowledge 32
2.8.2 Identified Methodological and Application Gaps 32
2.8.3 Lack of Early, Non-Destructive Crack Early-Warning Frameworks 33
2.8.4 Positioning of the Present Study within the Literature 33

3 Research Objectives and Hypotheses 35
3.1 Research Objectives 35
3.2 Research Hypotheses 35

4 Materials and Methods 38
4.1 Data Acquisition 38
4.1.1 Study Area and Experimental Design 38
4.1.2 Imaging Systems 40
4.1.3 Data Collection Protocol 43
4.1.4 Dataset Statistics 44
4.1.5 Pixel-Level Dataset Preparation 46
4.1.6 Expansion to Multi-Class Dataset 47
4.1.7 Whole-Image Dataset Construction and Experimental Design . . 48
4.2 Modeling and Evaluation Methodology 49
4.2.1 Global Spectral Preprocessing 50
4.2.2 Spectral Discriminability and Informative Wavelength Analysis . . 51
4.2.3 Pixel-Level Classification Framework 51
4.2.4 Anomaly Detection Framework 53
4.2.5 Dimensionality Reduction Strategy 55

4.2.6 Whole-Image Detection and Aggregation Pipeline 56
4.2.7 Evaluation Protocols and Performance Metrics 58
4.2.8 Reproducibility and Implementation Details 62

5 Experimental Results **64**
5.1 Overview of Experimental Results 64
5.1.1 Baselines 64
5.2 Spectral Signature Characterization 65
5.2.1 Mean Spectral Signatures of Healthy and Cracked Tissue 65
5.2.2 Spectral Separability Across Wavelength Regions 66
5.3 Pixel-Level Classification Performance 68
5.3.1 Experimental Setup and Evaluation Protocol 68
5.3.2 Binary Pixel-Level Classification Results 68
5.3.3 Pixel-Level Classification Results Under Different Labeling and Balancing Regimes (10 classes) 71
5.3.4 Autoencoder-Based Pixel-Level Anomaly Detection 74
5.3.5 Full-Image Inference: Early vs. Late Acquisition-Stage Experiments 81
5.3.6 Wavelength selection (BFS) setup 85
5.3.7 Full-image wavelength-selection results 86
5.3.8 BFS Wavelength-Selection Stability Analysis 88

6 Discussion **96**
6.1 Summary of Key Findings 96
6.1.1 Hypotheses Evaluation 97
6.2 Spectral and Physiological Interpretation 98
6.2.1 VIS Region: Pigments and Skin Integrity 98
6.2.2 NIR and Red-Edge Sensitivity to Water Stress 99
6.3 Why Pixel-Level Detection Works in Controlled Settings but Fails in Field Conditions 100
6.4 Spatial Aggregation as a Robust Strategy for Early-Stage Crack Detection 101
6.5 Feature Selection and Spectral Stability 103
6.5.1 Dimensionality Reduction via BFS 103
6.5.2 Stability Across Random Seeds and Sensor Design Implications . 104
6.6 Generalization Gaps Between Calibration and Test Sets 105
6.7 Supervised Classification versus Anomaly Detection 106
6.8 Practical Implications for Precision Viticulture 107
6.9 Limitations of the Study 109
6.10 Future Research Directions 111
6.11 Concluding Perspective 112

7 Conclusions and Future Work **113**
7.1 Summary of Main Contributions 113
7.2 Direct Answer to the Research Question 114
7.3 Validation of Research Hypotheses 115
7.4 Practical Implications and Applications 116
7.5 Limitations of the Study 118
7.6 Future Research Directions 119
7.6.1 Short-Term Extensions: Validation and Robustness 119
7.6.2 Medium-Term Opportunities: Multi-Modal Integration and Transfer Learning 120
7.6.3 Long-Term Vision: Autonomous Systems and Decision Support . 121
7.7 Final Concluding Statement 122

List of Figures

2.1 The formula for reflectance Blackburn, 2007. 22
2.2 Hyperspectral signature of barley grains with varying moisture content T. Sun et al., 2020. 23
2.3 Segments of the electromagnetic spectrum commonly used in hyperspectral imaging (Middleton Spectral Vision, n.d.). 23

4.1 Map of the experimental vineyard showing the five randomized blocks (A–E) and the four irrigation regimes applied within each block. 39
4.2 Hyperspectral imaging setup and data acquisition using the Specim IQ system under vineyard conditions. 40
4.3 Thermal imaging system and example thermal data acquired from grape clusters under vineyard conditions. 42
4.4 Graphical user interface of the HSI – RGB annotation tool. (1) Hyperspectral image visualized as an RGB composite with a SAM2-generated segmentation overlay, (2) wavelength-selectable grayscale HSI band with the same SAM2 segmentation mask, and (3) RGB image of the same grape cluster captured on the same day using a Canon EOS R5. (4) Spectral signature extracted from a single pixel within the SAM2-segmented region, and (5) autoencoder reconstruction of the same spectral signature, discussed later in this work. 46
4.5 Protocol overview for the row-based split, training and calibration on Row 1 Late-stage data, held-out evaluation on Row 2, and post-inference reporting stratified by acquisition stage. 49
4.6 Whole-image crack-detection pipeline applied to field-acquired cluster scenes (early and late settings) with row-partitioned evaluation (Row 1 calibration, Row 2 test). A pixel-level classifier produces a crack probability map ($[0, 1]$), which is spatially aggregated via morphological closing and blob-size filtering; patch rules are then combined into a final image-level decision (Cracked vs. Non-Cracked). Takeaway: spatial aggregation turns noisy pixel scores into a deployable cluster-level decision rule. 57

5.1 Mean spectral signatures (± standard deviation) for healthy and cracked tissue across the VIS–NIR range. 65
5.2 Wavelength-wise spectral separability metrics between healthy and cracked tissue, including absolute mean difference, Cohen's d, and Fisher score. . 67
5.3 Regional visual summary of mean reflectance (±1 STD) and absolute mean difference between healthy and cracked tissue in the VIS and NIR ranges. This figure provides an intuitive visualization of the regional trends quantified in Table 5.2. 67
5.4 Backward Feature Selection (BFS) trajectories for the full-image pipeline, plotted as CRACK-class PR–AUC (primary objective) and CRACK-class F1 versus the number of retained wavelengths (n, unitless count; full baseline n=159 over 450–925 nm). Y-axis metrics are unitless in $[0, 1]$. Takeaway: PR–AUC exhibits a broad near-optimal plateau, motivating reduced-band configurations. 85
5.5 BFS threshold-marker visualization on CRACK metrics, used to define representative reduced-band subset sizes. Markers indicate the maximum and the first n where performance falls more than 0.5% and 1.0% below that maximum (unitless drop). Takeaway: these markers operationalize "top-n" selection without introducing an arbitrary n. 86
5.6 Distribution and popularity of the top-30 selected wavelengths across five varying-split seeds. 90
5.7 Wavelength popularity at different bin sizes (1, 5, 10, 20 nm) for the top-30 subsets. 91
5.8 Stability heatmap for the top-30 BFS subsets across five varying-split seeds (objective: CRACK PR–AUC). The x-axis is wavelength binned at 5 nm; each cell value (0–5) indicates how many seeds selected at least one wavelength within that bin (unitless count). Takeaway: selection concentrates in a limited set of repeatable spectral regions, but exact channel identities vary across splits. 92
5.9 Wavelength selection frequency along the spectrum (2 nm sliding window) for the top-30 subsets. 93
5.10 Distribution and popularity of the top-11 selected wavelengths across five varying-split seeds. 93
5.11 Wavelength popularity at different bin sizes (1, 5, 10, 20 nm) for the top-11 subsets. 94

5.12 Stability heatmap for the top-11 BFS subsets across five varying-split seeds (objective: CRACK PR–AUC; 0.5% drop setting). The x-axis is wavelength binned at 5 nm; each cell value (0–5) indicates how many seeds selected a wavelength within that bin (unitless count). Takeaway: under aggressive reduction, only a small core of bins remains consistently selected across splits. 95
5.13 Wavelength selection frequency along the spectrum (2 nm sliding window) for the top-11 subsets. 95

List of Tables

1.1 Estimated financial losses from fruit cracking in major crops.(Alchanatis et al., 2022). 12

4.1 Pixel-level datasets. 44
4.2 Whole-image datasets. 44
4.3 Exact dataset statistics used in the experiments. For whole-image inference, Row 1 is used for calibration/tuning and Row 2 for held-out testing. 45
4.4 Pixel-level exports: dataset composition. 45
4.5 Multi-class pixel-level dataset: exported pixels by class. 45
4.6 Multi-class dataset: class definitions. 48
4.7 Autoencoder training hyperparameters. 54
4.8 Evaluation units and split strategy used across experiments. "Independent test" denotes the data that remain unseen during fitting/tuning for the corresponding protocol. 60
4.9 Evaluation metrics for pixel-level and anomaly detection experiments . . 61
4.10 Evaluation metrics for whole-image and patch-based detection 63

5.1 Summary statistics of reflectance values across spectral regions for healthy and cracked tissue. 66
5.2 Regional spectral separability metrics between healthy and cracked tissue. Mean values are averaged across wavelengths within each range, while peak values indicate the maximum separability and the corresponding wavelength. 66
5.3 Pixel-level classification metrics (unbalanced training set). Values are reported as mean ± standard deviation across folds where available. Precision/recall and ROC–AUC refer to the *Cracked* class (positive class); F1 is the weighted F1-score. 70
5.4 Pixel-level classification metrics (balanced training set). Values are reported as mean ± standard deviation across folds where available. Precision/recall and ROC–AUC refer to the *Cracked* class (positive class); F1 is the weighted F1-score. 70
5.5 Pixel-level classification metrics (**unbalanced** training set). Values are reported as mean ± standard deviation across folds. 72

5.6 Pixel-level classification metrics (**balanced** training set). Values are reported as mean ± standard deviation across folds. 73
5.7 Pixel-level anomaly detection performance using autoencoders trained on non-cracked samples (unbalanced sampling). Values are reported as mean ± standard deviation across folds. Accuracy is reported overall, while Precision/Recall/F1/ROC–AUC/PR–AUC correspond to the *Cracked* class (positive class). 76
5.8 Pixel-level anomaly detection performance using autoencoders trained on non-cracked samples (balanced sampling). Values are reported as mean ± standard deviation across folds. Accuracy is reported overall, while Precision/Recall/F1/ROC–AUC/PR–AUC correspond to the *Cracked* class (positive class). 76
5.9 Pixel-level anomaly detection performance using autoencoders trained exclusively on *Cracked* pixels and evaluated in a multi-class setting (unbalanced sampling). Values are reported as mean across LOGO folds. Accuracy is reported overall, while Precision/Recall/F1/ROC–AUC/PR–AUC correspond to the *Cracked* class (positive class). 78
5.10 Pixel-level anomaly detection performance using autoencoders trained exclusively on *Cracked* pixels and evaluated in a multi-class setting (balanced sampling). Values are reported as mean ± standard deviation across LOGO folds. Accuracy is reported overall, while Precision/Recall/F1/ROC–AUC/PR–AUC correspond to the *Cracked* class (positive class). 78
5.11 Pixel-level anomaly detection performance using autoencoders trained on all semantic classes except *Cracked* and evaluated in a multi-class setting (unbalanced sampling). Values are reported for the held-out test split. Accuracy is reported overall, while Precision/Recall/F1/ROC–AUC/PR–AUC correspond to the *Cracked* class (positive class). 80
5.12 Pixel-level anomaly detection performance using autoencoders trained on all semantic classes except *Cracked* and evaluated in a multi-class setting (balanced sampling). Values are reported for the held-out test split. Accuracy is reported overall, while Precision/Recall/F1/ROC–AUC/PR–AUC correspond to the *Cracked* class (positive class). 80
5.13 Dataset composition for full-image crack-detection experiments under early- and late-stage acquisition conditions (initial/minimal vs. advanced cracking). Row 1 was used for calibration, while Row 2 served as an independent test set. 82

5.14 Full-image crack detection performance for early- and late-stage acquisition experiments (initial/minimal vs. advanced cracking). Metrics are reported separately for calibration and test splits. Confusion-matrix entries correspond to the number of grape clusters classified as cracked or healthy. The main performance indicator is **F1 (Cracked)**. Accuracy, Balanced Accuracy and MCC are reported overall. Precision/Recall/F1/F2 refer to the *Cracked* class (positive class), while Specificity and NPV refer to the *Healthy* class (negative class). 83
5.15 Full-image crack detection using autoencoder-based anomaly detection (128–64–32, trained on *Cracked* pixels). Reconstruction errors (MSE) were converted to pseudo-probabilities via exponential decay, $p_{\text{CRACK}}(x) = \exp(-e(x)/\tau)$; the same post-processing pipeline (thresholding, morphological filtering, patch-based aggregation) was applied. Metrics are reported for calibration and test splits under early- and late-stage conditions. The main performance indicator is **F1 (Cracked)**. Accuracy, Balanced Accuracy and MCC are reported overall. Precision/Recall/F1/F2 refer to the *Cracked* class (positive class), while Specificity and NPV refer to the *Healthy* class (negative class). 84
5.16 Summary of BFS wavelength-count thresholds for CRACK metrics. . . . 86
5.17 Full-image crack-detection performance for different wavelength subsets under early- and late-stage conditions. 87
5.18 Model Generalization Analysis: Comparison between Calibration and Test MCC. 87
5.19 BFS stability: per-seed results under varying train/test splits. 89
5.20 Pairwise Jaccard similarity of top-30 wavelengths across seeds (varying split). Mean Jaccard = 0.493. 89
5.21 Pairwise Jaccard similarity of top-11 wavelengths across seeds (varying split). Mean Jaccard = 0.398. 89

Chapter 1

Introduction

1.1 The Problem of Fruit Cracking

Fruit cracking is a significant physiological disorder affecting a wide range of commercially important crops, including sweet cherries, tomatoes, pomegranates, and particularly table grapes (Vitis vinifera L.). The phenomenon is characterized by the rupture of the fruit's skin (cuticle and epidermis), exposing the internal flesh to the environment. These cracks render the fruit unmarketable and create entry points for pathogens, leading to rapid decay from secondary infections such as sour rot. Cracking typically occurs during the final stages of fruit ripening, a period when the fruit is most valuable. It is primarily caused by an imbalance between the turgor pressure within the fruit and the mechanical strength of its skin, a condition often exacerbated by environmental factors like rain, high humidity, and irrigation practices.

1.2 Economic Impact

The economic consequences of grape cracking are substantial. Direct losses can amount to up to 30% of the marketable yield. For table grapes, this translates to an estimated financial loss of €625 per ton, culminating in a total industry loss of approximately €175 million annually, based on European market data (Table 1.1). Beyond direct yield loss, cracking negatively impacts fruit appearance and quality, leading to price reductions of 20-50% and a shortened shelf-life, further diminishing profitability for growers.

1.3 Research Motivation

Current methods for managing cracking risk are reactive and often insufficient. There is a critical need for a non-destructive, reliable method to detect early signs of cracking susceptibility before visible fissures appear. Hyperspectral imaging (HSI) has emerged

Table 1.1: Estimated financial losses from fruit cracking in major crops.(Alchanatis et al., 2022).

Fruit	**Prod. (K t)**	**Coverage (K ha)**	**Price (€/kg)**	**Loss (%)**	**Fin. Loss (€/t)**	**Total loss (M€)**
Table grapes	280	7.0	2.5	25	625	175.0
Citrus	2300	58.5	1.1	20	220	506.0
Pomegranate	43	1.0	3.3	25	825	35.5
Sweet cherry	560	37.3	2.0	20	400	224.0

as a powerful tool in precision agriculture for assessing plant health and fruit quality due to its ability to capture detailed spectral information beyond the visible range. This research aims to investigate the potential of HSI and machine learning to address the challenge of grape cracking.

This thesis addresses two related but distinct analysis settings. *Identification/detection* concerns recognising existing crack tissue based on its hyperspectral signature and can be naturally posed as a pixel-level classification problem when representative labels are available. *Early-warning screening*, in contrast, targets pre-symptomatic field assessment under realistic vineyard conditions, where direct pixel-wise segmentation of complex scenes is often unstable: background clutter (e.g., leaves, wood, and artificial materials) and acquisition-dependent domain shifts (illumination, viewing geometry) can dominate individual pixel-level outputs and lead to unreliable image-level decisions. For this reason, the early-warning setting is approached through robust single-acquisition representations that aggregate information at the grape-cluster/image level. In particular, early-stage acquisitions are not a focal point for clear field identification because reliable field indicators are often not yet present, whereas late-stage acquisitions typically allow clearer field identification.

Terminology (Early vs. Late Acquisition). In this thesis, *detection/identification* refers to classification at the *time of measurement* using hyperspectral signatures (e.g., pixel-level crack identification and whole-image inference under early- vs. late-stage conditions). Here, *early* and *late* denote *acquisition-stage subsets relative to crack progression*: for a given grape/cluster identity, *early* corresponds to the first acquisition at which cracking is absent or only minimal/incipient (i.e., the first time a small crack is recorded), whereas *late* corresponds to acquisitions where cracking is advanced and macroscopically visible. These terms describe crack status at the time of measurement (and typically align with earlier- vs. later-season acquisition periods), not a future outcome.

1.3.1 Main Research Question

Can hyperspectral imaging and machine learning models be used to detect and identify cracking-related status at the time of measurement under field conditions, including both early- and late-stage acquisitions (initial/minimal vs. advanced cracking)?

1.4 Research Objectives and Hypotheses

1.4.1 Research Objectives

1. **Identification:** To develop a high-accuracy classification model to differentiate between healthy and cracked grape tissue at the pixel level using their hyperspectral signatures.

2. **Whole-image screening:** To develop and evaluate an image-level crack-detection pipeline by combining pixel-level inference with spatial aggregation and post-processing, and to assess performance under early- and late-stage acquisition conditions (initial/minimal vs. advanced cracking).

3. **Wavelength selection:** To quantify the performance–complexity trade-off of reduced spectral-band subsets and identify stable candidate wavelengths to support compact sensing configurations.

1.4.2 Contributions

The main contributions of this thesis are as follows:

- A consistent VIS–NIR preprocessing protocol was established and applied throughout the study by restricting spectra to 450–925 nm and using per-spectrum SNV normalization, enabling direct comparability across experiments.

- A field-acquired hyperspectral dataset was curated at both pixel and whole-image levels, including manual pixel labeling and full-scene vineyard acquisitions, and was used to benchmark supervised classifiers under leave-one-group-out protocols and row-separated calibration/test evaluation, demonstrating reliable crack discrimination at the spectral-signature level (Chapter 5, Section 5.3).

- The limits of direct pixel-level segmentation in realistic vineyard scenes were analyzed by tracing error sources such as mixed pixels, illumination/BRDF effects, and spectrally confounding background materials, motivating a shift toward spatial aggregation (Chapter 6, Section 6.3).

- A whole-image crack-detection pipeline was developed by combining pixel-level inference with probability thresholding, morphological filtering, and patch/blob-based aggregation, with post-processing parameters optimized on calibration data and evaluated under early- vs. late-stage acquisition conditions (initial/minimal vs. advanced cracking; Chapter 5, Section 5.3.5).
- Backward Feature Selection (BFS) was used to quantify the performance–complexity trade-off of wavelength reduction and to assess selection stability across random seeds, providing a basis for compact band subsets and sensor-design implications (Chapter 5, Sections 5.3.6 and 5.3.8).

Chapter 2

Literature Review

2.1 Grape Cracking as an Agricultural and Physiological Problem

2.1.1 Definition and visual manifestation of fruit cracking

Fruit cracking in table grapes (*Vitis vinifera* L.) is defined as a physiological disorder in which the berry skin ruptures, compromising fruit quality and marketability (Guirao et al., 2025). The visible manifestation typically appears as surface splits or fissures on the berry, reflecting the mechanical failure of the cuticle–skin system under stress (La Spada et al., 2024). Recent physiological evidence further links cracking susceptibility to cultivar-dependent differences in water uptake and internal tissue expansion during critical developmental phases (Yu et al., 2025).

2.1.2 Phenological timing (veraison, late ripening stages)

The phenological development of grape berries is characterized by well-defined stages that culminate in ripening, with veraison representing a critical transition point from berry growth to maturation. Veraison marks the onset of ripening and is associated with coordinated physiological changes, including berry softening, shifts in water and solute transport, and the initiation of biochemical processes that define fruit quality (Guirao et al., 2025). The timing and duration of veraison and subsequent late ripening stages are strongly influenced by thermal accumulation and environmental conditions, leading to variability in ripening dynamics across seasons and cultivars. Recent phenological studies have demonstrated that growing degree days (GDD) provide a robust framework for describing the progression from veraison to harvest, with differences in heat accumulation directly affecting the length of late ripening stages and final harvest timing (Monteiro et al., 2025).

2.1.3 Environmental and agronomic triggers

Environmental and agronomic factors play a central role in modulating grape berry development and triggering physiological disorders during ripening, particularly under conditions of altered water availability and tissue hydration. Variations in water uptake driven by aquaporin activity have been shown to directly influence internal berry pressure and cracking susceptibility (Yu et al., 2025), while changes in cuticle structure and integrity during ripening modulate the berry's mechanical resistance to environmental stress (La Spada et al., 2024). In parallel, agronomic practices affecting calcium transport and availability after veraison further influence fruit firmness and skin stability, thereby impacting the berry's response to environmental stressors during late ripening stages (Guirao et al., 2025).

2.2 Economic Impact and Practical Consequences

2.2.1 Yield losses and reduction in marketable produce

Fruit cracking leads to substantial yield losses in table grape production by directly reducing the proportion of berries suitable for fresh market commercialization. Even limited cracking of the berry skin is sufficient to render fruit unmarketable, as it compromises visual quality and accelerates postharvest deterioration processes such as water loss, tissue softening, and increased susceptibility to decay (C. Zhang et al., 2025). As a result, a significant discrepancy often emerges between biological yield and effective marketable yield, particularly in commercial vineyards exposed to unfavorable conditions during ripening. Based on large-scale production and economic estimates, cracking-related losses in table grapes can reach approximately €175 million, assuming a 25% yield loss rate, an average production volume of 280 kt, and a mean market price of 2.5 €/kg (Alchanatis et al., 2022). At a broader scale, fruit cracking is recognized as a major physiological disorder that contributes to yield instability and economic loss across multiple fruit crops, including grapes, by increasing preharvest rejection rates and postharvest waste (Santos et al., 2023).

2.2.2 Quality degradation and shelf-life reduction

Reactive or purely reactive management strategies for fruit cracking have shown limited effectiveness in table grape production, where berry susceptibility is strongly governed by the interaction between environmental conditions during ripening and intrinsic skin and tissue properties. Reviews addressing fruit cracking across fleshy fruit crops emphasize that abrupt changes in water availability, humidity, and temperature frequently exceed the buffering capacity of short-term corrective interventions once berries reach vulnera-

ble developmental stages, rendering post-hoc management largely insufficient (Seo et al., 2022; Xu et al., 2025). In grapes, even minor cracking events are sufficient to compromise marketability, which further amplifies the economic consequences of delayed or reactive responses. Evidence from field-based mitigation studies in other thin-skinned fruits indicates that targeted preharvest treatments, such as salicylic acid sprays, can reduce cracking incidence but do not eliminate it, suggesting that similar reactive approaches in grapes are inherently constrained and highly dependent on timing and environmental context (Karantzi et al., 2021). Collectively, these findings highlight the limitations of reactive management strategies in table grapes and underscore the need for preventive, monitoring-driven, and proactive approaches to cracking risk mitigation.

2.2.3 Limitations of reactive management strategies

Reactive or purely reactive management strategies for berry cracking in table grapes remain inherently limited, largely because cracking is triggered by rapid shifts in water relations and microclimatic conditions during ripening, interacting with cultivar-specific skin and cuticle properties. Evidence from table-grape studies indicates that cracking susceptibility is tightly linked to berry structural integrity and water uptake dynamics, with critical windows during ripening in which short-term corrective actions may be insufficient to prevent splitting once mechanical resistance declines (Chang & Keller, 2021; Chang et al., 2019; Yu et al., 2025). Accordingly, while preharvest interventions aimed at strengthening the cuticle or improving tissue integrity (e.g., calcium-based or combined treatments) can contribute to improved berry skin traits and potentially reduce susceptibility, their effectiveness is typically partial and context-dependent rather than fully preventive (La Spada et al., 2024). Taken together, these findings highlight that reactive management alone is unlikely to provide robust control of cracking in commercial table-grape systems and motivate preventive, monitoring-driven, and proactive strategies that enable earlier risk identification and timely intervention (Alchanatis et al., 2022).

2.3 Physiological and Biomechanical Mechanisms of Grape Cracking

Reactive or purely reactive management strategies for fruit cracking have consistently demonstrated limited efficacy across diverse horticultural crops. Comprehensive reviews indicate that cracking is driven by complex interactions between environmental triggers—such as rainfall, humidity fluctuations, and abrupt temperature changes—and intrinsic physiological and structural fruit properties, which often overwhelm short-term or corrective interventions applied after stress exposure (Seo et al., 2022; Xu et al., 2025). As emphasized in these studies, no single management practice is capable of fully

preventing cracking once susceptible developmental stages are reached, underscoring the inherent limitations of post-hoc approaches and the need for preventive, integrated strategies. Field-based intervention trials further support this conclusion: although targeted preharvest treatments such as foliar salicylic acid applications can significantly reduce cracking incidence and improve marketable yield, their effectiveness remains partial and crop- and condition-dependent, highlighting fundamental constraints of reactive measures when applied in isolation (Karantzi et al., 2021).

2.3.1 Berry water relations and turgor pressure dynamics

Beyond softening, water uptake plays a central role. Even minor fluctuations in soil moisture or surface wetness can cause rapid increases in berry volume. When mesocarp expansion outpaces the extensibility of the skin, tensile stress accumulates in the cuticle and epidermal cell walls. As reviewed by Khadivi-Khub Khadivi-Khub, 2014, this imbalance—driven by osmotic gradients, turgor dynamics, and altered permeability—forms a generalized mechanism for cracking across thin-skinned fruit species. However, grapes are particularly sensitive because cuticular deposition slows near maturity, while mesocarp growth continues. This mismatch in developmental timing reduces the elastic reserve of the skin and predisposes berries to micro-fissuring and eventual rupture.

2.3.2 Cuticle structure, micro-cracks, and mechanical failure

The grape berry cuticle functions as both a diffusion barrier and mechanical shell. Its composition—cutin, polysaccharides, and epicuticular waxes—determines the skin's tensile strength, elasticity, and hydration behavior. Studies in sweet cherry and tomato have demonstrated that microcracks in the cuticle dramatically increase water permeability and serve as initiation sites for macroscopic cracking Emmons and Scott, 1998; Peschel and Knoche, 2005. Recent work now shows that grapes exhibit similar patterns. Chang and Keller Chang and Keller, 2021 revealed that the grape cuticle and epidermal cell walls play both overlapping and distinct roles in resisting cracking. Their microscopy studies indicate that microcracks can form days before visible splitting and propagate through weakened regions of the cuticle under mechanical stress or hydration events.

Environmental conditions exacerbate these mechanical vulnerabilities. High humidity, rain, or dew hydration increases cuticular permeability and reduces its fracture toughness. Conversely, heat and drought can cause structural fatigue through repeated cycles of dehydration and rehydration. Because these microcracks do not manifest visually, early detection requires sensitive optical or spectral tools—highlighting the relevance of hyperspectral imaging (HSI) approaches.

2.3.3 Hormonal influences and agronomic interventions

Plant growth regulators, particularly gibberellins, are widely applied in table grape production to increase berry size, reduce compactness, and improve market quality. However, these treatments also modify skin biomechanics. Lichter et al. Lichter et al., 2014 investigated the effects of GA_3 on the seeded table grape 'Zainy' and found that while berry enlargement was achieved, the treatment altered skin structure and significantly affected cracking susceptibility. Their findings highlight the trade-off between agronomic optimization and physiological stability, emphasizing the need for cultivar-specific GA_3 protocols.

Other hormones—most notably abscisic acid (ABA)—also shape berry softening and water transport. Castellarin et al. Castellarin and other, 2016 characterized the interplay between ABA metabolism, turgor loss, and cell wall modification during ripening. These hormonal signals regulate both mesocarp softness and cuticle extensibility, indirectly influencing cracking risk. Together, these works suggest that cracking is not only mechanically driven but is also hormonally modulated.

2.3.4 Cultivar-dependent susceptibility and variability

Cracking susceptibility varies widely among grape cultivars, reflecting differences in cuticle thickness, cell wall architecture, berry firmness, water relations, and patterns of sugar accumulation. Chang and Keller Chang and Keller, 2021 demonstrated cultivar-dependent variation in skin biomechanical properties, showing that small differences in cuticle thickness or epidermal morphology can translate into large differences in cracking rates. Thin-cuticle cultivars or those with rapid sugar accumulation during ripening tend to be more vulnerable.

For 'Scarlotta Seedless', the cultivar investigated in the present study, several postharvest evaluations have documented sensitivity to temperature fluctuations and hydration-induced damage A. Author et al., 2022; B. Author et al., 2024. While these works focus primarily on postharvest quality, they provide important evidence that the skin of Scarlotta berries is structurally fragile compared to other table grape varieties. Given the cultivar's widespread commercial use, understanding and detecting early signs of cuticular stress is a significant applied challenge.

2.3.5 Skin pathology as an indicator of structural instability

Although not a cracking disorder per se, grape sour rot provides insight into skin structural failure. Hall et al. Hall et al., 2018 demonstrated that sour rot development is strongly associated with breaches in berry skin integrity, allowing entry of yeasts, acetic acid bacteria, and insects. These findings reinforce the broader concept that once the

cuticle–epidermis barrier is compromised—whether by microcracks, overripening, or mechanical abrasion—the fruit becomes highly vulnerable to physiological and pathological deterioration. Thus, the onset of cracking represents a pivotal point of failure in grape berry biology.

2.3.6 Summary

Overall, grape cracking emerges from the interaction of mechanical constraints, hormonal regulation, developmental processes, and cultivar-specific structural traits. Although these mechanisms have been extensively investigated, most studies focus on visible or post-symptomatic cracking stages. Consequently, early pre-symptomatic structural and physiological changes in the berry skin remain poorly characterized, highlighting the need for non-destructive optical approaches such as hyperspectral imaging.

2.4 Precision Agriculture and Non-Destructive Sensing

2.4.1 Principles of precision agriculture and data-driven crop management

Precision agriculture (PA) has emerged as a data-driven management paradigm that seeks to optimize agricultural operations through the integration of sensing technologies, data analytics, and site-specific interventions. At its core, PA relies on systematic acquisition and analysis of large heterogeneous datasets to improve efficiency, productivity, and long-term sustainability in crop production Mgendi, 2024. Recent advances in the Internet of Things (IoT), Big Data infrastructures, and artificial intelligence (AI) have further accelerated the adoption of data-centric farming practices, enabling continuous environmental monitoring and facilitating sustainable resource management at multiple spatial and temporal scales Ahmed and Shakoor, 2025.

2.4.2 Role of proximal and remote sensing technologies

The proliferation of smart sensor technologies—including proximal sensing devices, wireless sensor networks, and real-time monitoring platforms—has substantially expanded the types of agronomic variables that can be measured in situ. Such sensors now capture environmental, physiological, and operational parameters with unprecedented resolution, which supports precise and resource-efficient crop management Soussi et al., 2024.

2.4.3 Limitations of conventional physiological measurements

Managing these heterogeneous datasets—which often vary in granularity, modality, and update frequency—requires robust data engineering pipelines capable of processing information across various temporal and spatial dimensions. This complexity is further amplified by the need to deliver decision-ready outputs in formats that support real-time or near-real-time analysis Krisnawijaya et al., 2022. To address these challenges, modern PA increasingly incorporates advanced computational methods, including big data platforms, data-driven modeling, and AI-driven analytics. These tools play a key role in transforming raw sensor data into actionable insights, allowing early detection of anomalies, improved planning, and automated decision-support workflows Ahmed and Shakoor, 2025; Mgendi, 2024.

2.4.4 Computer Vision and AI in Agriculture

Computer vision (CV) and AI have become central tools in precision agriculture, enabling automated monitoring and decision support across tasks such as plant health assessment, weed mapping, defect detection, and yield estimation Cao et al., 2025; Dhanya et al., 2022; Patrício and Rieder, 2018; H. Tian et al., 2020. In recent years, deep-learning architectures (e.g., CNNs and related variants) have dominated these applications due to their capacity to learn rich visual representations under diverse conditions Attri et al., 2023; Benos et al., 2021; Ghazal et al., 2024.

However, the agricultural domain poses persistent data constraints that are particularly acute for pixel-level tasks (e.g., segmentation). Reviews consistently note that model performance and generalization hinge on dataset representativeness and annotation quality, both of which are difficult to guarantee under field variability (illumination changes, occlusions, phenological shifts, and heterogeneous backgrounds) Benos et al., 2021; Dhanya et al., 2022; Patrício and Rieder, 2018; H. Tian et al., 2020. These limitations motivate complementary sensing modalities and learning paradigms that reduce dependence on dense manual labeling, and they contextualize why hyperspectral workflows often prioritize robust preprocessing, classical machine learning, and aggregation strategies when targeting early and field-relevant inference.

2.5 Hyperspectral Imaging for Agricultural Applications

2.5.1 Fundamentals of Reflectance and Spectral Signatures

A central concept in spectral analysis is reflectance, defined as the ratio between the radiation reflected by a surface and the radiation received by that surface. This ratio is influenced by the material's chemical properties, surface micro-topography, and the angle of the light source Blackburn, 2007. Reflectance is the primary value captured at each pixel for every wavelength in a hyperspectral image, providing a normalized measure that is independent of the illumination intensity.
Figure 2.1 formalizes this normalization, highlighting why reflectance (rather than raw radiance) is the appropriate unit for comparing spectra across field acquisitions with changing illumination.

$$Reflectance = \phi out \,/\, \phi in$$
$$\text{where } \phi = \text{radiation}$$

Figure 2.1: The formula for reflectance Blackburn, 2007.

When a material is exposed to a light source, it reflects specific portions of electromagnetic energy according to its molecular vibrations and chemical composition. This unique reaction is known as the spectral signature of a material Shaw and Manolakis, 2002. Because these signatures are specific to chemical structures, hyperspectral imaging enables reliable discrimination between visually similar targets that would otherwise appear identical under conventional RGB or multispectral sensors.
Figure 2.2 provides a concrete example of this principle: moisture changes produce systematic, wavelength-dependent signature shifts, illustrating why HSI can detect physiological and structural changes before they are visually apparent.

2.5.2 Spectral Imaging Modalities and the Electromagnetic Spectrum

Imaging systems differ substantially in the density and breadth of the spectral information they capture. Traditional RGB cameras record reflected light using only three broad bands of visible radiation: blue, green, and red Benelli et al., 2020. Multispectral imaging (MSI) typically expands this capability by capturing between 3 to 15 distinct bands and has a spectral resolution greater than 10 nm. In contrast, hyperspectral imaging (HSI) acquires reflectance data across hundreds of narrow, contiguous spectral bands, typically with a spectral resolution of less than 5 nm Mehta, 2018.

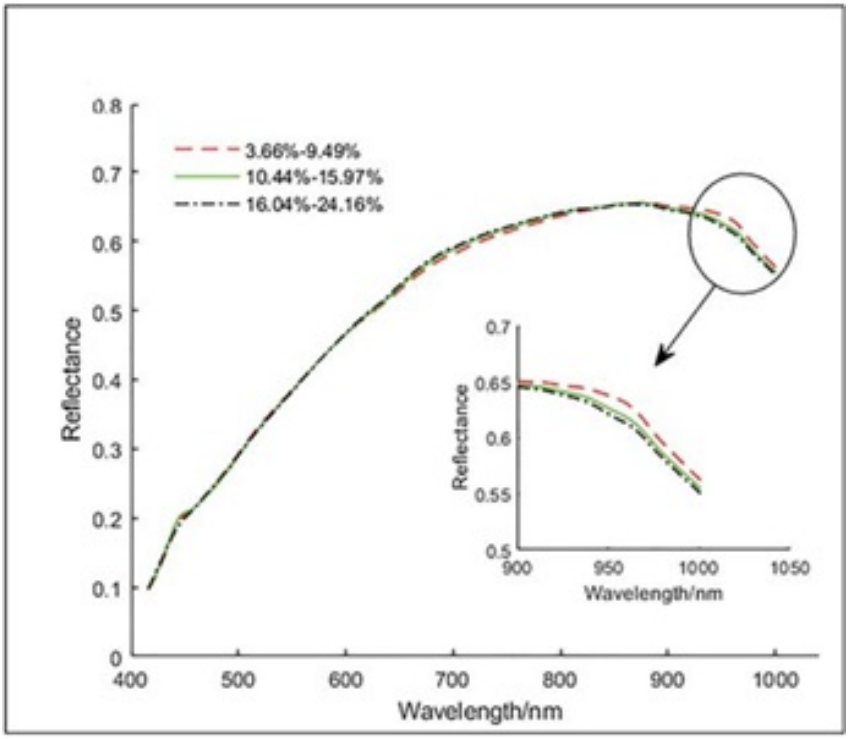

Figure 2.2: Hyperspectral signature of barley grains with varying moisture content T. Sun et al., 2020.

These systems capture broad segments of the electromagnetic spectrum, ranging from the ultraviolet (UV) around 200 nm, through the visible (VIS) light range (380 nm to 800 nm), and extending into the near-infrared (NIR) up to 1700 nm Ball, 2007. Additionally, the range often includes the short-wave infrared (SWIR) from 970 nm to 2500 nm Ball, 2007; Zwinkels, 2015. This high spectral resolution results in a three-dimensional hyperspectral data cube where each spatial pixel is associated with a detailed spectral vector, enabling the detection of both surface and subsurface characteristics that are not visible through conventional imaging Hong et al., 2025.
Figure 2.3 situates the VIS–NIR range used in this thesis within the broader electromagnetic spectrum, underscoring that the selected bands capture both pigment-driven VIS variability and structure/water-driven NIR variability.

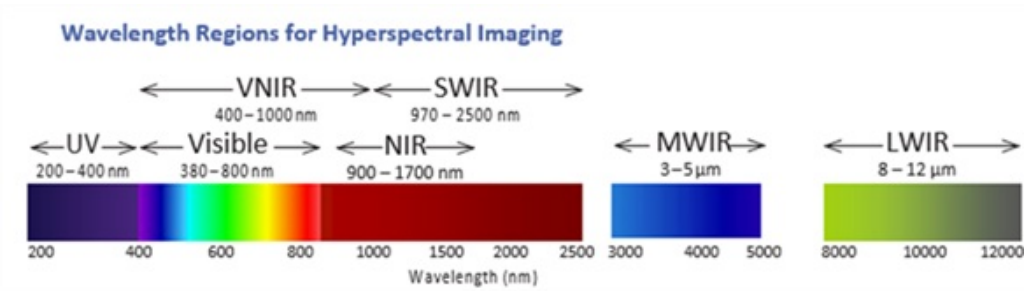

Figure 2.3: Segments of the electromagnetic spectrum commonly used in hyperspectral imaging (Middleton Spectral Vision, n.d.).

2.5.3 Advantages of Hyperspectral Imaging over RGB Imaging

Hyperspectral imaging offers substantial advantages over conventional RGB imaging by capturing detailed spectral information across a wide range of wavelengths. While RGB imaging provides only coarse color-based information, HSI records a dense spectral signature for each pixel, enabling precise characterization of material composition and condition Imaging, 2024. This enhanced spectral resolution allows HSI to detect subtle biochemical, structural, and physicochemical variations that are often indistinguishable in RGB images L. Chen et al., 2025; Liang et al., 2025.

In agricultural and food-related applications, HSI has demonstrated clear superiority over RGB imaging in tasks such as disease detection, quality assessment, and safety monitoring, owing to its ability to integrate spatial and spectral information in a non-destructive manner L. Chen et al., 2025; Liang et al., 2025. This capability facilitates the identification of pre-visual physiological stress, such as moisture imbalances or cell wall degradation, which often occur before physical symptoms like grape cracking become visible to the naked eye Abade et al., 2025; Valme et al., 2025.

2.5.4 VIS–NIR Sensitivity to Physiological and Structural Changes

The visible and near-infrared (VIS–NIR) spectral range exhibits high sensitivity to physiological and structural changes in plant tissues. Variations in VIS reflectance (400–700 nm) are primarily associated with biochemical components such as photosynthetic pigments (e.g., chlorophyll), whereas NIR reflectance (700–1000 nm) is strongly influenced by internal tissue structure and water-related properties T. Wang and Zhao, 2024; Y. Zhang et al., 2022.

Recent studies have demonstrated that VIS–NIR hyperspectral imaging enables the early detection of plant physiological stress prior to the appearance of visible symptoms, highlighting its sensitivity to subtle functional changes at the tissue level Abade et al., 2025; Liu et al., 2023. In fruit systems, VIS–NIR reflectance has been shown to correlate with internal quality attributes, including structural integrity, sugar content, and water status Q. Sun et al., 2024. These findings establish VIS–NIR HSI as a powerful tool for capturing microstructural and physiological variations that are not discernible using conventional imaging approaches.

2.5.5 Applications in Fruit Quality Assessment and Defect Detection

Hyperspectral imaging has been widely investigated as a non-destructive technique for fruit quality assessment and defect detection. Recent studies emphasize that combining

HSI with advanced machine learning and deep learning methods enables accurate evaluation of fruit quality attributes and improves food safety monitoring Yang et al., 2025; X. Zhang, Li, et al., 2024. The rich spectral signatures captured by HSI facilitate the identification of internal composition and surface characteristics that are not discernible using conventional imaging.

Experimental studies demonstrate the effectiveness of HSI for detecting both external and internal fruit defects, such as bruises, scars, and disease-related decay Akter et al., 2025; Min et al., 2023. In addition, HSI combined with feature selection techniques has shown strong potential for estimating key quality indicators such as soluble solid content (SSC), firmness, and aroma-related attributes in a variety of fruits Kanwal et al., 2025; P. Tian et al., 2023; Zhu et al., 2025. Overall, these studies establish HSI as a robust framework for postharvest management and industrial sorting, providing significant potential for industrial food safety assurance.

2.6 Machine Learning for Hyperspectral Data Analysis

Traditional machine learning approaches for hyperspectral imaging

Traditional machine learning (ML) approaches have been widely adopted for hyperspectral imaging (HSI) analysis in agricultural and food-quality applications, primarily due to their effectiveness in small- to medium-sized datasets and their reliance on well-established spectral preprocessing pipelines. Comprehensive review studies indicate that classical ML methods continue to play a central role in precision agriculture, supporting a broad range of tasks including crop and disease detection, stress monitoring, yield assessment, and produce quality evaluation García-Vera et al., 2024; Ram et al., 2024.

In typical traditional HSI workflows, each sample is represented as a spectral vector extracted at the pixel level, from a defined region of interest, or through spatial or spectral aggregation. Supervised learning is then applied using conventional algorithms such as partial least squares regression or discrimination (PLS/PLSR), support vector machines and regression (SVM/SVR), and other statistical or kernel-based models. These models are commonly combined with dedicated spectral preprocessing techniques aimed at mitigating sensor noise and compensating for scattering and illumination variability. Widely used preprocessing methods include Savitzky–Golay smoothing, standard normal variate (SNV) normalization, multiplicative scatter correction (MSC), and derivative-based spectral transformations.

Numerous studies have demonstrated the effectiveness of such classical pipelines for non-destructive assessment of fruit quality attributes. For instance, hyperspectral data com-

bined with PLSR and SVR models have been successfully used to estimate physicochemical properties of apples during storage following Savitzky–Golay filtering and SNV normalization Khaled et al., 2023. Similarly, PLS-based models employing tailored preprocessing strategies have achieved high accuracy for parameters such as soluble solids content, acidity, and phenolic compounds in apples, underscoring the strong dependence of classical ML performance on appropriate spectral normalization Hasanzadeh et al., 2022.

A major advantage of traditional ML approaches lies in their interpretability and their ability to identify informative wavelengths within the high-dimensional hyperspectral space. Consequently, feature extraction and wavelength selection techniques are frequently integrated into classical pipelines to reduce redundancy and computational complexity while preserving performance. Competitive adaptive reweighted sampling (CARS), for example, has been employed to extract effective wavelength subsets and to construct reduced-band models suitable for fast and potentially real-time applications Khaled et al., 2023. Comparable results have been reported in pear quality assessment studies, where wavelength selection combined with LS-SVM and optimized preprocessing substantially improved model robustness and estimation accuracy Z. Zhang et al., 2024. These findings are consistent with broader reviews emphasizing the central role of preprocessing and feature selection in traditional HSI-based learning frameworks Ram et al., 2024.

Despite their proven effectiveness, traditional ML approaches are often evaluated under relatively controlled experimental conditions, such as laboratory or postharvest environments with standardized acquisition protocols. As a result, many existing studies focus on detection or quality estimation tasks based on already manifested spectral differences rather than on truly pre-symptomatic inference. Review studies further highlight persistent challenges in transferring HSI models from laboratory settings to real-world field deployment, including illumination variability, background complexity, sensor limitations, and domain shift effects García-Vera et al., 2024; Ram et al., 2024. Recent preharvest investigations demonstrate that strong performance can be achieved through careful band reduction and model design; however, they also reveal that robustness and generalization remain key obstacles for operational field applications Fass et al., 2025. Overall, prior work establishes traditional ML as a powerful and interpretable foundation for hyperspectral data analysis, while motivating methodological choices that explicitly address variability and scalability when targeting early and field-relevant inference tasks.

2.6.1 Deep learning and non-linear models

Deep learning has also been widely explored for hyperspectral learning, including spectral-only networks that operate on one-dimensional signatures and spectral–spatial architectures that learn jointly from local patches or full cubes. Such models can exploit non-

linear structure and spatial context without requiring hand-crafted features, and they have shown strong performance in benchmark hyperspectral classification settings Z. Chen et al., 2024.

In practice, however, hyperspectral deep learning in agriculture faces the same fundamental constraints highlighted for CV more broadly (Section 2.4.4): limited labeled data, expensive annotations (especially for pixel-level segmentation), and acquisition-dependent domain shift. These issues are amplified by the high dimensionality and inter-band correlation of hyperspectral data, which can increase overfitting risk and reduce transferability across scenes and seasons. Consequently, recent reviews emphasize that classical pipelines—combining explicit spectral preprocessing, interpretable models, and wavelength selection—remain competitive and operationally attractive for small- to medium-scale agricultural datasets Attri et al., 2023; García-Vera et al., 2024; Ram et al., 2024.

2.6.2 Pixel-level versus image-level modeling paradigms

In hyperspectral image analysis, the choice of representation unit plays a central role in determining both the sensitivity of models to localized changes and their robustness under real-world conditions. Hyperspectral data are inherently acquired at the pixel level, where each pixel is represented as a high-dimensional spectral vector spanning contiguous wavelength channels. Pixel-level modeling directly exploits this representation and enables fine-grained discrimination of material properties and subtle biochemical variations, which can be critical for detecting early stress signals or micro-scale defects Moeini and Wang, 2018.

Despite these advantages, pixel-level approaches face substantial practical limitations. Pixel-wise classification or inference typically requires dense and accurate pixel-level annotations, which are costly and time-consuming to obtain in agricultural contexts. Moreover, pixel-based outputs are often sensitive to noise, mixed pixels, and background variability, particularly under non-uniform illumination and complex field conditions. To address these challenges, many modern hyperspectral methods incorporate spectral–spatial strategies that aggregate information across local neighborhoods using patch-based, region-based, or superpixel representations. By integrating spatial context with spectral information, such approaches reduce sensitivity to pixel-level inconsistencies and often achieve improved robustness and generalization Z. Chen et al., 2024; Moeini and Wang, 2018.

By contrast, image-level modeling treats the entire hyperspectral cube or large spatial regions as holistic inputs to machine learning models, thereby simplifying annotation requirements and enabling global context to inform decisions. While image-level approaches

may be less sensitive to highly localized early anomalies, they benefit from reduced labeling effort and increased stability under variable acquisition conditions. Recent empirical evaluations further highlight that the incorporation of spatial context is a key factor in achieving reliable and generalizable performance in deep learning-based hyperspectral classification Z. Chen et al., 2024. Overall, the trade-offs between pixel-level, spectral–spatial, and image-level modeling paradigms reflect fundamental balances between spatial granularity, label efficiency, and operational robustness in hyperspectral applications.

2.6.3 Challenges: class imbalance, background clutter, and generalization

Field-deployable hyperspectral learning systems must cope with several interacting sources of error. First, class distributions are often highly imbalanced (e.g., early defects occupy a small fraction of pixels), which can bias learners and destabilize threshold-based decision rules. Second, background clutter and mixed pixels are common in vineyard imagery, where leaves, wood, soil, and artificial materials may introduce confounding spectra and spatial edge effects. Third, acquisition variability (illumination, viewing geometry, and sensor-specific noise characteristics) produces domain shift that degrades model transfer from controlled conditions to operational settings García-Vera et al., 2024; Ram et al., 2024. These challenges are particularly severe for pixel-level segmentation, where dense labeling is costly and small spatial errors can propagate into unreliable image-level decisions.

While the modeling strategies reviewed above span a wide range of algorithms and data representations, their application in fruit analysis literature can be broadly divided into two conceptual objectives: (i) the detection of existing, observable defects or quality attributes, and (ii) the early identification of latent physiological disorders prior to visible manifestation. The following section reviews prior work in both domains, with particular emphasis on hyperspectral approaches for fruit defect detection and early-stage, pre-symptomatic detection.

2.7 Related Work on Fruit Defect Detection and Early-Stage Detection

Previous studies applying hyperspectral imaging to fruit quality analysis have addressed both defect detection and early-stage, pre-symptomatic detection, although these objectives are often treated implicitly rather than explicitly. In the context of this review, detection refers to the identification of defects that are already visually or structurally manifested, whereas early-stage detection denotes the identification of pre-symptomatic

or latent conditions that precede visible damage.

2.7.1 HSI-based detection of visible fruit defects

Hyperspectral imaging (HSI) is a well-established non-destructive technique for detecting visible fruit defects, including skin blemishes, decay, and mechanical injuries, particularly in postharvest inspection and grading applications. By combining high spectral resolution with spatial information, HSI enables effective discrimination between healthy and defective tissues based on characteristic reflectance differences associated with structural damage, biochemical changes, or pathogen activity.

Numerous studies demonstrate the effectiveness of classical hyperspectral analysis pipelines for visible defect detection. Wang et al. B. Wang et al., 2023 employed hyperspectral imaging together with spectral preprocessing and wavelength selection methods (CARS and SPA) to classify natural skin defects in *Cerasus humilis* fruit. Their approach achieved high classification accuracy and enabled spatial localization of defective regions, highlighting the importance of integrating spectral discrimination with image-level analysis. These findings are consistent with broader reviews showing that Vis/NIR spectroscopy and hyperspectral techniques are robust tools for identifying surface degradation across diverse fruit types under controlled conditions C. Wang et al., 2025.

Beyond surface-level defects, hyperspectral imaging has also been applied to the detection of decay processes during postharvest storage. Min et al. Min et al., 2023 reviewed recent advances in early decay detection using hyperspectral imaging, demonstrating that HSI can capture spectral changes associated with fungal infection before severe tissue degradation becomes visually apparent. Nevertheless, most reported applications focus on monitoring ongoing decay during storage rather than on identifying latent physiological disorders prior to visible symptom development.

Comprehensive reviews further confirm the maturity of hyperspectral imaging as a quality assessment tool within the fruit and vegetable supply chain. Vignati et al. Vignati et al., 2023 summarized key concepts, data processing strategies, and applications of HSI for quality monitoring, emphasizing its effectiveness for defect detection and postharvest inspection, while also noting limitations related to environmental variability and model transferability.

Overall, existing literature establishes hyperspectral imaging as a reliable and powerful technology for detecting visible fruit defects and postharvest decay under controlled acquisition conditions. However, the majority of these studies address defects that are already externally or structurally expressed, thereby motivating further research toward pre-symptomatic detection frameworks capable of identifying latent physiological changes prior to visible manifestation, particularly under realistic field conditions.

2.7.2 Attempts Toward Early and Pre-Symptomatic Defect Detection

Several investigations have demonstrated that HSI can reveal latent internal disorders before external manifestation. Dong et al. Dong et al., 2025 showed that early-stage bitter pit in apples can be identified using VIS–NIR hyperspectral data combined with spectral and texture features, achieving high classification accuracy prior to visible pit formation. This highlights the capacity of HSI to detect internal physiological imbalances before macroscopic damage occurs.

Pre-symptomatic detection of pathogen infection has also been reported across multiple crops. Haghbin et al. Haghbin et al., 2023 demonstrated that gray mold infection in kiwifruit can be identified using hyperspectral data and chemometric models, capturing infection-related spectral changes before visible decay appears. Similarly, hyperspectral imaging enabled early detection of anthracnose in pear leaves through multi-source feature fusion Y. Zhang et al., 2024, as well as the identification of bacterial leaf spot in tomato prior to symptom development X. Zhang, Vinatzer, and Li, 2024.

Recent advancements have further integrated HSI with deep learning to enhance sensitivity to subtle stress-related patterns. Ou et al. Ou et al., 2024 combined HSI with deep neural networks for the early detection of gray mold in strawberry leaves, identifying spectral signatures associated with initial pathogen stress.

Despite these results, most early-detection studies remain limited to controlled environments and localized leaf- or fruit-level analysis. Truly field-ready frameworks that provide early-warning signals ahead of defect emergence under realistic, field-scale vineyard conditions remain scarce. This underscores the need for methodologies that combine field-acquired hyperspectral data with robust preprocessing, wavelength reduction, and image-level aggregation to deliver practical, pre-symptomatic early-warning screening in real-world agricultural settings.

2.7.3 Limitations of Existing Approaches under Field Conditions

Despite the substantial progress demonstrated by hyperspectral imaging (HSI) in fruit quality assessment and early defect detection, the majority of existing approaches remain challenged by limited applicability under real-world field conditions. Most studies are conducted in controlled laboratory or postharvest environments, where illumination, background, viewing geometry, and acquisition timing are carefully regulated. While such settings facilitate methodological development and performance benchmarking, they do not adequately reflect the complexity and variability encountered in operational orchard or vineyard scenarios.

Several reviews emphasize that environmental variability represents a major obstacle for field deployment of HSI systems. Vignati et al. Vignati et al., 2023 note that changes in ambient lighting, surface moisture, temperature, and background composition can significantly distort spectral signatures, reducing model robustness and transferability. Similarly, Wang et al. C. Wang et al., 2025 highlight that Vis/NIR-based fruit quality models often exhibit degraded performance when transferred across seasons, cultivars, or acquisition setups, necessitating frequent recalibration.

Another key limitation lies in data annotation and scalability. Many HSI-based studies rely on dense pixel-level or region-level labeling, which is labor-intensive, subjective, and difficult to obtain consistently under field conditions. This constraint is particularly pronounced in early-detection studies, where pre-symptomatic changes are subtle and often lack clear visual reference points for annotation. As a result, most early-detection experiments remain restricted to localized fruit- or leaf-level samples acquired under controlled conditions Haghbin et al., 2023; Y. Zhang et al., 2024.

Variability across acquisition conditions further complicates field deployment. Even when hyperspectral signatures are informative under controlled settings Min et al., 2023, pre-harvest field operation introduces additional sources of uncertainty related to illumination, background composition, plant phenology, weather dynamics, and management practices, all of which can distort spectra and induce domain shift.

Finally, while recent studies have explored the integration of deep learning with HSI to enhance sensitivity to subtle stress patterns, these approaches remain data-intensive and highly task-specific. Deep learning models typically require large, consistently labeled datasets that are rarely available in agricultural field contexts, limiting their generalizability and operational feasibility Ou et al., 2024. Consequently, most existing frameworks prioritize detection of already manifested defects or localized early symptoms, rather than robust, pre-symptomatic early-warning screening at field scale.

Collectively, these limitations indicate that although HSI is a powerful sensing modality, current methodologies fall short of enabling reliable early warning of fruit disorders under realistic field conditions. Addressing environmental variability, annotation constraints, and model transferability remains essential for advancing HSI-based systems from experimental studies toward practical, field-deployable early warning tools.

Taken together, the literature provides strong evidence that hyperspectral signatures can reveal latent physiological change, but field-scale early-warning frameworks for latent disorders remain scarce under realistic acquisition variability García-Vera et al., 2024; Ram et al., 2024; Vignati et al., 2023; C. Wang et al., 2025. This gap motivates field-ready single-acquisition screening pipelines that (i) reduce spectral redundancy through wavelength selection and (ii) aggregate pixel-level decisions into conservative scene- or

cluster-level outputs that are more robust to background clutter and illumination variability.

2.8 Research Gap and Study Positioning

2.8.1 Summary of Established Knowledge

Hyperspectral imaging (HSI) has been extensively investigated as a non-destructive tool for agricultural monitoring, particularly for the detection of visible defects, postharvest decay, and quality-related attributes in fruits and vegetables. Numerous studies have demonstrated that spectral and spectral–spatial features can effectively discriminate between healthy and defective tissues, quantify physicochemical properties, and support automated grading and sorting processes.

In parallel, the physiological and biomechanical mechanisms underlying fruit cracking have been widely studied using destructive measurements, biochemical assays, and controlled experiments. These studies have established the roles of cuticle integrity, cell wall composition, water relations, and hormonal regulation in crack development, providing valuable biological insight into cracking susceptibility.

Despite this extensive body of work, the integration of hyperspectral imaging with physiological knowledge of cracking remains limited. In particular, while HSI has proven effective for detecting existing defects, its use for providing early-warning insight into a physiological disorder such as grape berry cracking—based on early spectral trends under realistic field acquisition variability—remains largely unexplored.

2.8.2 Identified Methodological and Application Gaps

A central gap in the existing literature lies in the focus on reactive rather than proactive screening frameworks. Most hyperspectral studies in fruit analysis are designed to identify defects or diseases after they have already manifested visually or structurally. Even studies described as "early detection" typically operate at a stage where symptoms are already incipient or localized, rather than truly pre-symptomatic.

Methodologically, many existing approaches rely on high-dimensional spectral data without explicitly addressing spectral redundancy or computational efficiency. While feature selection and wavelength reduction techniques have been applied in quality assessment tasks, they are rarely integrated into end-to-end field workflows to support early warning. Moreover, most models are trained and evaluated under controlled laboratory or postharvest conditions, limiting their robustness and transferability to preharvest field environments characterized by variable illumination, background complexity, and plant heterogeneity.

From an application perspective, there is a notable lack of non-destructive tools capable of providing actionable early warnings for physiological disorders in fruit crops. In the context of table grapes, cracking is typically identified only after visible damage occurs, at which point economic loss is often unavoidable. Existing scouting and inspection strategies therefore do not support timely intervention or informed decision-making at the vineyard level.

2.8.3 Lack of Early, Non-Destructive Crack Early-Warning Frameworks

Although grape cracking has been extensively studied from a physiological and mechanistic standpoint, few studies have attempted to detect cracking at an early stage using optical sensing techniques. In particular, the detection of pre-symptomatic microcracks or latent physiological stress—prior to visible skin rupture—remains largely unaddressed in the literature.

This gap reflects both technical and conceptual challenges. Pre-symptomatic cracking is characterized by subtle structural and biochemical changes that do not produce obvious visual cues, making traditional imaging approaches insufficient. Furthermore, the lack of dense, consistently labeled hyperspectral datasets acquired under field conditions has limited the development of models capable of learning early spectral signatures associated with cracking susceptibility.

As a result, no established framework currently exists that combines non-destructive hyperspectral imaging, machine learning, and field-ready image-level aggregation to deliver field-ready early warnings for grape cracking before it becomes visually apparent.

2.8.4 Positioning of the Present Study within the Literature

The present study is positioned at the intersection of physiological research on grape cracking and applied hyperspectral data analysis. By leveraging VIS–NIR hyperspectral imaging, machine learning, and spectral feature selection, this work aims to move beyond defect detection toward field-relevant early-warning screening of cracking susceptibility.

Specifically, the proposed approach integrates efficient wavelength selection with pixel-level classification and spatial aggregation to capture subtle changes in berry skin integrity and physiological state prior to visible cracking. Unlike prior studies that focus on postharvest or controlled acquisition, this work emphasizes early-stage, preharvest screening under realistic field conditions.

In doing so, this study bridges a critical gap between fundamental understanding of cracking mechanisms and practical, non-destructive vineyard screening. The resulting

framework contributes a novel perspective to the literature by explicitly addressing the connection between pixel-level spectral classification and whole-image decision support through spatial aggregation and by demonstrating the feasibility of hyperspectral imaging as an early warning tool for grape cracking.

Chapter 3

Research Objectives and Hypotheses

3.1 Research Objectives

The primary objective of this research is to develop and validate hyperspectral imaging (HSI) methods for crack-related *detection/identification at the time of measurement* in table grapes ('Scarlotta' cultivar) under field conditions, spanning both early-stage (absent-to-minimal/incipient cracking) and late-stage (advanced, macroscopically visible cracking) acquisition conditions. The work bridges the gap between spectroscopic research on cracking mechanisms and practical, non-destructive agricultural screening by leveraging imaging, machine learning, and robust whole-image aggregation.

3.2 Research Hypotheses

The research is guided by the following hypotheses, structured hierarchically to reflect a progression from physical feasibility to algorithmic performance, robustness, early detection capability, and spectral efficiency.

Hypothesis 1: Spectral Distinguishability (Physical Basis)

This hypothesis examines whether a fundamental physical difference exists in the spectral reflectance properties of healthy and cracked grape tissues.

- H_0**:** There is no statistically significant difference in the spectral signatures of healthy and cracked tissues in 'Scarlotta' grapes.
- H_1**:** Statistically significant differences exist in the spectral signatures of healthy versus cracked grape skins at specific wavelengths, providing a physical basis for subsequent algorithmic discrimination.

Hypothesis 2: Pixel-Level Classification Feasibility

This hypothesis evaluates whether machine learning algorithms can effectively learn the spectral differences identified in Hypothesis 1 under controlled, pixel-level conditions.

- H_0**:** A machine learning model trained on hyperspectral data cannot achieve classification performance, as measured by standard metrics (e.g., F1-score, precision/recall, or MCC), significantly higher than a random or baseline classifier at the pixel level.
- H_1**:** The proposed machine learning framework can successfully classify individual pixels as *Cracked* or *Healthy* with high performance, effectively learning the underlying spectral decision boundary.

Hypothesis 3: Whole-Image Detection and Robustness

This hypothesis assesses the robustness of the trained models when applied to realistic whole-image hyperspectral scenes containing complex background elements not present in the clean pixel dataset.

- H_0**:** The model fails to distinguish between the spectral signatures of cracks and complex background clutter (e.g., leaves, woody tissue, or plastic), resulting in a high false positive rate when applied to full hyperspectral images.
- H_1**:** The spectral signatures of cracks are sufficiently distinct from background clutter to allow the model to effectively suppress noise and detect cracks within full-image scenes with high precision.

Hypothesis 4: Early Detection Capability

This hypothesis investigates the ability of the whole-image framework to detect cracking at its onset, prior to the appearance of visually observable symptoms.

- H_0**:** The spectral changes associated with the early onset of cracking are too subtle to be reliably detected, limiting the model's applicability to late-stage damage.
- H_1**:** The spectral model is sufficiently sensitive to detect early physiological changes and micro-cracks, enabling early-stage identification of clusters exhibiting crack-related spectral signatures at the time of measurement (even when macroscopic cracking is not yet clearly visible).

Hypothesis 5: Spectral Efficiency and Operational Feasibility

This hypothesis examines whether the detection capabilities demonstrated in Hypotheses 3 and 4 can be preserved when using a reduced subset of informative spectral bands.

- H_0**:** Reducing the number of spectral bands results in a significant degradation in detection performance, either in whole-image scenarios or during early-stage detection, implying that the full hyperspectral spectrum is required.
- H_1**:** A carefully selected subset of informative wavelengths captures the key physiological markers of cracking, enabling robust detection in both whole-image and early-stage scenarios using cost-effective multispectral sensing configurations.

This thesis is organized into several interconnected chapters. The *Literature Review* chapter provides a comprehensive overview of grape cracking mechanisms and relevant precision agriculture techniques. The *Materials and Methods* chapter describes the experimental design, data acquisition procedures, hyperspectral imaging systems, and modeling approaches used in this study. The *Results* chapter presents the experimental findings, including pixel-level classification, whole-image crack detection, and wavelength selection experiments. The *Discussion* chapter interprets these results in the context of early crack detection, physiological relevance, and practical deployment considerations. Finally, the *Conclusions and Future Work* chapter summarizes the main contributions of the study and outlines directions for future research.

Chapter 4

Materials and Methods

4.1 Data Acquisition

4.1.1 Study Area and Experimental Design

The study was conducted in the Lachish region of Israel, an area characterized by a semi-arid climate with a hot, dry summer and a mild winter. These conditions make the region a central hub for grape cultivation (viticulture) in Israel. The experiment was conducted in a commercial table grape vineyard (*Vitis vinifera* L., cv. 'Scarlotta'), in collaboration with the "Tali Grapes" brand. The vineyard was grafted onto 1103 Paulsen rootstock and was planted in 2018.

Figure 4.1 summarizes the block structure and irrigation assignment used throughout the study, clarifying the spatial provenance of the samples used later for row-based calibration and testing.

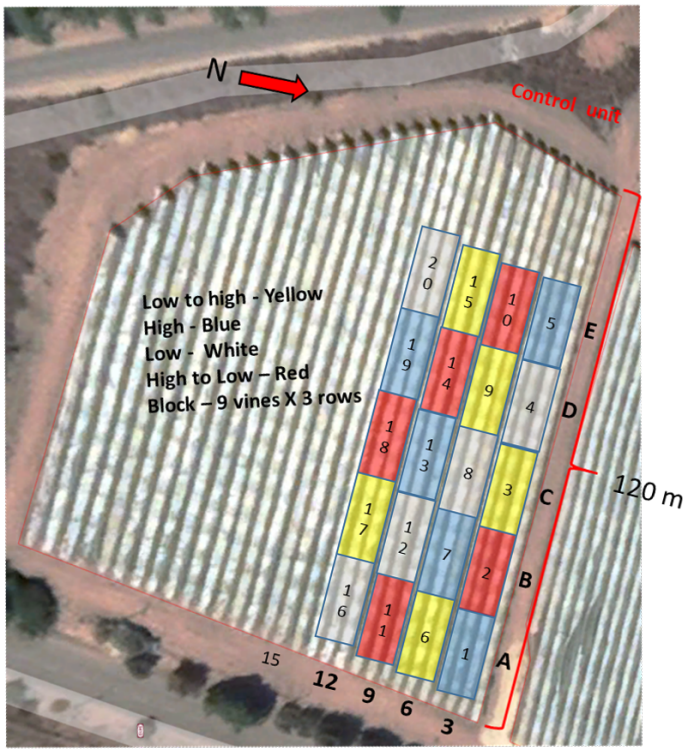

Figure 4.1: Map of the experimental vineyard showing the five randomized blocks (A–E) and the four irrigation regimes applied within each block.

The experimental design followed a Randomized Complete Block Design (RCBD), including five replicates (Blocks A–E). Within each block, four different irrigation regimes were tested, resulting in a total of 20 experimental plots (5 blocks × 4 treatments).

Each experimental plot consisted of three consecutive rows of nine vines each (27 vines per plot). To minimize edge effects and water spillover between irrigation regimes, only vines from the middle row of each plot were selected for measurement. From each middle row, 12 representative grape clusters were tagged, yielding a total sample size of 240 clusters (20 plots × 12 clusters).

The four irrigation regimes tested were:

- **High Irrigation (Blue):** 796 mm of water throughout the season.
- **Low Irrigation (White):** 376 mm of water throughout the season.
- **Reducing Irrigation (Red):** A transition from high to low irrigation (total 532 mm), beginning at the post-veraison stage.
- **Increasing Irrigation (Yellow):** A transition from low to high irrigation (total 645 mm), beginning at the post-veraison stage.

Irrigation commenced on April 29, 2024, and was applied daily or every other day via a drip irrigation system.

The experiment continued until the end of September 2024. Physiological and yield measurements—including stem water potential, stomatal conductance, fruit properties, and percentage of healthy clusters—were performed weekly. Physiological data were collected using a Scholander Pressure Bomb and a Porometer, and soil moisture was measured using Soil Moisture Sensors.

4.1.2 Imaging Systems

To study grape cracking in a comprehensive way, a multi-modal imaging setup was used. The system combined three imaging sensors placed at the same location, each capturing different types of information from a different part of the electromagnetic spectrum. Together, these sensors provided complementary spectral, spatial, and thermal data, allowing a more complete analysis of grape berry condition and cracking development. All images were collected from a fixed distance of approximately 1 m from the grape clusters to ensure consistent scale and alignment across all measurements.

Hyperspectral Imaging System (HSI)

Hyperspectral data were collected using the **Specim IQ** (Specim, Spectral Imaging Ltd., Oulu, Finland), a portable snapshot hyperspectral camera designed for field applications. The camera operates in the Visible and Near-Infrared (VNIR) spectral range (400–1000 nm) and produces 3D datacubes of size $512 \times 512 \times 204$ for each snapshot. Figure 4.2 documents the practical acquisition setup under vineyard conditions; this field configuration is important context for the later performance gap between pixel-level and whole-image inference under background clutter and illumination variability.

(a) Field deployment of the Specim IQ system in the vineyard.

(b) Hyperspectral image acquisition of grape clusters using the Specim IQ.

Figure 4.2: Hyperspectral imaging setup and data acquisition using the Specim IQ system under vineyard conditions.

- **Spectral Resolution:** The system captures 204 contiguous spectral bands with a Full Width at Half Maximum (FWHM) of 7 nm and a spectral sampling rate of approximately 3 nm. The high spectral fidelity is ensured by a signal-to-noise ratio (SNR) of $> 400:1$.

- **Spatial Resolution:** The sensor has a resolution of 512×512 pixels. With a $31° \times 31°$ Field of View (FOV), at a 1 m working distance, the camera covers a physical area of approximately 0.55 m $\times$ 0.55 m. This configuration yields a theoretical spatial resolution of approximately **1.08 mm/pixel**, sufficient for resolving individual berries and larger cracks.

- **Radiometric Calibration:** A spectrally flat, diffuse white reference panel (Spectralon®, $\approx 99\%$ reflectance) was included in every captured scene. This allowed subsequent normalization of raw radiance data into relative reflectance values, accounting for varying natural illumination conditions in the vineyard.

RGB Imaging System

To provide high-resolution visual context and capture fine surface textures that might be missed by the lower spatial resolution of the HSI system, a high-end digital camera was used.

- **Camera & Sensor: Canon EOS R5**, equipped with a 45-megapixel full-frame (36×24 mm) CMOS sensor, producing 14-bit RAW images with a resolution of 8192×4608 pixels.

- **Optics:** The camera was fitted with a **35 mm** prime lens, providing a wide Field of View of 54.4° (horizontal) $\times$ 37.8° (vertical) and sufficient depth of field to keep the entire cluster in focus.

- **Spatial Resolution:** At the 1 m working distance, this system achieved an extremely high theoretical spatial resolution of approximately **0.13 mm/pixel**. This level of detail is critical for detecting micro-cracks (hairline fissures) and minute alterations in the berry skin cuticle before they become visible to the naked eye or the HSI sensor.

Thermal Imaging System

Canopy and grape cluster temperatures, which are widely used as indirect indicators of plant water status, stomatal conductance, and transpirational cooling dynamics, were monitored using a high-definition thermal imaging system.
Figure 4.3 illustrates the thermal modality acquired alongside Theramal Camera (FLIR T1020).

(a) FLIR T1020 thermal camera used for vineyard measurements.

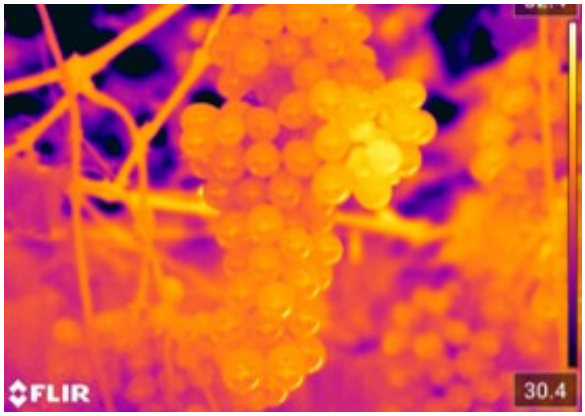

(b) Thermal image of a grape cluster showing surface temperature variations.

Figure 4.3: Thermal imaging system and example thermal data acquired from grape clusters under vineyard conditions.

- **Camera: FLIR T1020** (Teledyne FLIR LLC, Wilsonville, OR, USA), a high-performance uncooled microbolometer specifically designed for precision research.
- **Sensor & Optics:** The camera has a thermal resolution of 1024×768 pixels with a 17 μm pixel pitch, operating in the Long-Wave Infrared (LWIR) spectral range (7.5–14 μm). It was equipped with a standard **34 mm** lens (adjustable focus including autofocus), providing a FOV of 45° (H) × 34° (V).
- **Performance:** The system boasts a high thermal sensitivity (Noise Equivalent Temperature Difference, NETD) of < 20 mK (< 0.02°C) at 30°C, enabling the detection of subtle temperature gradients across the grape cluster.
- **Spatial Resolution:** At the 1 m working distance, the theoretical thermal spatial resolution was approximately **0.81 mm/pixel**, allowing for accurate temperature extraction from individual berries while minimizing mixed-pixel effects from the surrounding air or leaves.

Due to the high dimensionality of the acquired data, individual hyperspectral images were substantially larger than the corresponding RGB and thermal images. On average, a single hyperspectral datacube occupied approximately **200 MB**, compared to approximately **11 MB** for a high-resolution RGB image and **2.5 MB** for a thermal image. In total, the imaging campaign resulted in a dataset of approximately **575 GB** of raw data, highlighting the computational and storage challenges associated with multi-modal hyperspectral analysis.

4.1.3 Data Collection Protocol

Data collection was conducted during concentrated field days, typically once a week (Mondays or Thursdays), throughout the growing season from June to the end of September. To ensure consistent lighting conditions, field operations were strictly scheduled between 08:00 and 17:00.

Daily Schedule and Logistics

Each collection day began at 05:30 at the Volcani Institute with equipment organization and verification. Departure to the vineyard in Lachish occurred at approximately 06:00. Upon arrival at 07:00–08:00, the imaging systems were mounted on their respective tripods and calibrated.

Sampling Strategy

Due to significant differences in acquisition time between modalities, a split sampling strategy was employed:

- **RGB Imaging:** All 240 marked grape clusters (12 clusters $\times$ 20 plots) were imaged first during each field day to capture them under relatively uniform early-morning lighting.
- **Hyperspectral Imaging (HSI):** Due to the complex acquisition process—which required re-positioning the camera and white reference panel for each cluster, followed by a dedicated spectral focusing procedure—each HSI scan took approximately 2-3 minutes. Consequently, only a subset of 120 clusters was imaged per session. These clusters were selected to represent a balanced cross-section of the experimental blocks, ensuring full dataset coverage over alternating sessions. HSI acquisition typically commenced around 10:00 AM when sunlight was more stable and intense.
- **Thermal Imaging:** Thermal image acquisition was purposely scheduled for later in the day (starting around 12:00 PM), after RGB imaging was complete. This timing leverages the high ambient temperatures typical of midday in the semi-arid Negev region to maximize thermal contrast on the berry surface. Specifically, cracked or decaying areas, often characterized by exposed moist tissue or conversely by localized dehydration, exhibit different thermal signatures compared to healthy, intact skin due to variations in evaporative cooling rates. Capturing images during peak heat enhances these temperature differentials, improving the detectability of such defects.

Field Procedure

To ensure accurate re-imaging, a consistent labeling system was implemented. Target clusters were marked with laminated, color-coded tags attached via plastic cable ties. The tags featured a numeric identifier (1–60), which was repeated across treatments but distinguished by the specific color assigned to each irrigation regime. This design allowed for unambiguous identification and durability against humidity. Furthermore, vine locations were georeferenced using a GPS module integrated into the thermal camera.

Although only the RGB and HSI datasets were analyzed in the present study, all imaging systems were spatially co-aligned and temporally synchronized during field acquisition to facilitate potential future analyses.

Table 4.1: Pixel-level datasets.

Dataset	Labels	Purpose	Method	H.
Binary	Healthy; Cracked	Spectral differences: intact vs damaged	RGB Pixel → SAM2 → HS segment extract	H1, H2
Multi-Class (10)	Cracked Healthy Leaf Background and more...	Spectral signatures: all materials	RGB Pixel → SAM2 → HS segment extract	H3

Table 4.2: Whole-image datasets.

Dataset	Acquisition Stage	Purpose	Method	H.
Late-Stage	Advanced cracking	Detection under visible crack conditions	Binary label	H3
Early-Stage	Initial onset	Detection at early crack-development stage	Binary label	H4

Note: Early/late refer to acquisition-stage subsets at different crack-progression levels (time of measurement). HSI+RGB pairs. Pixel: segment→label→extract. Image: direct labeling.

4.1.4 Dataset Statistics

Dataset	Split / Variant	Samples	Positive (CRACK)	Negative (REGULAR)
Pixel-Level Binary	Exported labeled pixels	94,166	24,548	69,618
Pixel-Level Multi-Class	Exported labeled pixels	1,189,041	24,548	69,618
Whole-Image Early	Row 1 calibration	172	32	140
Whole-Image Early	Row 2 test	60	32	28
Whole-Image Late	Row 1 calibration	160	35	125
Whole-Image Late	Row 2 test	60	34	26

Table 4.3: Exact dataset statistics used in the experiments. For whole-image inference, Row 1 is used for calibration/tuning and Row 2 for held-out testing.

Pixel-level exports.

Dataset	Labeled Pixels	Source
Binary	94166	80 segments across 19 hyperspectral images
Multi-class	1189041	227 segments across 54 hyperspectral images

Table 4.4: Pixel-level exports: dataset composition.

Multi-class exported pixels by class.

Class	Pixels	Description
BACKGROUND	378,194	background pixels (e.g., soil and mixed background).
WHITE_REFERENCE	270,159	White reference panel pixels.
TRIPOD	137,494	Tripod and imaging setup components.
LEAF	120,552	Vine foliage.
BRANCH	78,654	Woody vine structures.
REGULAR	69,618	Intact grape tissue without visible defects.
PLASTIC	66,185	Artificial vineyard elements.
BURNT_PIXEL	36,676	Saturated or corrupted pixels.
CRACK	24,548	Grape tissue exhibiting visible cracking symptoms.
IRON	6,961	Metallic elements.

Table 4.5: Multi-class pixel-level dataset: exported pixels by class.

4.1.5 Pixel-Level Dataset Preparation

To enable efficient creation of the pixel-level dataset—required to test spectral differences between healthy and cracked grape tissues (Hypothesis 1) and to assess pixel-level classification feasibility using machine learning (Hypothesis 2)—a custom graphical user interface (GUI) was developed in Python. The tool integrates data visualization, interactive annotation, and model inference in a single platform (see Figure 4.4). The dataset generation workflow proceeded as follows:

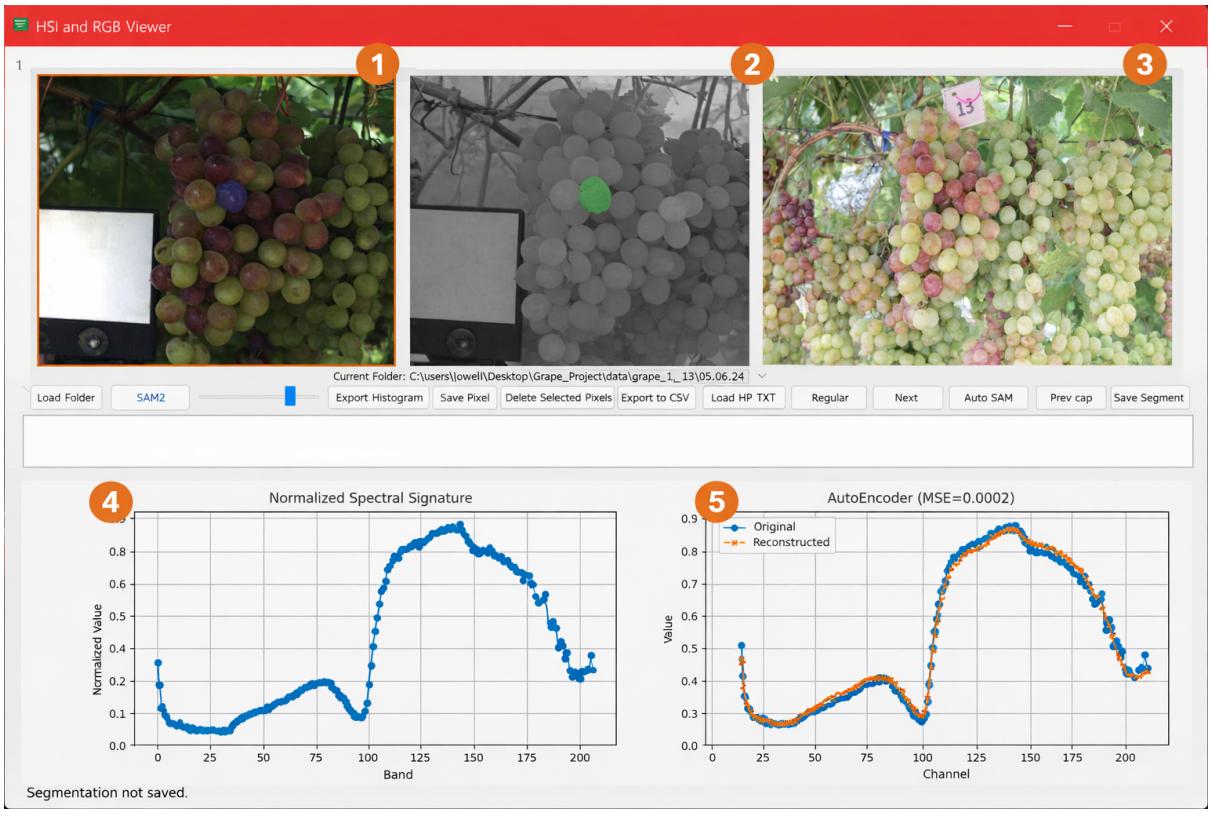

Figure 4.4: Graphical user interface of the HSI – RGB annotation tool. (1) Hyperspectral image visualized as an RGB composite with a SAM2-generated segmentation overlay, (2) wavelength-selectable grayscale HSI band with the same SAM2 segmentation mask, and (3) RGB image of the same grape cluster captured on the same day using a Canon EOS R5. (4) Spectral signature extracted from a single pixel within the SAM2-segmented region, and (5) autoencoder reconstruction of the same spectral signature, discussed later in this work.

1. **Image Loading and Visualization:** The tool displayed the hyperspectral datacube alongside corresponding RGB images (HSI camera and Canon EOS R5). A slider enabled interactive exploration of all 204 spectral bands (400–1000 nm).

2. **Interactive Pixel Sampling:** The user selected a seed pixel by clicking anywhere on a target object in either the RGB or HSI image. For the binary dataset, berries exhibiting clear cracked or healthy states were selected.

3. **SAM2 Segmentation on RGB:** The seed pixel was passed to **Segment Anything Model 2 (SAM2)** Ravi et al., 2024 as a point prompt. SAM2 operated on the RGB image to generate a binary segmentation mask of the selected object. This mask was then spatially aligned and applied to the corresponding hyperspectral datacube to identify the same region.

4. **HSI Data Extraction and Labeling:** The tool extracted spectral signatures from the hyperspectral datacube for all pixels within the segmented region. The user assigned a class label (e.g., 'Cracked' or 'Regular' for binary classification) to the object, and the annotated spectral data were stored.

The final exported binary pixel-level dataset used in this work contains 94,166 labeled pixels (24,548 CRACK; 69,618 REGULAR), as summarized in Table 4.3.

4.1.6 Expansion to Multi-Class Dataset

The binary pixel-level dataset contained two classes: healthy grape tissue and cracked grape tissue. A multi-class pixel-level dataset was constructed to include additional classes representing non-grape objects present in vineyard scenes. This dataset was designed for training multi-class classifiers and whole-image semantic segmentation models, as specified in Hypothesis 3.

The same annotation workflow was applied to acquire spectral samples from background objects. Seed pixels were selected on target objects (leaves, branches, soil, artificial materials, imaging equipment) in the RGB or HSI images. SAM2 segmented each selected object on the RGB image, and the resulting mask was applied to the hyperspectral datacube. Spectral signatures were extracted for all pixels within each segmented region. Each region was assigned a class label, and the labeled spectral samples were stored.

The multi-class dataset comprised ten classes:
The class distribution and dataset size are reported in Table 4.5. The multi-class dataset was exported as labeled spectral samples and used for training supervised multi-class classification models.

Class	Description
CRACK	Grape tissue with visible surface cracks
REGULAR	Intact grape tissue
LEAF	Green vine foliage
BRANCH	Woody vine structures (stem, cane)
BACKGROUND	Soil, ground, and mixed non-object pixels
PLASTIC	Plastic vineyard elements (covers, ties)
TRIPOD	Camera tripod components
WHITE_REFERENCE	Calibration panel pixels
BURNT_PIXEL	Saturated or overexposed pixels
IRON	Metal objects (wires, stakes)

Table 4.6: Multi-class dataset: class definitions.

4.1.7 Whole-Image Dataset Construction and Experimental Design

Dataset Composition

The whole-image dataset is defined at the *(grape_id, week_date)* level, where each record corresponds to a single hyperspectral image of a grape cluster. Sample counts and class distributions for all experimental subsets are reported in Table 4.3.

Spatial Partitioning

A row-based spatial partitioning scheme was applied to ensure physically disjoint datasets. All records acquired from vineyard Row 1 were assigned to the calibration set, while records from Row 2 were reserved as a held-out evaluation set. The two rows are spatially separated within the experimental vineyard, minimizing spatial autocorrelation and preventing information leakage between sets.

Subset Usage Protocol

The calibration set (Row 1) was used for model training and for internal parameter calibration of the whole-image inference procedure. The held-out test set (Row 2) was used exclusively for final performance evaluation and was not involved in model training, parameter tuning, or threshold selection.

Training Data Definition

The whole-image pipeline used a pretrained pixel-level classifier. The pixel-level model was trained on spectral signatures (pixels) sampled from Late-stage images in vineyard Row 1 only. Early-stage records were excluded from pixel-level training.

Whole-image hyperparameter tuning was performed using Row 1 only. Tuned parameters included the spatial aggregation and post-processing settings used to convert pixel-level

scores into image-level outputs (e.g., patch aggregation thresholds, crack-pixel criteria, and blob filtering parameters such as minimum/maximum region area).

Inference on the Held-out Evaluation Set

After training and calibration, the finalized model and inference parameters were applied to the held-out evaluation set (Row 2) without modification.

Post-Inference Acquisition-Stage Stratification

Following inference, outputs were stratified by acquisition stage for reporting. Stage labels were assigned according to vineyard monitoring records:

1. **Late-stage:** Images acquired after the first recorded cracking event, representing an advanced cracking condition.
2. **Early-stage:** The earliest available image associated with the onset of cracking for the same cluster, representing the initial observable stage.

Both Early-stage and Late-stage results were generated using the same trained pixel-level model. Whole-image inference parameters were tuned separately for Early-stage and Late-stage using Row 1 and then applied to the corresponding stage-specific records in the held-out evaluation set (Row 2).

Row split → Train pixel-level model on pixels from Late-stage (Row 1) → Tune full-image aggregation hyperparameters on Row 1 (separately for Early/Late) → Freeze parameters → Inference on held-out evaluation set (Row 2) → Stage-specific reporting (Early/Late)

Figure 4.5: Protocol overview for the row-based split, training and calibration on Row 1 Late-stage data, held-out evaluation on Row 2, and post-inference reporting stratified by acquisition stage.

4.2 Modeling and Evaluation Methodology

This section describes the modeling framework and evaluation protocols employed to analyze hyperspectral data for grape crack detection and early-warning screening. The methodology is structured to progressively assess spectral discriminability, define appropriate problem formulations, and evaluate model generalization from pixel-level classification to whole-image detection, while maintaining reproducibility and methodological consistency across experiments.

4.2.1 Global Spectral Preprocessing

All hyperspectral data were subjected to a unified and fixed preprocessing pipeline prior to any modeling or evaluation. This preprocessing was applied consistently across all datasets, models, and experimental settings to ensure methodological uniformity, reproducibility, and fair comparability between experiments Thenkarail et al., 2016.

Spectral Range Selection

To avoid the inclusion of spectral regions characterized by consistently low signal-to-noise ratios, the raw spectral signatures were restricted to a predefined wavelength range of 450–925 nm. Preliminary analysis of the data revealed high variance at the spectral extremities (400–450 nm and 925–1000 nm). This observation aligns with previous performance evaluations of the Specim IQ camera; notably, Behmann et al. Behmann et al., 2018 reported increased noise levels in the 400–450 nm range and significant reflectance artifacts in the near-infrared region (specifically above 925 nm) under outdoor conditions. Consequently, this effective operating range was selected once and retained throughout the study to avoid experiment-specific preprocessing decisions and to ensure consistency across all analyses Bioucas-Dias et al., 2013.

This wavelength window was treated as a *global* design choice rather than a tunable hyperparameter: it was fixed prior to model development and kept identical for all cross-validation folds, feature-selection experiments, and final held-out tests.

Quality Control and Outlier Handling

Hyperspectral datacubes were analyzed in normalized reflectance units, where spectral values are expected to lie within the physically valid range $[0, 1]$. Due to field acquisition conditions and imperfect radiometric normalization, isolated violations of this range may occur and indicate technically corrupted measurements rather than biological variability.

Per-Spectrum Normalization

Following quality control, each remaining spectral vector was normalized independently using *Standard Normal Variate* (SNV) on a per-pixel basis. In this transformation, each spectrum was mean-centered and scaled by its standard deviation to reduce additive and multiplicative effects associated with illumination variability, surface geometry, and scattering, while preserving relative spectral shape. SNV is widely used in close-range hyperspectral imaging for reducing non-chemical variability without distorting discriminative spectral features Barnes et al., 1989; Mishra et al., 2017; Späth et al., 2024.

4.2.2 Spectral Discriminability and Informative Wavelength Analysis

Prior to model development, a wavelength-wise separability assessment was conducted to verify that cracked and healthy grape tissues exhibit distinguishable spectral signatures and to localize the spectral regions contributing to class contrast across the VIS–NIR range.

Separability was quantified directly from the pixel-level spectra using three model-agnostic metrics computed at each wavelength: absolute mean difference $|\Delta\mu|$, Cohen's d effect size, and a Fisher-style discriminant ratio. These measures capture both effect magnitude and variance-normalized class separation.

The analysis was used solely to characterize the spectral distribution of cracked–healthy contrast and to support interpretation of the spectral-signature trends reported in the Results. No wavelength subset was selected based on these metrics.

4.2.3 Pixel-Level Classification Framework

Pixel-level classification was performed to evaluate whether spectral signatures of individual pixels could discriminate cracked grape tissue from healthy tissue and background materials. Each pixel was treated as an independent observation represented by its SNV-normalized reflectance spectrum.

Problem Formulation and Class Definitions

Two classification settings were evaluated:

- **Binary classification:** Pixels were assigned to one of two classes—*Healthy* (negative class, y=0) or *Cracked* (positive class, y=1)—based on visual assessment of the corresponding berry tissue during manual annotation.
- **Multi-class classification:** The binary formulation was extended to include explicit background classes representing non-berry materials commonly present in vineyard scenes (leaves, branches, soil, and artificial supports). Three multi-class evaluation modes were investigated:
  - *CRACK VS REST*: Binary formulation treating *Cracked* as positive.
  - *3-CLASSES*: Grouping samples into *Healthy*, *Cracked*, and *not-grape*.
  - *FULL MULTI-CLASS*: Preserving all 10 original class labels.

Feature Representation and Model Training

Each pixel was represented by its SNV-normalized reflectance vector across the 450–925 nm spectral range (159 bands at ∼3 nm spacing). No dimensionality reduction or

feature selection was applied prior to classification; the full spectral signature was used as input to enable assessment of intrinsic separability without imposed constraints.

The following supervised learning algorithms were evaluated:

- Partial Least Squares Discriminant Analysis (PLS-DA)
- Logistic Regression with L1 regularization
- Support Vector Machine with RBF kernel (SVM-RBF)
- Random Forest
- Gradient-boosted decision trees (XGBoost, used as baseline)
- Shallow multi-layer perceptron (MLP)

XGBoost was adopted as the baseline classifier for all primary comparisons due to its robustness to high-dimensional correlated features.

Both balanced and unbalanced training regimes were investigated. Under the unbalanced regime, the natural class distribution was preserved. Under the balanced regime, all classes were undersampled to match the minority class count. For binary classification, majority-class samples were randomly undersampled. For multi-class settings, segment-proportional undersampling was applied: each class was capped at the *Cracked* class count, with samples drawn proportionally from each segment (mask region) to preserve within-class diversity. Models were trained using default or lightly tuned hyperparameters; no extensive grid search was performed.

Cross-Validation Protocol

To assess generalization to unseen biological samples, Leave-One-Group-Out (LOGO) cross-validation was applied at the grape-cluster acquisition level. LOGO was selected due to the limited number of available hyperspectral images, which precluded a simple held-out test set while still requiring rigorous evaluation of cluster-level generalization. All pixels extracted from the same hyperspectral image (corresponding to a unique grape cluster) were assigned exclusively to either the training set or the test set within each fold. This grouping strategy ensured that evaluation was performed on spectral signatures from previously unseen clusters, preventing spatial or spectral leakage between partitions.

For the multi-class formulation with background classes, a domain-aware variant was used: LOGO folds were defined over grape-containing acquisitions, while non-grape background samples were assigned to a fixed grouped holdout split (80/20) to prevent leakage across semantically distinct domains.

Evaluation Metrics

Classification performance was quantified using metrics selected for their interpretability under class imbalance. The primary ranking metric for pixel-level classification was

Precision–Recall Area Under the Curve (PR–AUC) for the *Cracked* class, computed with *Cracked* treated as the positive class. PR–AUC was preferred over ROC–AUC because its baseline corresponds to the positive-class prevalence, making it more informative when the minority class is of primary interest.

Additional metrics reported included: Accuracy, Balanced Accuracy (macro-average of per-class recall), Precision and Recall for the *Cracked* class, macro-average F1-score, and ROC–AUC for the *Cracked* class. These metrics were computed per fold and summarized as mean ± standard deviation across folds. Threshold-dependent metrics (Precision, Recall, F1) used the model's default decision rule; for probabilistic classifiers, the standard threshold of 0.5 was applied to predicted probabilities.

4.2.4 Anomaly Detection Framework

One-Class Formulation

An anomaly detection framework was implemented at the pixel level using a one-class learning paradigm. Models were trained exclusively on spectral signatures designated as *normal*, and unseen samples were flagged as anomalous based on deviation from this learned distribution.

Definition of Normality per Variant

Three experimental configurations were evaluated, each defining normality differently:

- **Binary one-class:** Normal class comprised Healthy/Regular pixels; anomalies were Cracked pixels.
- **Multi-class (all except Cracked):** Normal class comprised all nine non-*Cracked* classes; anomalies were *Cracked* pixels.
- **Multi-class (Cracked only):** Normal class comprised *Cracked* pixels exclusively; anomalies were all other classes.

Data Partitioning and Leakage Control

Cross-validation strategies were adapted to each variant's data structure:

- **Binary one-class:** Leave-One-Group-Out (LOGO) at the grape-cluster acquisition level, matching the supervised classification protocol (§4.2.3).
- **Multi-class (all except Cracked):** Single grouped train/test split (80/20) stratified by acquisition.
- **Multi-class (Cracked only):** Domain-aware cross-validation combining LOGO over *Cracked*-containing acquisitions with a fixed grouped 80/20 split for non-*Cracked* samples to prevent segment leakage.

For binary one-class IsolationForest (contamination = 0.05) was applied to remove outliers from the training normal set prior to autoencoder fitting.

Spectral Preprocessing

Pixels were preprocessed as described in §4.2.1. Specifically, SNV normalization was applied per spectrum, and the retained wavelength range was 450–925 nm (159 bands at ∼3 nm spacing).

Autoencoder Architecture and Training

All anomaly detection experiments employed a fully connected autoencoder with symmetric encoder–decoder structure. The encoder applied ReLU activations, BatchNorm, and dropout ($p = 0.2$) in the first two layers. Several bottleneck sizes were evaluated.

Let $x \in \mathbb{R}^D$ denote a preprocessed spectrum and $\hat{x}$ its reconstruction. Training minimized $\mathrm{MSE}(x, \hat{x})$, with hyperparameters listed in Table 4.7.

Parameter	**Value**
Optimizer	Adam
Learning rate	10^{-3}
Weight decay	10^{-5}
LR scheduler	ReduceLROnPlateau (patience=5, factor=0.5)
Early stopping	patience=15
Max epochs	100
Batch size	256

Table 4.7: Autoencoder training hyperparameters.

Anomaly Scoring and Thresholding

The anomaly score was defined as the per-sample reconstruction mean squared error:

$$e(x) = \frac{1}{D} \|x - \hat{x}\|_2^2. \tag{4.1}$$

For each fold or split, an operating threshold τ was computed as the 99th percentile of reconstruction errors on the training partition of the normal class. A sample was classified as anomalous if $e(x) > \tau$.

Integration into Whole-Image Inference

For full-image inference, the multi-class autoencoder variant trained on CRACK samples only was selected and exported. This model was integrated into the full-image inference

pipeline, transforming reconstruction errors into probability-like crack scores via sigmoid mapping:

$$p_{\text{CRACK}}(x) = \frac{1}{1 + \exp\left(\frac{e(x)-\tau}{\alpha}\right)}, \tag{4.2}$$

where $e(x)$ is the reconstruction error for spectrum x, τ is the training threshold (99th percentile of CRACK class errors), and α is a temperature parameter ($\approx 0.3\tau$) controlling transition sharpness. This mapping produces a smooth S-curve: low reconstruction errors (CRACK-like) map to high probability, while high errors (anomalous) map to low probability. Per-pixel scores were subsequently processed through standard post-processing and aggregation stages.

4.2.5 Dimensionality Reduction Strategy

Dimensionality reduction was investigated as a secondary analysis step at the pixel level, following validation of baseline models on the full spectral representation. As formulated in §4.2.3, wavelength selection was evaluated separately for binary (*Cracked* vs. *Healthy*) and multi-class (with background classes) settings.

Spectral Preprocessing

Pixels were preprocessed as described in §4.2.1. SNV normalization was applied per spectrum, and the spectral range was restricted to 450–925 nm, yielding 159 bands at approximately 3 nm spacing.

Classification Model

XGBoost was used as the fixed classifier for all wavelength selection experiments, selected as the best-performing model from the preceding pixel-level classification work (§4.2.3).

Two Experimental Settings

Wavelength selection was performed in two independent experiments:

- **Binary setting:** Wavelengths selected for *Cracked* vs. *Healthy* classification.
- **Multi-class setting:** Wavelengths selected for multi-class classification with background classes.

Train-Test Split Protocol

For each experimental setting, a single grouped 80/20 held-out split was constructed with group constraints to prevent leakage. For binary classification, the grouping was by grape cluster identity (*CRACK* and *REGULAR* samples). For multi-class classification, grouping was by cluster/segment identity for background classes. The 80% training subset

was used to re-train XGBoost at each BFS step, while the held-out 20% test subset served as the invariant selection criterion throughout the elimination path.

Backward Feature Selection (BFS)

A deterministic wrapper method was applied, starting from the full set of 159 wavelengths and iteratively removing the least informative band at each step. At each removal step, the classifier was re-trained on the 80% training subset and evaluated on the held-out 20% test subset. The selection metric was PR–AUC for the *Cracked* class. BFS provides a monotonic elimination path, identifying the minimal wavelength subset preserving near-baseline detection performance.

4.2.6 Whole-Image Detection and Aggregation Pipeline

Building upon the pixel-level classification outputs, a whole-image detection and localization pipeline was developed to enable robust crack identification in realistic vineyard scenes. Rather than introducing an additional image-level classifier, the pipeline aggregates pixel-level classification outputs into a system-level framework that enforces spatial coherence and suppresses isolated false positive responses.

The pipeline operates on pixel-wise crack probability maps generated by the trained pixel-level classifiers and progressively aggregates them into region-level, patch-level, and image-level decisions, bridging the gap between noisy pixel-level outputs and biologically meaningful image-level interpretation.

All pixel-level models—including the base classifiers, autoencoder variants, and wavelength-reduced models from dimensionality reduction—were fixed at their trained states. No retraining, tuning, or optimization of these models was performed at the whole-image level.

Pipeline Architecture and Spatial Aggregation

The whole-image aggregation pipeline follows a sequential process, illustrated in Figure 4.6, and consists of the following stages:

- **Input Hyperspectral Image:** Each input consists of a full hyperspectral datacube ($H \times W \times B$) acquired under field conditions.
- **Pixel-Level Probability Map Generation:** The trained pixel-level classifier produces a dense pixel-wise crack probability map with values in the range $[0, 1]$.
- **Morphological Closing and Region Formation:** Spatially adjacent pixels with elevated crack probabilities are grouped into connected regions (BLOBs) using morphological closing operations, enforcing spatial coherence.

- **Blob Size Filtering:** Small connected regions below a minimum size threshold are removed to suppress isolated false positive detections.
- **Patch-Based Division and Decision:** The image is divided into fixed-size patches. A patch is marked as crack-positive if the proportion of crack-related pixels within the patch exceeds a predefined threshold.
- **Image-Level Decision:** The final image-level decision is obtained by aggregating patch-level outcomes. An image is classified as *Cracked* if at least one patch is identified as crack-positive; otherwise, it is classified as *Non-Cracked*.

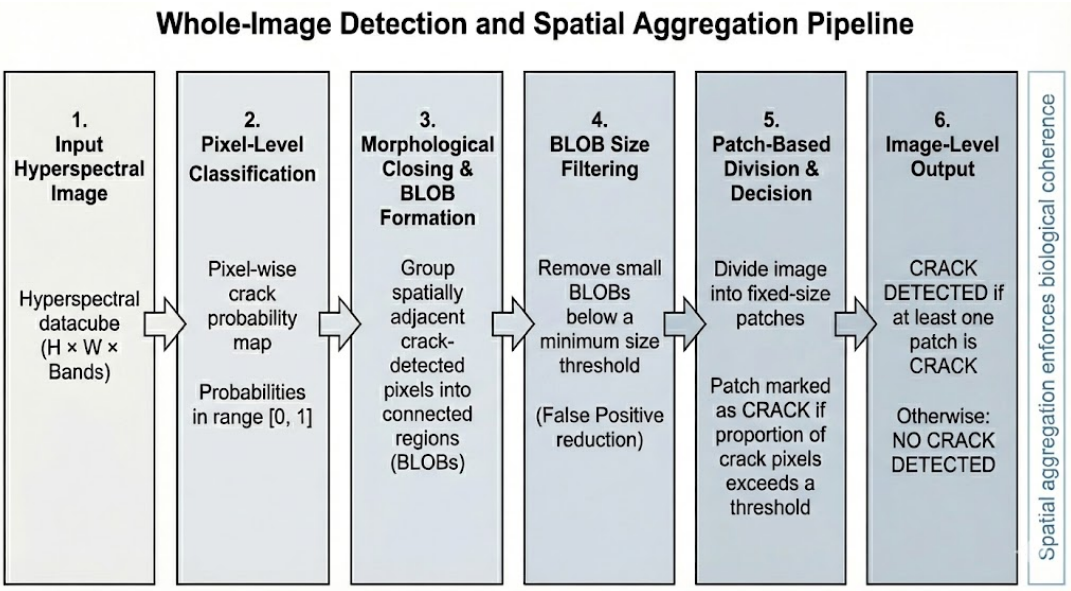

Figure 4.6: Whole-image crack-detection pipeline applied to field-acquired cluster scenes (early and late settings) with row-partitioned evaluation (Row 1 calibration, Row 2 test). A pixel-level classifier produces a crack probability map ($[0, 1]$), which is spatially aggregated via morphological closing and blob-size filtering; patch rules are then combined into a final image-level decision (Cracked vs.
Non-Cracked). Takeaway: spatial aggregation turns noisy pixel scores into a deployable cluster-level decision rule.

Whole-Image Dataset and Evaluation Setup

Whole-image evaluation was conducted on the row-partitioned inference dataset described in Section 4.1.7. The aggregation pipeline was applied to patch-based representations extracted from the full images, enabling localized detection while preserving image-level context. Row 1 was used exclusively for calibration/tuning of whole-image inference parameters, while Row 2 was reserved as a held-out test set for final reporting. Exact sample counts and class balance (early/late) are reported in Table 4.3.

Evaluation Across Disease Progression Stages

To assess robustness across different stages of crack development, whole-image performance was evaluated separately for early-stage and late-stage samples. Late-stage images contained clusters with clearly visible macroscopic cracking, whereas early-stage images corresponded to initial onset (absent-to-minimal/incipient cracking) based on expert monitoring records and visual inspection. This stratification was applied exclusively at the evaluation stage and did not affect model training or aggregation design.

4.2.7 Evaluation Protocols and Performance Metrics

Model performance was evaluated using task-specific protocols and metrics tailored to each stage of the analysis, reflecting the differing objectives and operational requirements of pixel-level classification, anomaly detection, and whole-image detection.

Evaluation metrics were selected according to the objective of each experimental stage. Pixel-level and anomaly detection metrics are summarized in Table 4.9, while system-level evaluation for whole-image detection is reported in Table 4.10.

Metrics Rationale

This study spans multiple tasks with different operating assumptions (pixel-level detection under strong class imbalance, system-level whole-image decisions after spatial aggregation, and wavelength-selection optimization). Accordingly, a task-dependent *primary* metric is defined for each setting, while additional metrics are reported to describe operating-point behavior and error trade-offs.

Pixel-level detection (binary and multi-class). The pixel-level objective is to detect cracked tissue, which is typically the minority class. Therefore, the primary ranking metric is **PR–AUC for the *Cracked* class** (computed with *Cracked* as the positive class; one-vs-rest in multi-class settings). PR–AUC (average precision) is preferred under class imbalance because it focuses on precision–recall trade-offs and its baseline corresponds to the positive-class prevalence, making it more informative than ROC–AUC when negatives dominate. Threshold-dependent metrics (Precision/Recall and, where reported, F1) are included as complementary operating-point summaries. Unless explicitly subscripted (e.g., $\mathrm{F1}_{\mathrm{CRACK}}$), reported **F1 refers to the weighted F1-score** (support-weighted over classes), matching the evaluation scripts used in the experiments.

Whole-image crack classification (spatial aggregation). At the image level, performance is reported with explicit emphasis on the *Cracked* class. The *primary* summary metric is $\mathbf{F1_{CRACK}}$, supported by $\mathbf{Precision_{CRACK}}$ and $\mathbf{Recall_{CRACK}}$ to expose the false-positive/false-negative trade-off at the chosen operating point. **MCC** is reported

as a complementary single-number summary that remains informative under class imbalance. Image-level accuracy is included for completeness, but it is not treated as the main indicator of crack-detection quality. $\mathbf{F2_{CRACK}}$ is additionally reported when a recall-oriented operating point is of interest.

Backward Feature Selection (BFS) optimization. For BFS, the objective metric is **CRACK PR–AUC** evaluated on a fixed grouped 80/20 hold-out split (Section 4.2.5). CRACK F1 is additionally plotted to show how feature elimination affects threshold-dependent performance, but selection is driven by the PR–AUC criterion.

Reporting and threshold conventions. For cross-validation experiments (pixel-level classification and LOGO anomaly detection), metrics are computed per held-out fold and summarized as mean ± standard deviation across folds. ROC–AUC and PR–AUC are computed from continuous scores/probabilities and do not require selecting a decision threshold. Metrics that require binary decisions (Precision/Recall/F1/F2/MCC) use the model's hard class labels under its standard decision rule; for the PLS-DA wrapper this corresponds to thresholding the continuous score at $t = 0.5$. For one-class autoencoder experiments, the anomaly threshold is estimated on the training partition of each fold using a percentile of training reconstruction errors and then applied unchanged to the held-out fold. For whole-image experiments, post-processing parameters (including probability and aggregation thresholds) are calibrated on Row 1 only and then fixed for reporting on the held-out Row 2 test set.

Cross-Validation Strategy

To assess generalization across biologically independent samples and prevent spatial or spectral data leakage, group-aware evaluation protocols were employed. Where cross-validation was used, Leave-One-Group-Out (LOGO) was applied at the grape-cluster acquisition level so that all pixels originating from the same grape cluster (or the same hyperspectral acquisition of a cluster) were assigned exclusively to either training or test within a fold. For multi-class settings with explicit background/distractor classes, a domain-aware variant was additionally used in which grape (or CRACK-containing) groups define LOGO folds while non-grape samples are assigned to a fixed grouped hold-out split.

This strategy ensures that evaluation is performed on previously unseen biological samples and provides a realistic estimate of model performance under field deployment conditions.

Across all reported protocols, leakage prevention was enforced by design: the wavelength restriction (450–925 nm) is fixed globally, SNV is computed independently per spectrum, and any data-dependent operation that requires fitting parameters or selecting features is carried out using only the training partition of the relevant protocol (or Row 1 for whole-image calibration) and then applied to held-out groups (or Row 2) without adaptation.

Evaluation Units and Split Strategy

Table 4.8 provides a compact summary of the unit of analysis and the exact independence assumptions used across all reported experiments.

Table 4.8: Evaluation units and split strategy used across experiments. "Independent test" denotes the data that remain unseen during fitting/tuning for the corresponding protocol.

Experiment / task	Unit	Split strategy (group definition)	Independent test
Binary pixel-level classification (2 classes)	Pixel spectrum	LOGO cross-validation with group = `cluster_id` extracted from `hs_dir` (three levels up in the path). All pixels from a held-out cluster are evaluated together.	Held-out LOGO fold (one cluster group)
Multi-class pixel-level classification (domain-aware LOGO)	Pixel spectrum	LOGO applied to grape samples with group = `hs_dir` (image-level identifier), combined with a fixed 80/20 grouped hold-out split for non-grape/background samples (by `hs_dir`, with fallback to `mask_path` if required). Each fold tests one held-out grape image plus the fixed non-grape hold-out set.	Per fold: held-out grape `hs_dir` + fixed non-grape hold-out
CRACK-focused domain-aware CV (unified pipeline)	Pixel spectrum	LOGO applied to CRACK samples only with group = CRACK `hs_dir`; REGULAR samples use a fixed 80/20 grouped split (by `mask_path`); non-grape samples use a fixed 80/20 grouped split. The same fixed REGULAR/non-grape hold-out portions are reused across folds.	Per fold: held-out CRACK `hs_dir` + fixed REGULAR/non-grape hold-out
Autoencoder anomaly detection (one-class; LOGO)	Pixel spectrum	LOGO cross-validation with group = `cluster_id` extracted from `hs_dir`. Scaling and threshold selection are computed from training partitions only.	Held-out LOGO fold (one cluster group)
Autoencoder anomaly detection (train on all except CRACK; single split)	Pixel spectrum	Single group-wise train/test split without LOGO: unique groups (`cluster_id` extracted from `hs_dir`) are split 80/20 into train/test groups. The autoencoder is trained on non-CRACK samples from training groups; evaluation is reported on held-out test groups.	Held-out 20% of groups (cluster_id)
Whole-image crack detection (spatial aggregation)	Patch; image (cluster acquisition)	Row-partitioned evaluation: Row 1 CSVs are used for calibration/tuning of post-processing parameters; Row 2 CSVs are held out for final testing. Early- and late-stage scenarios are evaluated separately.	Held-out Row 2 (early and late, separately)

Pixel-Level Classification Metrics

For binary pixel-level classification, performance was evaluated using both ranking-based metrics (ROC–AUC and PR–AUC with *Cracked* as the positive class) and operating-point metrics (Precision/Recall and F1). Under class imbalance, PR–AUC$_{\text{CRACK}}$ is treated as

the primary summary of separability, while Precision/$\text{Recall}_{\text{CRACK}}$ describe the trade-off at the operating point used by the classifier.

Additional metrics, including precision, recall, and ROC-AUC, were reported as supporting indicators to facilitate comprehensive performance analysis.

For multi-class pixel-level classification, Macro-F1 and per-class F1-scores were used as primary metrics to ensure balanced evaluation across all classes, with particular attention to the *Cracked* class. Confusion matrices were used to analyze class-specific error patterns and background-related confusions.

Anomaly Detection Evaluation

For anomaly detection experiments, model performance was evaluated using ROC-AUC and PR-AUC, reflecting the ranking-based nature of one-class detection and the absence of a fixed decision threshold. These metrics quantify the ability of the model to distinguish anomalous (cracked) spectra from normal (healthy) spectral behavior across a range of operating points.

Whole-Image and Patch-Based Evaluation

Whole-image detection performance was evaluated at the patch and image levels, reflecting the system-level objective of identifying cracked grape clusters under realistic field conditions.

Given the higher cost associated with missed detections, recall-oriented metrics were emphasized. In particular, Recall and the F2-score for the *Cracked* class (F2_{CRACK}) were used as primary evaluation criteria, assigning greater weight to recall than precision.

Precision and false positive rates were reported as complementary metrics to characterize trade-offs and system behavior. Quantitative evaluation was supported by qualitative visual inspection of detection overlays to analyze spatial consistency, typical failure modes, and false positive patterns.

Table 4.9: Evaluation metrics for pixel-level and anomaly detection experiments

Task	**Primary Metrics**	**Secondary Metrics**
Binary pixel-level classification	PR–$\text{AUC}_{\text{CRACK}}$, $\text{Recall}_{\text{CRACK}}$	$\text{Precision}_{\text{CRACK}}$, F1 (weighted unless specified), ROC–AUC
Multi-class pixel-level classification	Macro-F1, F1_{CRACK}	Per-class Precision/Recall, Confusion Matrix
Anomaly detection (one-class)	ROC-AUC, PR-AUC	Recall@Fixed-FPR, Precision@Top-K

4.2.8 Reproducibility and Implementation Details

This section summarizes the concrete implementation and execution details needed to rerun the experiments and reproduce the reported results. Where the project does not explicitly record a detail (e.g., exact CPU/GPU model), it is marked as **TODO: ...** rather than inferred.

Software Environment

All experiments were executed in a dedicated Python virtual environment located at `.venv`. The environment was created with **Python 3.11.9** (as recorded in `.venv/pyvenv.cfg`). Dependency versions were pinned in `requirements.txt`; core libraries used throughout the pipelines include:
`numpy==2.2.3`, `pandas==2.2.3`, `scikit-learn==1.6.1`, `xgboost==2.1.4`, and `torch==2.5.1+cu121`.

The codebase is developed and executed on Windows (paths and helper scripts use Windows conventions). **TODO: Record exact Windows version/build used for final runs (e.g., from system info) and archive it alongside experiment outputs.**

Randomness and Seed Strategy

Randomness is controlled explicitly in the main training and evaluation scripts. A project-wide default seed of **42** is used in multiple pipelines. For the one-class autoencoder experiments, the scripts define a `set_seed()` helper that sets seeds for `random`, `numpy`, and `torch` (and, when CUDA is available, `torch.cuda.manual_seed_all`), and enforces deterministic cuDNN behavior by setting `torch.backends.cudnn.deterministic=True` and `torch.backends.cudnn.benchmark=False`. In cross-validation settings, some runs additionally use fold-index offsets (e.g., `seed = 42 + fold_idx`) to ensure controlled but distinct fold-specific randomness.

For dataset construction steps that include sampling (e.g., selecting a bounded number of negative samples for full-image datasets), the seed is passed as an explicit `random_seed` argument with default `42`.

Outputs, Artifacts, and Result Storage

Experiment artifacts are written to the top-level `experiments/` directory using timestamped subfolders. For example, the unified pixel-level comparison pipeline creates an `experiments/unified_experiment_.../` folder and stores the exact run configuration in `experiment_config.json`, cross-validation manifests (`cv_split_manifest_*.json`), and consolidated reports exported to `.xlsx/.csv/.md`. Similarly, autoencoder experiments store fold-level and summary outputs (e.g., `all_fold_results.csv` and `summary_results.csv`) under timestamped `experiments/autoencoder_.../` directories.

TODO: For long-term reproducibility, archive each experiment folder together with the exact input dataset CSV(s) used, or their immutable hashes/versions.

How to Rerun Core Pipelines

Two helper scripts are provided to ensure the correct environment is used:

- `activate_venv.bat` activates `.venv` and opens a new `cmd` session.
- `run_with_venv.bat` runs a given Python command using `.venv`
  `Scripts`
  `python.exe`.

Representative entry points used in this thesis include:

- Unified pixel-level experiment pipeline (exports consolidated reports): src/models/classification/pixel_level/simple_classification_leave_one_out/comare_all_models_multi_class_16_01/unified_experiment_pipeline_acc.py.
- One-class autoencoder anomaly detection (LOGO and thresholding per fold): src/models/classification/pixel_level/simple_classification_leave_one_out/autoencoder_multiclass_30_01/autoencoder_anomaly_detection.py.
- Full-image dataset builder (creates Row 1/Row 2 CSVs; random seed controls sampling): src/datasets/full_image/builders/build_full_image_datasets.py.

The full-image inference application is a self-contained subproject under src/models/classification/full_image/inference_to_see_results_of_models/ and includes a reproducibility-focused smoke test (`scripts/smoke_test.py`) that reports the configured `RANDOM_SEED` and device.

TODO: Record the exact hardware used for final model training/inference (CPU model, RAM, GPU model/VRAM). For GPU runs, capture the device name printed by the scripts (e.g., `torch.cuda.get_device_name(0)`) and store it in the corresponding experiment folder.

Table 4.10: Evaluation metrics for whole-image and patch-based detection

Task	Primary Metrics	Secondary Metrics
System-level detection of cracked grape clusters	$F1_{CRACK}$, $Precision_{CRACK}$, $Recall_{CRACK}$	MCC, Image-level Accuracy, $F2_{CRACK}$, False Positive Rate

Chapter 5

Experimental Results

5.1 Overview of Experimental Results

This chapter presents the quantitative results obtained from the experimental evaluation of hyperspectral-based crack detection and early-warning screening methods. The results are organized to follow the logical progression of the experimental pipeline, beginning with spectral characterization and continuing through pixel-level and whole-image modeling, followed by wavelength-selection analyses.

Only empirical findings are reported in this chapter, without interpretation or comparison to prior studies.

5.1.1 Baselines

To support consistent comparisons across tasks, each set of results in this chapter is reported relative to an explicit baseline configuration:

- **Pixel-level classification baseline.** The baseline classifier is **XGBoost** trained on the **full hyperspectral signature** (450–925 nm) after **SNV normalization**. Baseline performance for the binary task is reported in the XGBoost rows of Table 5.3 and Table 5.4. For the extended labeling/balancing regimes, the corresponding XGBoost baselines appear in Table 5.5 and Table 5.6.

- **Whole-image crack-detection baseline.** The baseline whole-image system uses **pixel-level model outputs** as inputs to the same **spatial post-processing and aggregation pipeline** (thresholding, morphological filtering, patch-level aggregation, and image-level decision logic), **without any wavelength selection**. Its early/late calibration and held-out test performance is summarized in Table 5.14 (with dataset composition in Table 5.13).

- **BFS wavelength-selection reference.** BFS results are reported as **performance vs. number of selected wavelengths** relative to the **full-spectrum**

baseline (159 wavelengths within 450–925 nm). The performance trajectories are shown in Figure 5.4 and Figure 5.5, and the derived wavelength-count thresholds are summarized in Table 5.16. Whole-image test-set performance at representative wavelength counts (including the full-spectrum baseline at 159 wavelengths) is reported in Table 5.17.

5.2 Spectral Signature Characterization

This section examines the spectral properties of grape tissue to establish whether measurable differences exist between healthy and cracked samples prior to any modeling stage.

5.2.1 Mean Spectral Signatures of Healthy and Cracked Tissue

Mean spectral signatures were computed for pixels sampled from healthy and cracked grape tissue across the full VIS–NIR range. The analysis focuses on class-level spectral trends and variability, without fitting any classification model.

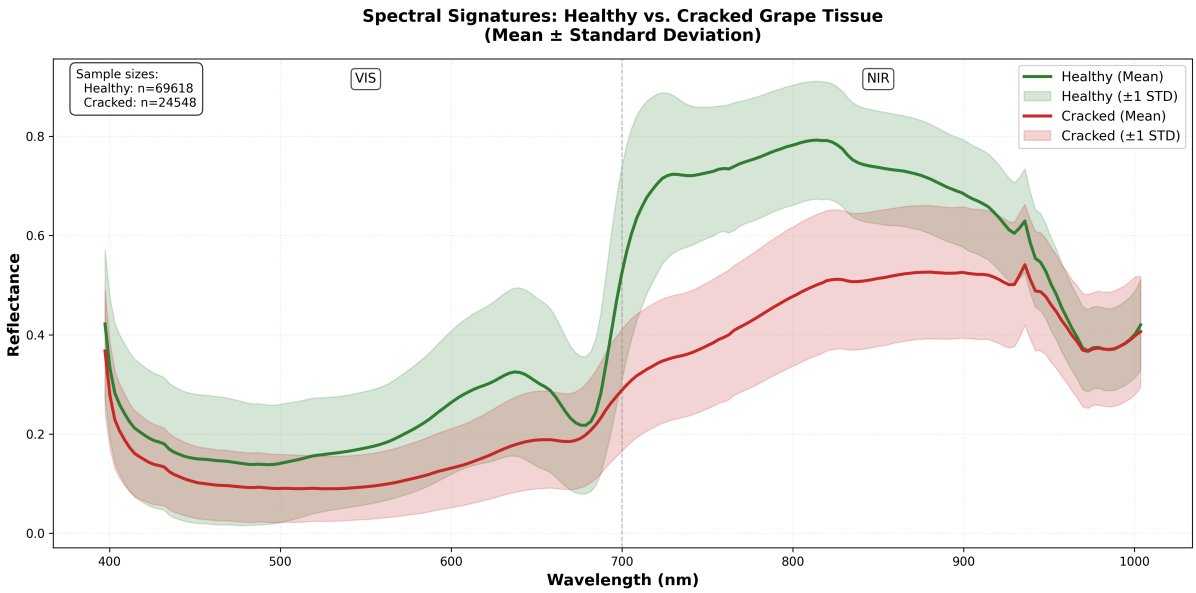

Figure 5.1: Mean spectral signatures (± standard deviation) for healthy and cracked tissue across the VIS–NIR range.

To provide a compact quantitative summary, reflectance values were aggregated over two broad spectral regions corresponding to the visible (VIS) and near-infrared (NIR) ranges.

Table 5.1: Summary statistics of reflectance values across spectral regions for healthy and cracked tissue.

Spectral Region	Class	Mean Reflectance	Std. Dev.	Median
VIS (400–700 nm)	Healthy	0.218	0.128	0.186
	Cracked	0.137	0.076	0.123
NIR (700–1000 nm)	Healthy	0.660	0.114	0.630
	Cracked	0.450	0.121	0.425

5.2.2 Spectral Separability Across Wavelength Regions

This subsection quantifies the degree of spectral separation between healthy and cracked tissue across predefined wavelength regions. The goal is to identify spectral ranges exhibiting the strongest inter-class contrast, without invoking classification models.

To facilitate regional-level comparison, the wavelength-wise separability measures were aggregated over predefined spectral regions.

Table 5.2: Regional spectral separability metrics between healthy and cracked tissue. Mean values are averaged across wavelengths within each range, while peak values indicate the maximum separability and the corresponding wavelength.

Metric	VIS Range	NIR Range	Full Spectrum
Mean $\lvert\Delta\mu\rvert$ (Abs. Mean Diff.)	0.0810	0.2101	0.1422
Max $\lvert\Delta\mu\rvert$ (nm)	0.2325 (708.6)	0.3704 (726.5)	0.3704 (726.5)
Mean Cohen's d	0.6330	1.6217	1.1014
Max Cohen's d (nm)	1.1910 (699.5)	2.6877 (756.6)	2.6877 (756.6)
Mean Fisher Score	0.2895	1.6590	0.9436
Max Fisher Score (nm)	0.8821 (694.5)	3.6311 (747.5)	3.6311 (747.5)

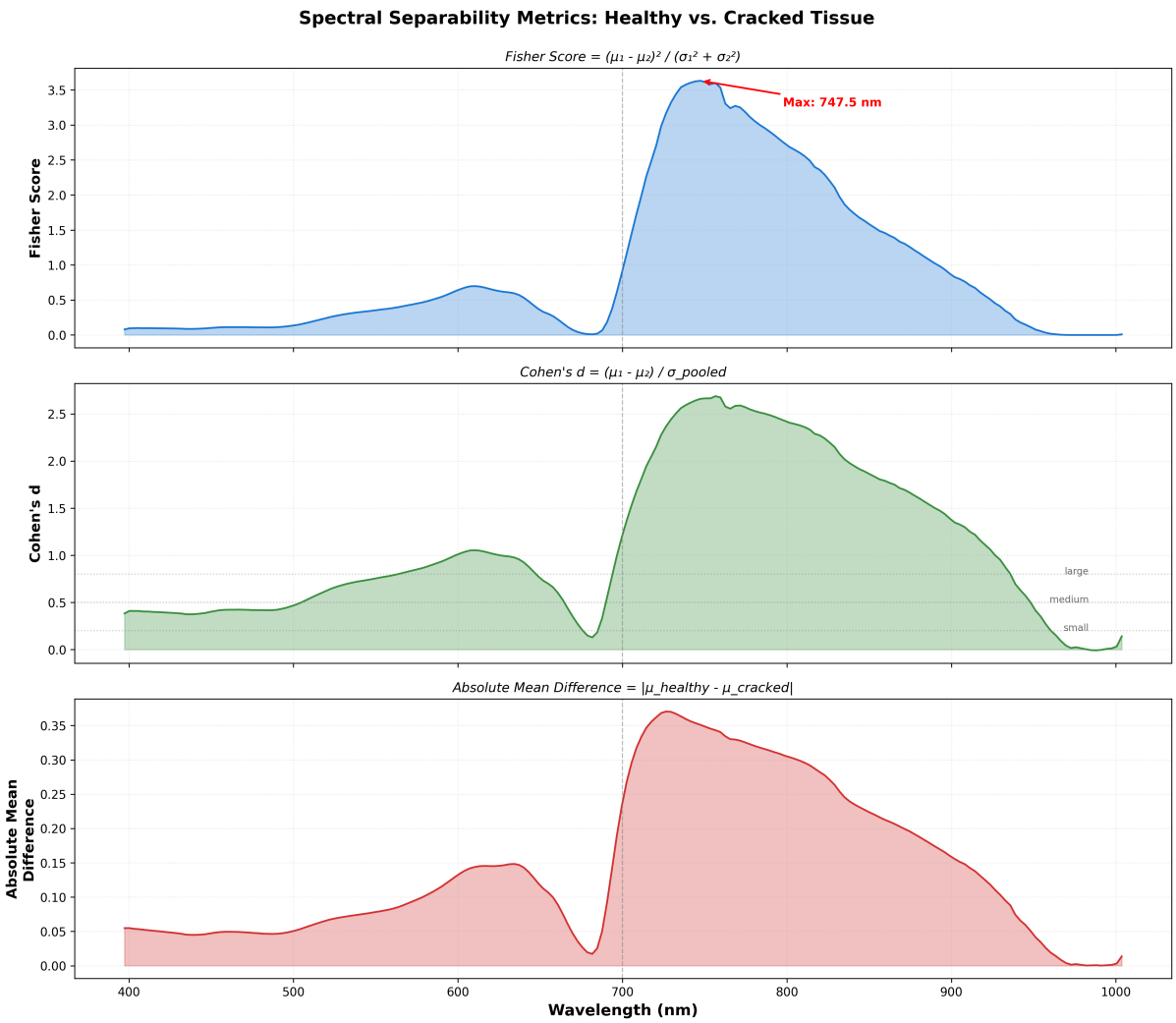

Figure 5.2: Wavelength-wise spectral separability metrics between healthy and cracked tissue, including absolute mean difference, Cohen's d, and Fisher score.

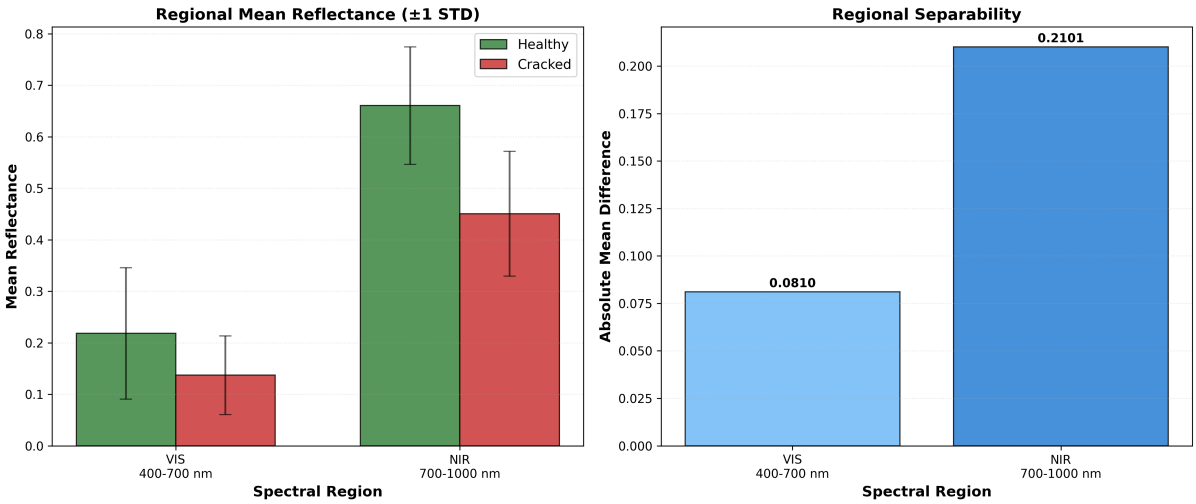

Figure 5.3: Regional visual summary of mean reflectance (±1 STD) and absolute mean difference between healthy and cracked tissue in the VIS and NIR ranges. This figure provides an intuitive visualization of the regional trends quantified in Table 5.2.

Figures 5.2 and 5.3, together with Table 5.2, quantify wavelength-wise and regional separability between healthy and cracked tissue without invoking a classifier. The next section evaluates whether supervised learning models can exploit these measured differences to discriminate cracked pixels under the group-aware protocol. Binary and extended labeling results are reported in Tables 5.3–5.4 and Tables 5.5–5.6.

5.3 Pixel-Level Classification Performance

This section reports the performance of supervised pixel-level classification models trained on hyperspectral signatures.

5.3.1 Experimental Setup and Evaluation Protocol

Pixel-level classification performance was evaluated using a cross-validation framework designed to assess generalization across grape clusters. Standard classification metrics were computed for all experiments. For a compact summary of the evaluation units and split strategies used across all experiments (pixel-level, anomaly detection, and whole-image), see Table 4.8.

5.3.2 Binary Pixel-Level Classification Results

Binary pixel-level classification was evaluated for distinguishing healthy from cracked tissue. Performance was assessed using ranking-based metrics (ROC–AUC and, where reported, PR–AUC) together with class-specific Precision and Recall for the *Cracked* class (positive class). Under class imbalance, PR–AUC$_{\text{CRACK}}$ is treated as the primary separability metric (see Section 4.2.7).

Two sampling regimes were considered: the original naturally imbalanced distribution and a class-balanced configuration.

Unbalanced vs. Balanced Training Sets

Results obtained under both sampling regimes are summarized jointly on the following landscape page. Table 5.3 reports the classification performance obtained using the original unbalanced dataset, while Table 5.4 presents the corresponding results obtained under balanced sampling. The identical evaluation protocol and model set are used in both cases, enabling a direct comparison between regimes.

Uncertainty and statistical comparisons. Tables 5.3 and 5.4 report mean ± standard deviation across cross-validation folds. These descriptive summaries indicate variability across folds, but they do not by themselves quantify uncertainty of *differences*

between models or sampling regimes. Accordingly, claims in this section are interpreted descriptively; no hypothesis tests or confidence intervals for model-to-model differences are reported. A stronger comparison would require retaining fold-wise metric values (or per-sample model outputs with fold/group identifiers) and applying a paired procedure (e.g., a paired bootstrap or permutation test over folds/groups).

Table 5.3: Pixel-level classification metrics (unbalanced training set). Values are reported as mean ± standard deviation across folds where available. Precision/recall and ROC–AUC refer to the *Cracked* class (positive class); F1 is the weighted F1-score.

Model	Accuracy	Precision (Cracked)	Recall (Cracked)	Weighted F1	ROC–AUC (Cracked)
PLS-DA	0.9927 ± 0.0168	0.9999	0.9682	0.9924	1.0000 ± 0.0000
Logistic Regression (L1)	0.9962 ± 0.0074	0.9890	0.9948	0.9963	0.9996 ± 0.0012
SVM (RBF)	0.9938 ± 0.0094	0.9943	0.9787	0.9938	0.9997 ± 0.0010
Random Forest	0.9968 ± 0.0055	0.9964	0.9904	0.9968	0.9990 ± 0.0035
XGBoost	0.9947 ± 0.0103	0.9953	0.9798	0.9946	1.0000 ± 0.0000

Table 5.4: Pixel-level classification metrics (balanced training set). Values are reported as mean ± standard deviation across folds where available. Precision/recall and ROC–AUC refer to the *Cracked* class (positive class); F1 is the weighted F1-score.

Model	Accuracy	Precision (Cracked)	Recall (Cracked)	Weighted F1	ROC–AUC (Cracked)
PLS-DA	0.9961 ± 0.0086	0.9998	0.9929	0.9961	1.0000 ± 0.0000
Logistic Regression (L1)	0.9930 ± 0.0148	0.9994	0.9861	0.9930	0.9999 ± 0.0002
SVM (RBF)	0.9876 ± 0.0202	0.9948	0.9771	0.9875	0.9998 ± 0.0007
Random Forest	0.9935 ± 0.0110	0.9970	0.9882	0.9934	0.9990 ± 0.0038
XGBoost	0.9934 ± 0.0107	0.9972	0.9882	0.9933	1.0000 ± 0.0001

5.3.3 Pixel-Level Classification Results Under Different Labeling and Balancing Regimes (10 classes)

This subsection reports pixel-level classification performance under three labeling strategies: (i) *crack_regular_rest*, (ii) *crack_vs_rest*, and (iii) a *multi_class* formulation. All models were evaluated using identical domain-aware LOGO cross-validation splits. For each labeling strategy, two sampling regimes were considered: a class-balanced configuration and the original naturally imbalanced distribution, resulting in six experimental configurations in total.

Performance is reported as mean ± standard deviation across folds. Reported metrics include global measures (Accuracy, Balanced Accuracy and Macro-F1), CRACK-specific metrics (Precision, Recall, F1, ROC–AUC and PR–AUC), and total runtime per experiment. The evaluated classifiers include Logistic Regression (L1), Random Forest, XGBoost, a shallow Multi-Layer Perceptron (MLP), and PLS-DA.

As with the binary results above, these fold-aggregated summaries are used descriptively; no hypothesis tests or confidence intervals for differences between labeling/balancing regimes are reported.

Balanced Training Sets

Results obtained under balanced sampling are summarized in Table 5.6. The table reports performance for both binary labeling schemes and for the multi-class configuration.

Unbalanced Training Sets

Results obtained on naturally imbalanced data are summarized in Table 5.5. The same set of models and metrics are reported for direct comparison with the balanced regime.

Table 5.5: Pixel-level classification metrics (**unbalanced** training set). Values are reported as mean ± standard deviation across folds.

Label setup	Model	Accuracy	Balanced Accuracy	Precision (Cracked)	Recall (Cracked)	Macro-F1	ROC–AUC (Cracked)	PR–AUC (Cracked)
crack_regular_rest								
	PLS-DA	0.5087 ± 0.0044	0.6879 ± 0.0239	0.8825 ± 0.1174	0.7537 ± 0.2385	0.5819 ± 0.0199	0.9977 ± 0.0049	0.8630 ± 0.1242
	Logistic Regression (L1)	0.8537 ± 0.0021	0.8683 ± 0.0075	0.9654 ± 0.0185	0.9663 ± 0.0748	0.8010 ± 0.0049	0.9993 ± 0.0021	0.9839 ± 0.0116
	Random Forest	0.9175 ± 0.0056	0.9179 ± 0.0116	0.8942 ± 0.0644	0.9394 ± 0.0701	0.8904 ± 0.0106	0.9975 ± 0.0037	0.9622 ± 0.0495
	XGBoost	0.9212 ± 0.0040	0.9162 ± 0.0094	0.9804 ± 0.0118	0.9493 ± 0.0894	0.8832 ± 0.0074	0.9992 ± 0.0017	0.9902 ± 0.0160
	MLP (Small)	0.9175 ± 0.0059	0.9166 ± 0.0122	0.9530 ± 0.0272	0.9729 ± 0.0398	0.8759 ± 0.0176	0.9994 ± 0.0017	0.9911 ± 0.0122
crack_vs_rest								
	PLS-DA	0.5120 ± 0.0047	0.6940 ± 0.0189	0.8843 ± 0.1117	0.7623 ± 0.2303	0.5893 ± 0.0164	0.9979 ± 0.0045	0.8669 ± 0.1186
	Logistic Regression (L1)	0.8574 ± 0.0022	0.8704 ± 0.0076	0.9669 ± 0.0190	0.9651 ± 0.0759	0.8049 ± 0.0050	0.9993 ± 0.0022	0.9847 ± 0.0114
	Random Forest	0.9147 ± 0.0060	0.9159 ± 0.0126	0.8871 ± 0.0701	0.9368 ± 0.0751	0.8857 ± 0.0116	0.9975 ± 0.0041	0.9610 ± 0.0535
	XGBoost	0.9200 ± 0.0043	0.9154 ± 0.0098	0.9809 ± 0.0120	0.9508 ± 0.0888	0.8825 ± 0.0078	0.9992 ± 0.0018	0.9900 ± 0.0165
	MLP (Small)	0.9163 ± 0.0062	0.9158 ± 0.0129	0.9521 ± 0.0282	0.9736 ± 0.0390	0.8741 ± 0.0188	0.9994 ± 0.0017	0.9912 ± 0.0122
multi_class								
	PLS-DA	0.9670 ± 0.0211	0.9787 ± 0.0121	0.7204 ± 0.1749	0.9927 ± 0.0127	0.9013 ± 0.0709	0.9978 ± 0.0025	0.9677 ± 0.0372
	Logistic Regression (L1)	0.9972 ± 0.0031	0.9959 ± 0.0097	0.9675 ± 0.0225	0.9977 ± 0.0078	0.9920 ± 0.0085	0.9996 ± 0.0016	0.9971 ± 0.0079
	Random Forest	0.9965 ± 0.0030	0.9940 ± 0.0120	0.9675 ± 0.0234	0.9969 ± 0.0090	0.9906 ± 0.0100	0.9994 ± 0.0026	0.9970 ± 0.0077
	XGBoost	0.9978 ± 0.0021	0.9946 ± 0.0103	0.9812 ± 0.0149	0.9908 ± 0.0206	0.9923 ± 0.0074	0.9995 ± 0.0021	0.9977 ± 0.0069
	MLP (Small)	0.9905 ± 0.0249	0.9890 ± 0.0224	0.9244 ± 0.1648	0.9866 ± 0.0259	0.9699 ± 0.0704	0.9965 ± 0.0083	0.9898 ± 0.0247

Table 5.6: Pixel-level classification metrics (**balanced** training set). Values are reported as mean ± standard deviation across folds.

Label setup	Model	Accuracy	Balanced Accuracy	Precision (Cracked)	Recall (Cracked)	Macro-F1	ROC–AUC (Cracked)	PR–AUC (Cracked)
crack_regular_rest								
	PLS-DA	0.4771 ± 0.0088	0.7061 ± 0.0107	0.8433 ± 0.0910	0.9451 ± 0.1069	0.5875 ± 0.0090	0.9982 ± 0.0046	0.9500 ± 0.0899
	Logistic Regression (L1)	0.8629 ± 0.0033	0.8653 ± 0.0073	0.9865 ± 0.0067	0.9671 ± 0.0739	0.8097 ± 0.0054	0.9994 ± 0.0018	0.9874 ± 0.0090
	Random Forest	0.9277 ± 0.0046	0.9199 ± 0.0110	0.9101 ± 0.0533	0.9194 ± 0.1124	0.9047 ± 0.0087	0.9975 ± 0.0035	0.9725 ± 0.0438
	XGBoost	0.9242 ± 0.0026	0.9111 ± 0.0084	0.9932 ± 0.0042	0.9437 ± 0.0954	0.8839 ± 0.0067	0.9993 ± 0.0016	0.9919 ± 0.0175
	MLP (Small)	0.9219 ± 0.0053	0.9140 ± 0.0125	0.9831 ± 0.0123	0.9832 ± 0.0223	0.8869 ± 0.0167	0.9982 ± 0.0057	0.9934 ± 0.0097
crack_vs_rest								
	PLS-DA	0.4782 ± 0.0090	0.7078 ± 0.0106	0.8445 ± 0.0904	0.9455 ± 0.1063	0.5889 ± 0.0093	0.9982 ± 0.0046	0.9507 ± 0.0886
	Logistic Regression (L1)	0.8642 ± 0.0032	0.8662 ± 0.0074	0.9866 ± 0.0067	0.9674 ± 0.0738	0.8109 ± 0.0055	0.9994 ± 0.0018	0.9876 ± 0.0089
	Random Forest	0.9261 ± 0.0049	0.9191 ± 0.0113	0.9092 ± 0.0546	0.9192 ± 0.1128	0.9038 ± 0.0091	0.9974 ± 0.0036	0.9722 ± 0.0444
	XGBoost	0.9238 ± 0.0027	0.9110 ± 0.0085	0.9931 ± 0.0042	0.9439 ± 0.0954	0.8836 ± 0.0068	0.9993 ± 0.0016	0.9919 ± 0.0176
	MLP (Small)	0.9221 ± 0.0052	0.9143 ± 0.0126	0.9830 ± 0.0124	0.9833 ± 0.0222	0.8871 ± 0.0165	0.9982 ± 0.0057	0.9934 ± 0.0097
multi_class								
	PLS-DA	0.9666 ± 0.0210	0.9786 ± 0.0120	0.7179 ± 0.1759	0.9926 ± 0.0129	0.9010 ± 0.0707	0.9978 ± 0.0025	0.9674 ± 0.0375
	Logistic Regression (L1)	0.9973 ± 0.0031	0.9960 ± 0.0097	0.9677 ± 0.0224	0.9977 ± 0.0078	0.9921 ± 0.0085	0.9996 ± 0.0016	0.9971 ± 0.0079
	Random Forest	0.9966 ± 0.0030	0.9941 ± 0.0120	0.9676 ± 0.0233	0.9969 ± 0.0090	0.9907 ± 0.0100	0.9994 ± 0.0026	0.9970 ± 0.0077
	XGBoost	0.9979 ± 0.0021	0.9947 ± 0.0103	0.9813 ± 0.0149	0.9908 ± 0.0206	0.9924 ± 0.0074	0.9995 ± 0.0021	0.9977 ± 0.0069
	MLP (Small)	0.9906 ± 0.0249	0.9891 ± 0.0224	0.9246 ± 0.1647	0.9866 ± 0.0259	0.9700 ± 0.0704	0.9965 ± 0.0083	0.9898 ± 0.0247

The supervised pixel-level results above (Tables 5.3 and 5.4, and the broader regimes in Tables 5.5 and 5.6) summarize discriminative performance when labeled training data are available. To complement this setting, the next subsection evaluates reconstruction-based anomaly detection with autoencoders, where crack detection is driven by reconstruction error rather than a direct discriminative classifier. Quantitative results for these anomaly-detection variants are summarized in Tables 5.7–5.12.

5.3.4 Autoencoder-Based Pixel-Level Anomaly Detection

In addition to supervised classifiers, pixel-level crack detection was evaluated using reconstruction-based anomaly detection with autoencoders. The experiments were designed in a progressive manner. First, a binary formulation was considered, in which the autoencoder was trained exclusively on healthy (non-cracked) pixels and evaluated against cracked tissue. Subsequently, the setting was extended to a multi-class environment, in which background and nuisance categories (e.g., leaves, branches, plastic and calibration targets) were explicitly included during testing.

Within the multi-class regime, two complementary training strategies were investigated. In the first, the autoencoder was trained solely on pixels belonging to the *Cracked* class, such that crack signatures define the reconstruction manifold and all remaining classes are treated as anomalous. In the second strategy, the model was trained on all semantic classes except *Cracked*, thereby enforcing accurate reconstruction of diverse non-crack appearances while promoting elevated reconstruction errors for crack pixels at inference time.

Across all configurations, three fully-connected architectures were examined: *Autoencoder (64–32–16)*, *Autoencoder (128–64–32)*, and *Autoencoder (64–32–8)*. All models were trained and evaluated using identical domain-aware LOGO cross-validation splits employed in the supervised experiments.

Anomaly scores were computed from reconstruction errors and converted into binary class labels using a percentile-based threshold estimated on the training folds. Performance is reported as mean ± standard deviation across folds. Reported metrics include overall Accuracy together with class-conditional metrics (Precision, Recall, F1, ROC–AUC and PR–AUC) for the *Cracked* class (positive class), alongside aggregate confusion counts across folds and computational cost indicators. For each autoencoder formulation, two sampling regimes were considered: the original naturally imbalanced distribution and a class-balanced configuration. For a compact summary of the evaluation units and split strategies used across all experiments (including the LOGO variants used here), see Table 4.8.

Table 5.8 summarizes the balanced-sampling performance of the one-class autoencoder trained on non-cracked samples; the key takeaway is that anomaly detection can separate

cracked pixels in this controlled pixel-level setting, but these results should be interpreted as complementary to (not a replacement for) the supervised whole-image pipeline evaluated under field conditions.

Table 5.7: Pixel-level anomaly detection performance using autoencoders trained on non-cracked samples (unbalanced sampling). Values are reported as mean ± standard deviation across folds. Accuracy is reported overall, while Precision/Recall/F1/ROC–AUC/PR–AUC correspond to the *Cracked* class (positive class).

Architecture	Accuracy	Precision (Cracked)	Recall (Cracked)	F1 (Cracked)	ROC–AUC (Cracked)	PR–AUC (Cracked)	Train Time [s]	Infer Time [s]
Autoencoder (64–32–16)	0.8969 ± 0.1646	0.8226 ± 0.1925	0.9971 ± 0.0016	0.9017 ± 0.1047	0.9814 ± 0.0327	0.9554 ± 0.0900	63.34 ± 2.80	0.043 ± 0.004
Autoencoder (128–64–32)	0.8597 ± 0.1813	0.7544 ± 0.2308	0.9974 ± 0.0015	0.8628 ± 0.1270	0.9673 ± 0.0469	0.9253 ± 0.1190	60.90 ± 1.48	0.057 ± 0.001
Autoencoder (64–32–8)	0.8923 ± 0.1648	0.8126 ± 0.1938	0.9978 ± 0.0013	0.8965 ± 0.1050	0.9799 ± 0.0334	0.9511 ± 0.0913	61.02 ± 1.46	0.041 ± 0.001

Table 5.8: Pixel-level anomaly detection performance using autoencoders trained on non-cracked samples (balanced sampling). Values are reported as mean ± standard deviation across folds. Accuracy is reported overall, while Precision/Recall/F1/ROC–AUC/PR–AUC correspond to the *Cracked* class (positive class).

Architecture	Accuracy	Precision (Cracked)	Recall (Cracked)	F1 (Cracked)	ROC–AUC (Cracked)	PR–AUC (Cracked)	Train Time [s]	Infer Time [s]
Autoencoder (64–32–16)	0.9343 ± 0.0989	0.9122 ± 0.1348	0.9906 ± 0.0340	0.9437 ± 0.0820	0.9823 ± 0.0457	0.9702 ± 0.0592	65.35 ± 1.90	0.008 ± 0.002
Autoencoder (128–64–32)	0.9083 ± 0.1332	0.8771 ± 0.1576	0.9982 ± 0.0058	0.9256 ± 0.1016	0.9919 ± 0.0178	0.9833 ± 0.0357	58.49 ± 3.87	0.007 ± 0.001
Autoencoder (64–32–8)	0.9353 ± 0.1027	0.9074 ± 0.1338	0.9977 ± 0.0100	0.9449 ± 0.0833	0.9858 ± 0.0344	0.9757 ± 0.0501	52.04 ± 2.44	0.006 ± 0.002

Tables 5.9 and 5.10 report the crack-only training variant; the key takeaway is that when the "normal" class is restricted to cracked spectra, reconstruction error becomes a strong discriminator against all other semantic classes.

Table 5.9: Pixel-level anomaly detection performance using autoencoders trained exclusively on *Cracked* pixels and evaluated in a multi-class setting (unbalanced sampling). Values are reported as mean across LOGO folds. Accuracy is reported overall, while Precision/Recall/F1/ROC–AUC/PR–AUC correspond to the *Cracked* class (positive class).

Architecture	Accuracy	Precision (Cracked)	Recall (Cracked)	F1 (Cracked)	ROC–AUC (Cracked)	PR–AUC (Cracked)	Train Time [s]	Infer Time [s]
Autoencoder (64–32–16)	0.9660	0.9995	0.9662	0.9826	0.9858	0.9999	26.96	0.148
Autoencoder (128–64–32)	0.9861	0.9991	0.9869	0.9930	0.9846	0.9999	27.12	0.207
Autoencoder (64–32–8)	0.9629	0.9994	0.9632	0.9809	0.9834	0.9999	26.20	0.155

Table 5.10: Pixel-level anomaly detection performance using autoencoders trained exclusively on *Cracked* pixels and evaluated in a multi-class setting (balanced sampling). Values are reported as mean ± standard deviation across LOGO folds. Accuracy is reported overall, while Precision/Recall/F1/ROC–AUC/PR–AUC correspond to the *Cracked* class (positive class).

Architecture	Accuracy	Precision (Cracked)	Recall (Cracked)	F1 (Cracked)	ROC–AUC (Cracked)	PR–AUC (Cracked)	Train Time [s]	Infer Time [s]
Autoencoder (64–32–16)	0.9660 ± 0.0106	0.9995 ± 0.0008	0.9662 ± 0.0108	0.9826 ± 0.0055	0.9858 ± 0.0281	0.9999 ± 0.0001	61.06 ± 7.56	0.045 ± 0.013
Autoencoder (128–64–32)	0.9861 ± 0.0052	0.9991 ± 0.0017	0.9869 ± 0.0051	0.9930 ± 0.0027	0.9846 ± 0.0274	0.9999 ± 0.0001	63.03 ± 8.09	0.056 ± 0.004
Autoencoder (64–32–8)	0.9629 ± 0.0149	0.9994 ± 0.0011	0.9632 ± 0.0150	0.9809 ± 0.0079	0.9834 ± 0.0298	0.9999 ± 0.0002	59.80 ± 8.55	0.041 ± 0.003

Table 5.11 captures the failure mode of the non-crack-trained autoencoder in the multi-class setting: despite high overall accuracy, cracked-class recall and PR–AUC collapse, indicating that "normal" is too heterogeneous for reconstruction-error thresholding to reliably isolate cracks.

Table 5.11: Pixel-level anomaly detection performance using autoencoders trained on all semantic classes except *Cracked* and evaluated in a multi-class setting (unbalanced sampling). Values are reported for the held-out test split. Accuracy is reported overall, while Precision/Recall/F1/ROC–AUC/PR–AUC correspond to the *Cracked* class (positive class).

Architecture	Accuracy	Precision (Cracked)	Recall (Cracked)	F1 (Cracked)	ROC–AUC (Cracked)	PR–AUC (Cracked)	Train Time [s]	Infer Time [s]
Autoencoder (64–32–16)	0.9969	0.0096	0.1110	0.0177	0.4575	0.0083	1429.22	0.388
Autoencoder (128–64–32)	0.9986	0.0118	0.0126	0.0122	0.4513	0.0084	999.73	0.255
Autoencoder (64–32–8)	0.9984	0.0207	0.0316	0.0250	0.4542	0.0110	916.85	0.141

Table 5.12: Pixel-level anomaly detection performance using autoencoders trained on all semantic classes except *Cracked* and evaluated in a multi-class setting (balanced sampling). Values are reported for the held-out test split. Accuracy is reported overall, while Precision/Recall/F1/ROC–AUC/PR–AUC correspond to the *Cracked* class (positive class).

Architecture	Accuracy	Precision (Cracked)	Recall (Cracked)	F1 (Cracked)	ROC–AUC (Cracked)	PR–AUC (Cracked)	Train Time [s]	Infer Time [s]
Autoencoder (64–32–16)	0.9791	0.0000	0.0000	0.0000	0.2472	0.0083	2567.17	0.381
Autoencoder (128–64–32)	0.9789	0.0000	0.0000	0.0000	0.2847	0.0084	2260.73	0.299
Autoencoder (64–32–8)	0.9781	0.0000	0.0000	0.0000	0.4513	0.0110	1853.00	0.227

The pixel-level anomaly detection experiments above quantify crack separability using reconstruction-error scores across several training formulations and sampling regimes (Tables 5.7–5.12). Since the deployment objective is detection at the grape-cluster level, the following subsection evaluates an end-to-end full-image inference pipeline that aggregates pixel-level outputs into patch- and image-level decisions. Dataset composition is reported in Table 5.13, and early/late full-image performance is summarized in Table 5.14.

5.3.5 Full-Image Inference: Early vs. Late Acquisition-Stage Experiments

To evaluate robustness across acquisition stages, two independent optimization and evaluation scenarios were considered, corresponding to *early-stage* (initial onset / minimal cracking) and *late-stage* (advanced, macroscopically visible cracking) acquisition subsets. In both cases, post-processing and aggregation parameters were optimized on a calibration split using Optuna and subsequently assessed on an unseen test set. For a compact summary of the evaluation units and split strategies used across all experiments (including the Row 1 calibration vs. Row 2 held-out test setup), see Table 4.8. The corresponding calibration-to-test performance gaps are quantified later in Table 5.18.

Each experiment employed identical inference logic, including pixel-level probability thresholding, morphological filtering, patch-level aggregation and global crack-percentage criteria. In addition to the supervised pixel-level classifier, the same full-image pipeline was evaluated using an autoencoder-based anomaly detector (architecture 128–64–32, trained exclusively on *Cracked* pixels). For the autoencoder, reconstruction errors (MSE) were converted to pseudo-probabilities using an exponential decay mapping, $p_{\text{CRACK}}(x) = \exp(-e(x)/\tau)$, where τ is the stored training-derived threshold, after which the identical post-processing and aggregation logic was applied. Performance was quantified on both calibration and test splits using a comprehensive set of metrics. For system-level detection, the main performance indicator is **F1 (Cracked)**, supported by **Precision (Cracked)**, **Recall (Cracked)**, and **MCC**; accuracy is reported for completeness. Additional measures (F2, specificity, NPV) and the underlying confusion matrices are included to characterize error trade-offs.

The dataset composition for the two acquisition scenarios is reported in Table 5.13. Quantitative detection performance is summarized in Table 5.14, enabling a direct comparison between early- and late-stage conditions and between calibration and test generalization behavior.

Table 5.13: Dataset composition for full-image crack-detection experiments under early- and late-stage acquisition conditions (initial/minimal vs. advanced cracking). Row 1 was used for calibration, while Row 2 served as an independent test set.

Row	Stage	Split	Total	Unique	Pos	Neg
Row 1	Early	Calibration	172	60	32	140
Row 1	Late	Calibration	160	60	35	125
Row 2	Early	Test	60	60	32	28
Row 2	Late	Test	60	60	34	26

Table 5.14: Full-image crack detection performance for early- and late-stage acquisition experiments (initial/minimal vs. advanced cracking). Metrics are reported separately for calibration and test splits. Confusion-matrix entries correspond to the number of grape clusters classified as cracked or healthy. The main performance indicator is **F1 (Cracked)**. Accuracy, Balanced Accuracy and MCC are reported overall. Precision/Recall/F1/F2 refer to the *Cracked* class (positive class), while Specificity and NPV refer to the *Healthy* class (negative class).

Stage	Split	TP	FP	TN	FN	Acc	Balanced Accuracy	Precision (Cracked)	Recall (Cracked)	F1 (Cracked)	F2 (Cracked)	Specificity (Healthy)	NPV (Healthy)	MCC
Late	Calibration	34	5	120	1	0.963	0.966	0.872	0.971	0.919	0.950	0.960	0.992	0.897
Late	Test	27	5	21	7	0.800	0.801	0.844	0.794	0.818	0.804	0.808	0.750	0.598
Early	Calibration	23	6	134	9	0.913	0.838	0.793	0.719	0.754	0.732	0.957	0.937	0.703
Early	Test	19	3	25	13	0.733	0.743	0.864	0.594	0.704	0.633	0.893	0.658	0.504

Table 5.15: Full-image crack detection using autoencoder-based anomaly detection (128–64–32, trained on *Cracked* pixels). Reconstruction errors (MSE) were converted to pseudo-probabilities via exponential decay, $p_{\mathrm{CRACK}}(x) = \exp(-e(x)/\tau)$; the same post-processing pipeline (thresholding, morphological filtering, patch-based aggregation) was applied. Metrics are reported for calibration and test splits under early- and late-stage conditions. The main performance indicator is **F1 (Cracked)**. Accuracy, Balanced Accuracy and MCC are reported overall. Precision/Recall/F1/F2 refer to the *Cracked* class (positive class), while Specificity and NPV refer to the *Healthy* class (negative class).

Stage	Split	TP	FP	TN	FN	Acc	Balanced Accuracy	Precision (Cracked)	Recall (Cracked)	F1 (Cracked)	F2 (Cracked)	Specificity (Healthy)	NPV (Healthy)	MCC
Late	Calibration	26	7	118	9	0.900	0.843	0.788	0.743	0.765	0.751	0.944	0.929	0.702
Late	Test	22	7	19	12	0.683	0.689	0.759	0.647	0.698	0.667	0.731	0.613	0.375
Early	Calibration	19	17	123	13	0.826	0.736	0.528	0.594	0.559	0.579	0.879	0.904	0.452
Early	Test	13	13	15	19	0.467	0.471	0.500	0.406	0.448	0.422	0.536	0.441	−0.058

Full-image results in Table 5.14 quantify system-level detection performance under early- and late-stage conditions using a fixed post-processing and aggregation pipeline, and Table 5.15 reports the analogous evaluation when driven by autoencoder-based scores. The next experiment investigates the effect of spectral dimensionality reduction on this same end-to-end pipeline by applying Backward Feature Selection (BFS) and tracking CRACK metrics as a function of the number of retained wavelengths. The resulting performance trajectories are shown in Figures 5.4 and 5.5.

5.3.6 Wavelength selection (BFS) setup

Backward Feature Selection (BFS) was applied to the hyperspectral channels to evaluate full-image crack-detection performance as a function of the number of selected wavelengths. At each BFS step, the pipeline performance was recorded using CRACK-class metrics, with **CRACK PR–AUC** treated as the primary objective (Section 4.2.5). The **full-spectrum baseline** corresponds to **159 wavelengths** (450–925 nm) and serves as the reference point for the performance curves and for the subset comparisons reported below.

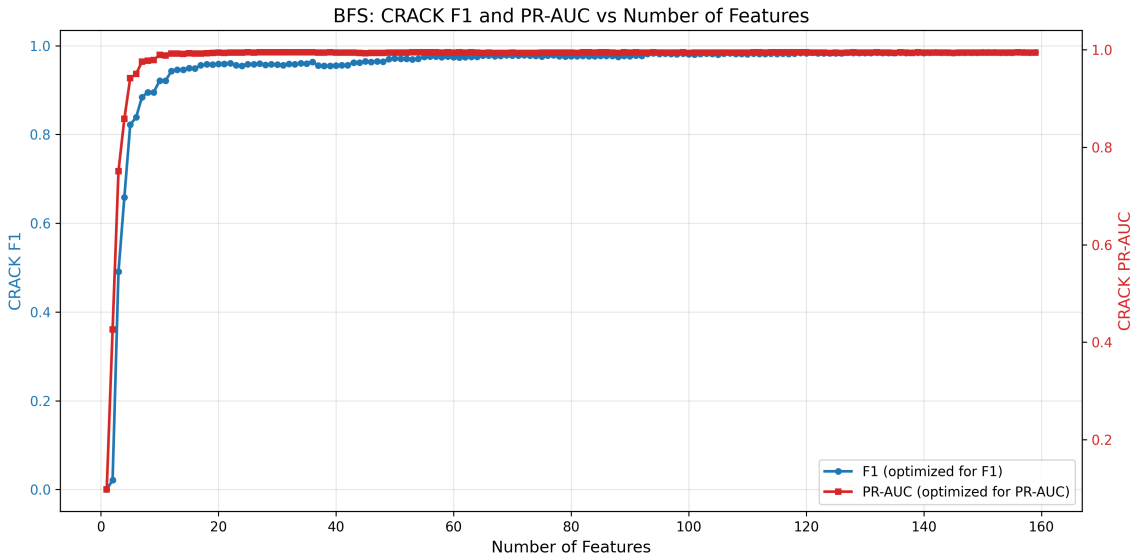

Figure 5.4: Backward Feature Selection (BFS) trajectories for the full-image pipeline, plotted as CRACK-class PR–AUC (primary objective) and CRACK-class F1 versus the number of retained wavelengths (n, unitless count; full baseline n=159 over 450–925 nm). Y-axis metrics are unitless in $[0, 1]$. Takeaway: PR–AUC exhibits a broad near-optimal plateau, motivating reduced-band configurations.

Subset selection criteria. Representative subset sizes were selected directly from the BFS performance trajectories using the same threshold-marker convention shown in Figure 5.5 and summarized in Table 5.16. Unless stated otherwise, subset choice is based on the **CRACK PR–AUC** curve (Figure 5.5b), while CRACK F1 (Figure 5.5a) is

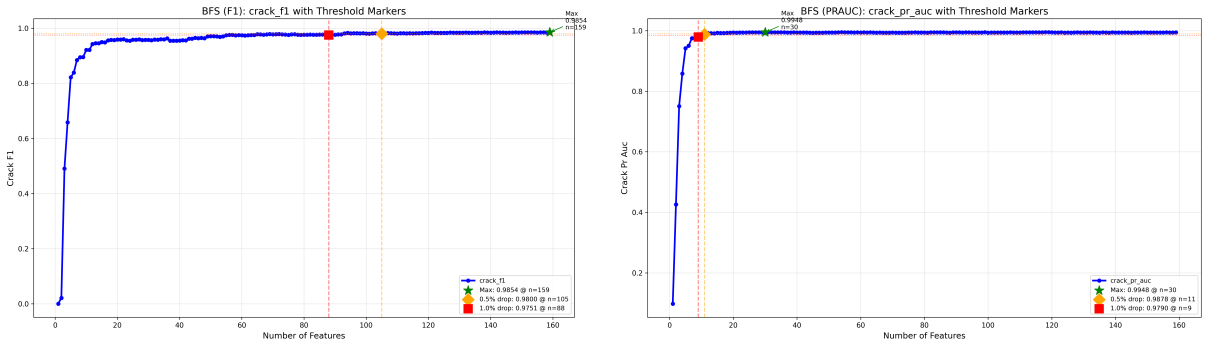

(a) CRACK-class F1 vs. number of wavelengths (n), with markers at the maximum and at 0.5%/1.0% drop points.

(b) CRACK-class PR–AUC (primary BFS objective) vs. number of wavelengths (n), with the same threshold markers.

Figure 5.5: BFS threshold-marker visualization on CRACK metrics, used to define representative reduced-band subset sizes. Markers indicate the maximum and the first n where performance falls more than 0.5% and 1.0% below that maximum (unitless drop). Takeaway: these markers operationalize "top-n" selection without introducing an arbitrary n.

Table 5.16: Summary of BFS wavelength-count thresholds for CRACK metrics.

Metric	Max score	$n_{\max}$	0.5% drop: n	score	1.0% drop: n	score
CRACK PR–AUC	0.9948	30	11	0.9878	9	0.9790
CRACK F1	0.9854	159	105	0.9800	88	0.9751

plotted as a complementary, threshold-dependent operating-point summary. Specifically, the **top-30** subset corresponds to the wavelength count $n_{\max}$ that maximizes CRACK PR–AUC (here $n_{\max}$=30), and the **top-11** subset corresponds to the first wavelength count encountered when reducing features for which CRACK PR–AUC drops by more than 0.5% from its maximum (i.e., falls below $0.995 \times \text{PR–AUC}_{\max}$; here n=11). For reference, the analogous 1.0% drop threshold on CRACK PR–AUC corresponds to n=9 and is included as a more aggressive reduced-band setting in the end-to-end full-image evaluation (Table 5.17).

5.3.7 Full-image wavelength-selection results

Full-image crack-detection experiments were conducted for several wavelength subsets after complete spatial post-processing, including probability thresholding, morphological filtering, and blob-based aggregation. Performance was evaluated separately for early- and late-stage acquisitions on an independent test set.

Table 5.17 reports the obtained CRACK-class metrics for representative wavelength counts.

Table 5.17: Full-image crack-detection performance for different wavelength subsets under early- and late-stage conditions.

Stage	# Wavelengths	Accuracy	Balanced Accuracy	Precision (Cracked)	Recall (Cracked)	F
Early	9	0.7833	0.7902	0.8800	0.6875	
Late	9	0.8000	0.8054	0.8667	0.7647	
Early	11	0.7500	0.7567	0.8400	0.6562	
Late	11	0.8167	0.8111	0.8286	0.8529	
Early	30	**0.8167**	**0.8214**	**0.8889**	**0.7500**	
Late	30	**0.8333**	**0.8348**	**0.8750**	0.8235	
Early	159	0.8000	0.8036	0.8571	**0.7500**	
Late	159	**0.8333**	0.8258	0.8333	**0.8824**	

Table 5.18: Model Generalization Analysis: Comparison between Calibration and Test MCC.

Stage	# Features	MCC Calibration	MCC Test	**Gap (Δ)**
Early	9	0.7381	0.5873	0.1508
	30	0.7232	**0.6447**	**0.0785**
	159	0.6631	0.6071	0.0560
Late	9	0.8968	0.6054	0.2914
	30	0.8771	**0.6652**	**0.2119**
	159	0.8931	0.6591	0.2340

Calibration-to-test generalization gap (primary result). A consistent calibration-to-test generalization gap is observed across all evaluated wavelength subset sizes and in both acquisition-stage conditions. As summarized in Table 5.18, early-stage calibration MCC spans 0.663–0.738, while early-stage test MCC spans 0.587–0.645, corresponding to gaps of 0.056–0.151. For the late-stage scenario, calibration MCC spans 0.877–0.897, while test MCC spans 0.605–0.665, yielding larger gaps of 0.212–0.291. This indicates that performance on the calibration row (Row 1) can materially overestimate performance on the independent test row (Row 2), and that reduced-band conclusions should be anchored primarily in the held-out test results rather than calibration scores alone.

Note on uncertainty. Table 5.17 (and the generalization gaps in Table 5.18) report point estimates on the held-out test set. Where the narrative compares the full-spectrum baseline (159 wavelengths) to reduced-band subsets (e.g., 30 or 9 wavelengths), the strength of these comparisons would be improved by confidence intervals for the metric *differences*. A statistically appropriate approach would be a cluster-aware bootstrap over independent units (e.g., image/cluster-level samples), or a paired resampling procedure if per-sample outputs are retained. Such uncertainty quantification is not included here because the exported summary results provide aggregate scores without per-unit identifiers, preventing a reliable post-hoc resampling analysis.

The wavelength-selection results above provide end-to-end test-set performance at representative subset sizes (Table 5.17) and summarize calibration-to-test generalization gaps (Table 5.18), complementing the full BFS performance curves in Figure 5.4. To assess whether these outcomes are robust to random variation in the data partitioning and model initialization, the following stability analysis repeats the BFS elimination sequence under multiple seeds. Per-seed results are summarized in Table 5.19.

5.3.8 BFS Wavelength-Selection Stability Analysis

To assess the robustness of the Backward Feature Selection (BFS) procedure, the full elimination sequence was repeated five times using different random seeds. In each run, both the train/validation data split seed and the XGBoost model seed were set to the same value (seeds 1–5), so that every repetition uses a different data partition *and* a different model initialisation. The objective metric was CRACK PR–AUC, and elimination proceeded from 159 down to 1 wavelength. For each repetition, the top-30 and top-11 surviving wavelengths were recorded. Here, "top-30" denotes the PR–AUC-maximizing point ($n_{\max}$=30), while "top-11" denotes the 0.5% PR–AUC drop threshold (Table 5.16; Figure 5.5).

Table 5.19 summarises the per-seed results. Best PR–AUC ranged from 0.812 to 0.998, and the optimal number of features varied between 64 and 153, revealing substantial sensitivity to the data partition.

Table 5.19: BFS stability: per-seed results under varying train/test splits.

Seed	Split seed	Model seed	Best PR–AUC (Cracked)	Best n (wavelengths)
1	1	1	0.9014	153
2	2	2	0.9933	66
3	3	3	0.8714	111
4	4	4	0.9979	64
5	5	5	0.8119	149
Mean ± Std			0.915 ± 0.077	108.6 ± 42.2

Wavelength Overlap Across Seeds

Tables 5.20 and 5.21 report the pairwise Jaccard similarity between the wavelength subsets selected by each seed for the top-30 and top-11 configurations, respectively.

Table 5.20: Pairwise Jaccard similarity of top-30 wavelengths across seeds (varying split). Mean Jaccard = 0.493.

	Seed 1	Seed 2	Seed 3	Seed 4	Seed 5
Seed 1	—	0.409	0.590	0.722	0.442
Seed 2	0.409	—	0.378	0.409	0.476
Seed 3	0.590	0.378	—	0.590	0.442
Seed 4	0.722	0.409	0.590	—	0.476
Seed 5	0.442	0.476	0.442	0.476	—

Table 5.21: Pairwise Jaccard similarity of top-11 wavelengths across seeds (varying split). Mean Jaccard = 0.398.

	Seed 1	Seed 2	Seed 3	Seed 4	Seed 5
Seed 1	—	0.500	0.412	0.333	0.412
Seed 2	0.500	—	0.412	0.412	0.333
Seed 3	0.412	0.412	—	0.500	0.333
Seed 4	0.333	0.412	0.500	—	0.333
Seed 5	0.412	0.333	0.333	0.333	—

The top-30 subsets share 13 wavelengths across all five seeds (42%), with a mean Jaccard of 0.493.

The top-11 subsets share 4 wavelengths across all five seeds (33%), with a mean Jaccard of 0.398. Based on the per-seed wavelength export files (experiments/feature_selection/stability_bfs_prauc/varyingsplit/*/selected_wavelengths_at11.csv), the cross-seed intersection at this setting comprises exactly four wavelengths (reported to two decimal places as stored in the exports): (452.25, 548.55, 580.90, and 729.53) nm. These same four wavelengths also appear in the 13-wavelength intersection of the top-30 subsets (val-

idated from the corresponding `selected_wavelengths_at30.csv` files), indicating that they are consistently selected under both subset sizes.

Wavelength Popularity and Stability – Top 30

Figures 5.6–5.9 visualise the selection frequency and stability of the top-30 wavelength subsets across the five seeds. Figure 5.7 further shows that the same dominant regions persist under coarser binning, indicating that the stability conclusions are not an artefact of plotting resolution.

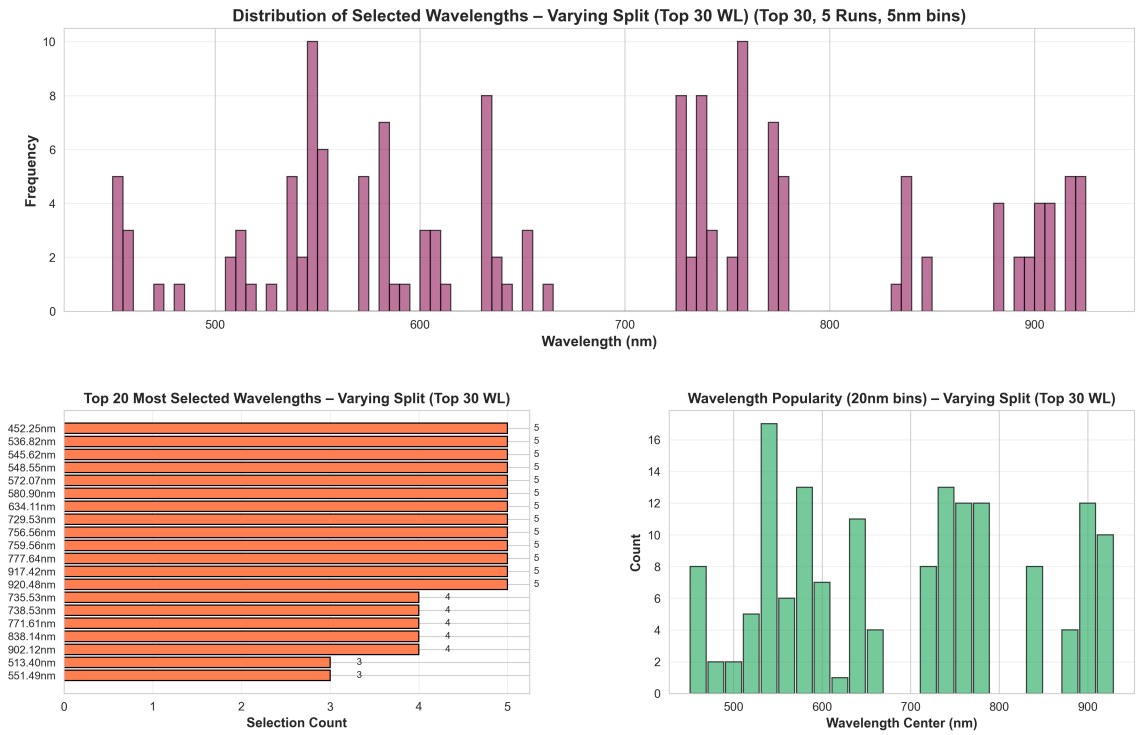

Figure 5.6: Distribution and popularity of the top-30 selected wavelengths across five varying-split seeds.

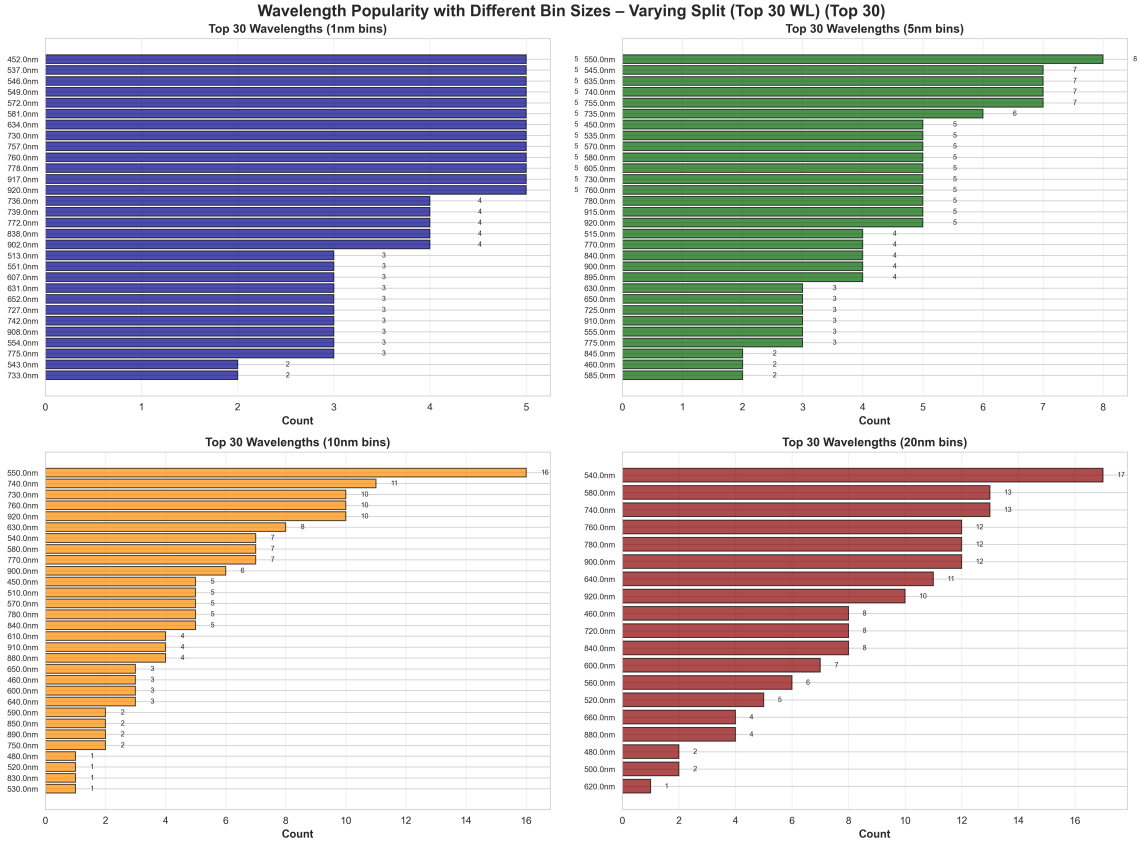

Figure 5.7: Wavelength popularity at different bin sizes (1, 5, 10, 20 nm) for the top-30 subsets.

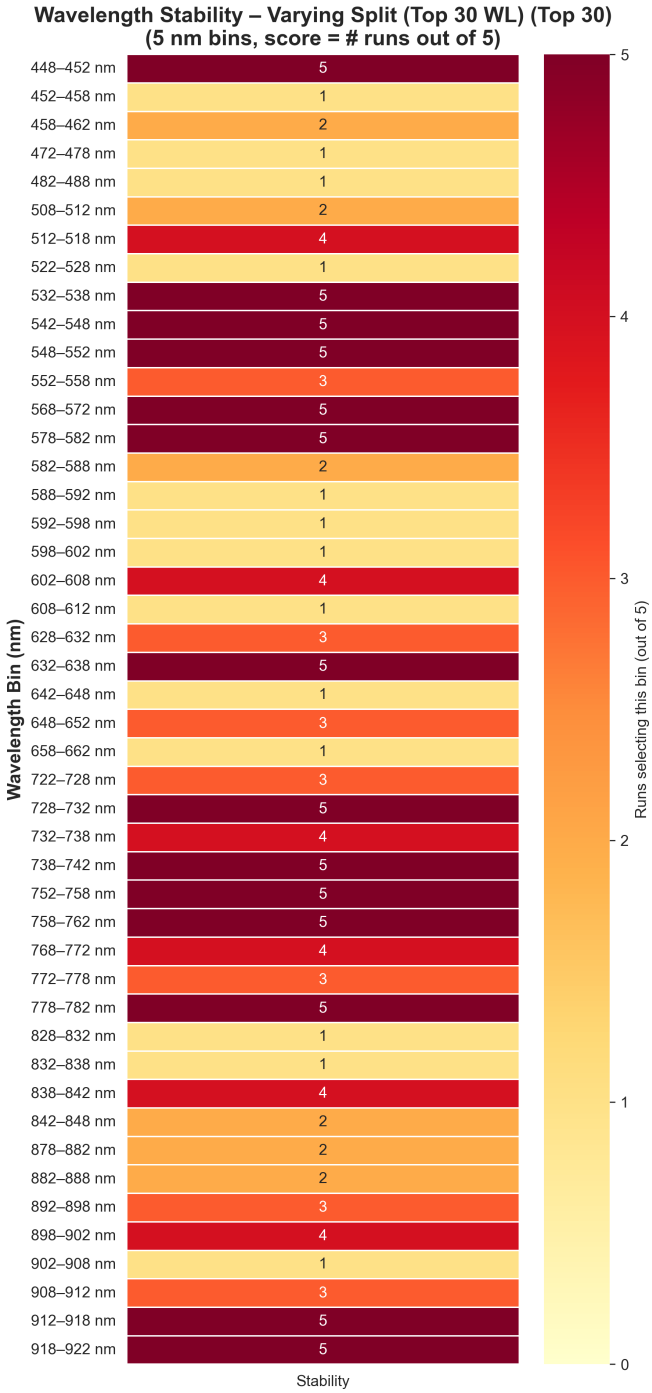

Figure 5.8: Stability heatmap for the top-30 BFS subsets across five varying-split seeds (objective: CRACK PR–AUC). The x-axis is wavelength binned at 5 nm; each cell value (0–5) indicates how many seeds selected at least one wavelength within that bin (unitless count). Takeaway: selection concentrates in a limited set of repeatable spectral regions, but exact channel identities vary across splits.

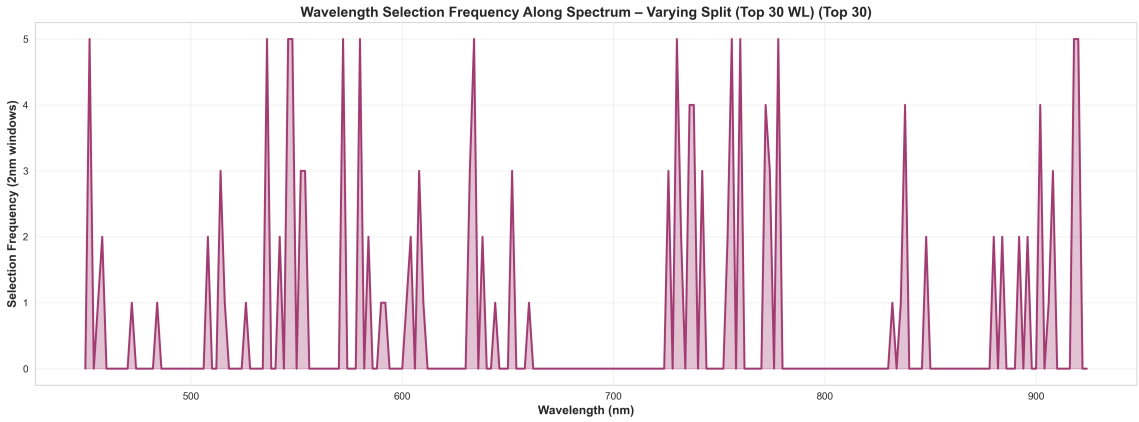

Figure 5.9: Wavelength selection frequency along the spectrum (2 nm sliding window) for the top-30 subsets.

Wavelength Popularity and Stability – Top 11

The same analysis was repeated for the top-11 wavelength subsets (Figures 5.10–5.13), corresponding to the most aggressive dimensionality reduction evaluated (within 1% of the maximum PR–AUC).

For interpretability, Figure 5.11 shows how apparent wavelength "popularity" changes with bin size, while Figure 5.12 highlights which 5 nm bins are consistently selected across seeds; the key takeaway is that only a small core set remains stable under this aggressive reduction.

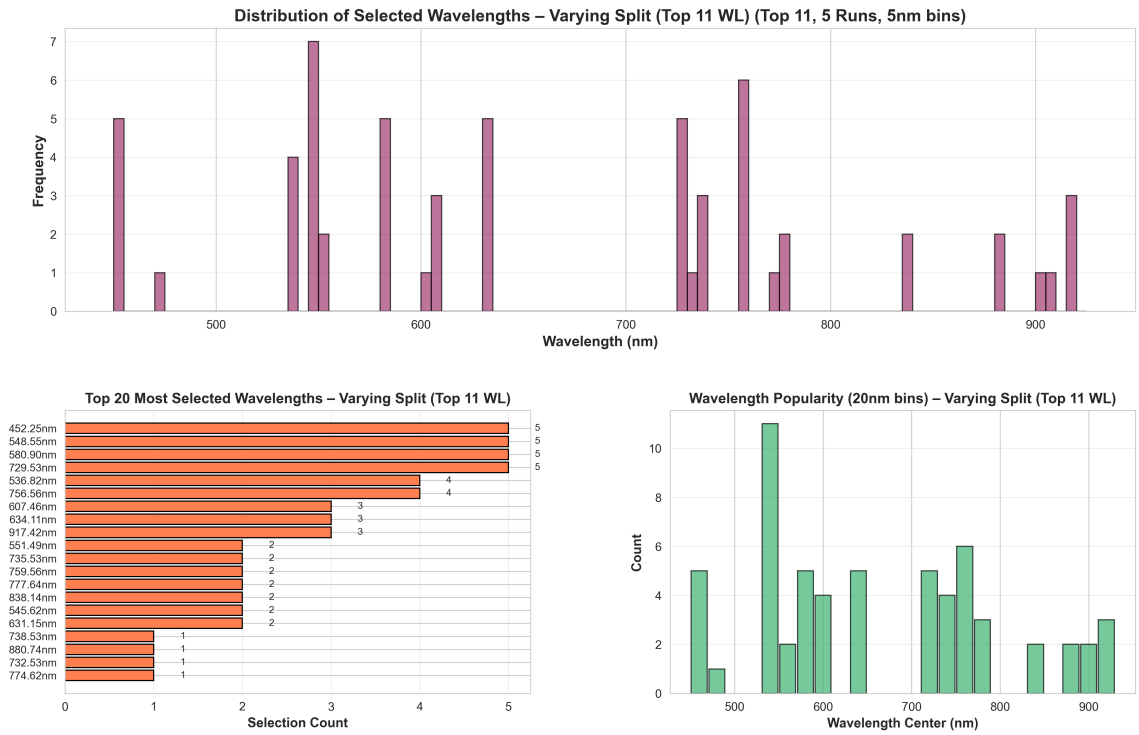

Figure 5.10: Distribution and popularity of the top-11 selected wavelengths across five varying-split seeds.

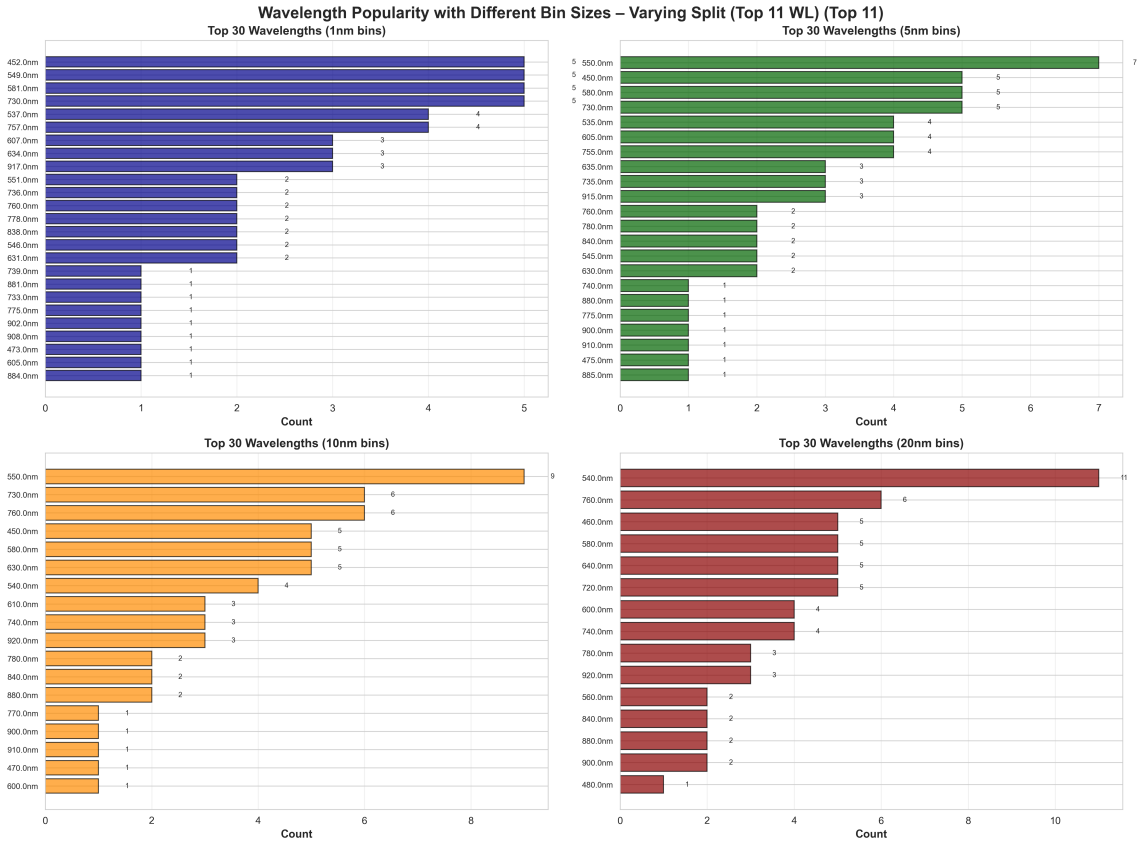

Figure 5.11: Wavelength popularity at different bin sizes (1, 5, 10, 20 nm) for the top-11 subsets.

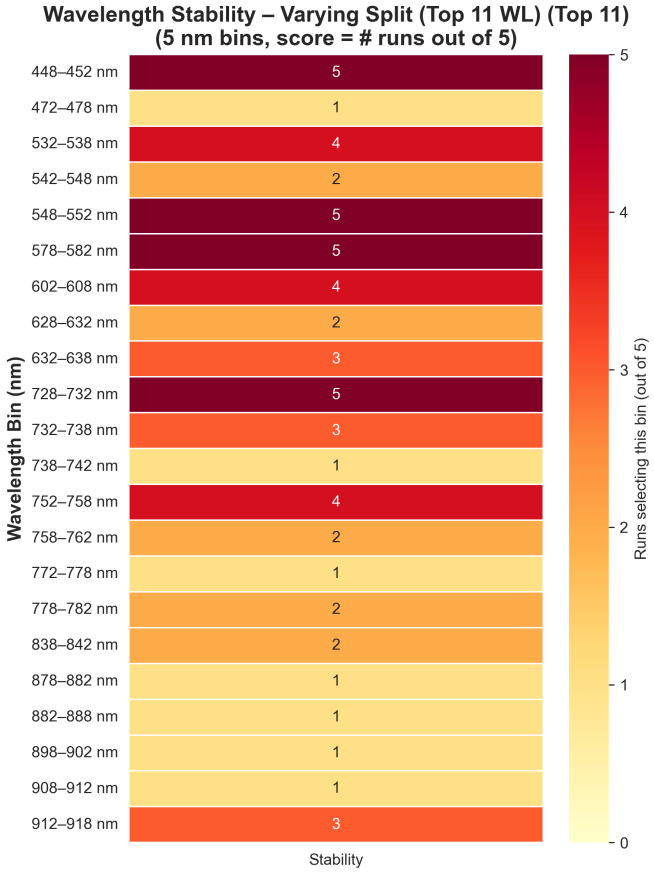

Figure 5.12: Stability heatmap for the top-11 BFS subsets across five varying-split seeds (objective: CRACK PR–AUC; 0.5% drop setting). The x-axis is wavelength binned at 5 nm; each cell value (0–5) indicates how many seeds selected a wavelength within that bin (unitless count). Takeaway: under aggressive reduction, only a small core of bins remains consistently selected across splits.

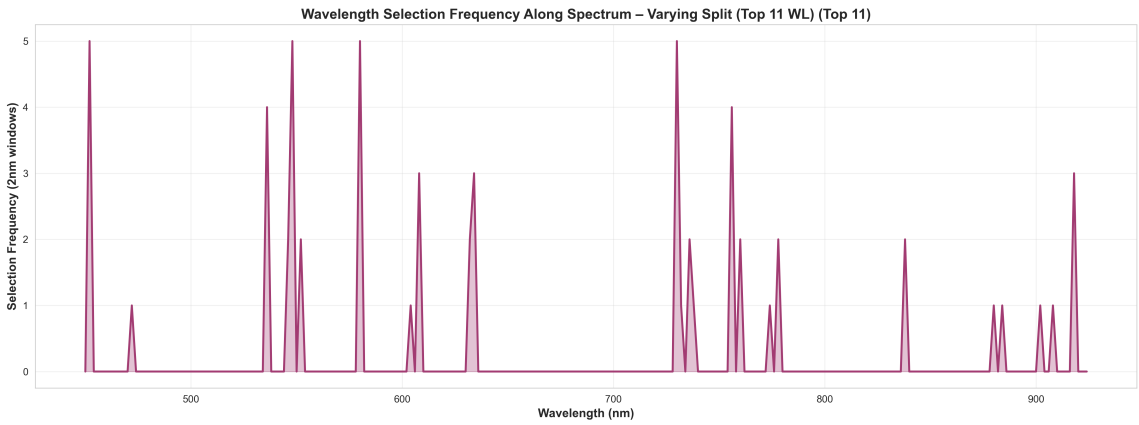

Figure 5.13: Wavelength selection frequency along the spectrum (2 nm sliding window) for the top-11 subsets.

Chapter 6

Discussion

6.1 Summary of Key Findings

This study set out to determine whether hyperspectral imaging in the visible–near-infrared (VIS–NIR) range can detect existing cracks in table grapes and, more ambitiously, identify crack-related spectral signatures even under early-stage acquisitions where macroscopic cracking is not yet clearly visible. The experimental programme yielded five principal results that, taken together, advance both the scientific understanding and the practical feasibility of spectral crack detection. In the discussion below, *detection* refers to classification at the time of measurement. Throughout, *early* and *late* denote acquisition-stage subsets relative to crack progression at the time of measurement: *early* corresponds to absent-to-minimal/incipient cracking (the first recorded small-crack stage for a given cluster identity), whereas *late* corresponds to advanced cracking that is macroscopically visible. These terms are used for stratified evaluation and are not a forecast of future cracking.

First, the spectral characterisation confirmed that healthy and cracked grape tissues produce markedly different reflectance signatures across the analyzed 450–925 nm range. Healthy tissue exhibited mean VIS reflectance of 0.218 and mean NIR reflectance of 0.660, whereas cracked tissue dropped to 0.137 and 0.450, respectively (Table 5.1). The strongest separability was concentrated in the red-edge and NIR plateau, with Cohen's d reaching 2.69 near 757 nm and a peak Fisher score of 3.63 near 748 nm (Table 5.2). This physical basis validates Hypothesis 1 and establishes that cracking alters the optical properties of berry skin in ways that are measurable with a portable hyperspectral sensor Blackburn, 2007; Y. Zhang et al., 2022.

Second, pixel-level supervised classifiers achieved near-ceiling discrimination when trained and tested on manually labelled spectra under the multi-class formulation, with XGBoost reaching ROC–AUC of 1.00 and consistently strong cracked-class separability (Tables 5.3–5.4), thereby supporting Hypothesis 2. All five classifiers—including PLS-DA,

Logistic Regression, SVM, Random Forest, and XGBoost—achieved extremely high performance under both balanced and unbalanced regimes in the multi-class setting (Tables 5.5–5.6). However, the binary and simplified labelling schemes (crack_regular_rest, crack_vs_rest) that conflate background classes with healthy tissue exhibited substantially lower balanced accuracy (approximately 87–92 %) and higher variance across LOGO folds, foreshadowing the challenges encountered at the whole-image level.

Third, the transition from pixel-level to whole-image inference revealed a meaningful performance gap. Late-stage images, in which cracks are macroscopically visible, yielded a test-set $F1_{CRACK}$ of 0.818 and an MCC of 0.598, whereas the early-stage scenario—the more practically relevant one—achieved a test $F1_{CRACK}$ of 0.704 and an MCC of 0.504 (Table 5.14). These values represent a substantial degradation relative to the pixel-level ceiling, yet they also demonstrate that the full-image pipeline retains meaningful early-stage identification value under realistic vineyard conditions, supporting Hypothesis 3 and partially supporting Hypothesis 4.

Fourth, Backward Feature Selection (BFS) showed that the 159-channel hyperspectral cube can be reduced to as few as 11 wavelengths with only 0.5 % loss in CRACK PR–AUC (from 0.9948 to 0.9878), and to 9 wavelengths within 1.0 % of the maximum (Table 5.16). Critically, the 30-wavelength subset matched or exceeded the full spectrum on the independent test set, achieving the highest early-stage test MCC of 0.6447 compared with 0.6071 for the full 159-channel cube (Table 5.17). Stability analysis across five random seeds further identified four wavelengths—452.25, 548.55, 580.90, and 729.53 nm—that were selected in every single repetition, confirming their physical importance and supporting Hypothesis 5.

Fifth, the autoencoder-based anomaly-detection branch exposed an instructive asymmetry. Training on cracked pixels alone produced competitive pixel-level performance, with a cracked-class PR–AUC of 0.9999 (accuracy 0.966–0.986; Table 5.10), whereas training on all non-crack classes failed catastrophically, with near-zero recall and F1 for the cracked class (Table 5.12). At the whole-image level, the autoencoder pipeline achieved a test MCC of only −0.058 in the early-stage scenario, compared with 0.504 for the supervised classifier (Tables 5.15 and 5.14).

The sections that follow interpret these findings in the context of grape physiology, sensor design, and operational deployment.

6.1.1 Hypotheses Evaluation

For traceability, the five research hypotheses are evaluated here against the results reported in Chapter 5.

- **Hypothesis 1 (Spectral distinguishability): Supported.** Clear and consistent separation between healthy and cracked tissue was observed in mean spectra and

separability statistics (Figure 5.1; Figure 5.2; Tables 5.1 and 5.2).

- **Hypothesis 2 (Pixel-level classification feasibility): Supported.** Supervised models achieved near-ceiling discrimination under controlled pixel-level labeling, across both balanced and unbalanced regimes (Tables 5.3–5.4 and 5.5–5.6).
- **Hypothesis 3 (Whole-image robustness): Supported.** When deployed on full hyperspectral scenes that include complex background content, the end-to-end whole-image pipeline retained meaningful precision and MCC on an independent test row (Table 5.14; with dataset composition in Table 5.13).
- **Hypothesis 4 (Early detection capability): Partially supported.** Early-stage images (acquired before clearly visible macroscopic cracking) were classified above chance on the held-out test set, but with reduced performance relative to late-stage detection and non-trivial calibration-to-test gaps (Tables 5.14 and 5.18).
- **Hypothesis 5 (Spectral efficiency): Supported.** BFS demonstrated that strong crack-detection performance can be maintained with reduced wavelength subsets (Figure 5.5; Table 5.16), and whole-image evaluation confirmed that reduced-band configurations can match or exceed the full-spectrum baseline on the independent test set (Table 5.17). Stability analysis further identified a small core of universally selected wavelengths across seeds (Figure 5.10).

6.2 Spectral and Physiological Interpretation

6.2.1 VIS Region: Pigments and Skin Integrity

The lower mean reflectance of cracked tissue across the entire VIS range (400–700 nm) likely reflects two complementary processes rooted in the biochemistry of berry skin. When the berry cuticle ruptures, the exposed sub-epidermal cells undergo rapid oxidative browning Santos et al., 2023. The resulting accumulation of phenolic oxidation products—including quinones and melanoidins—broadens the absorption across the blue-green region, depressing overall VIS reflectance. Simultaneously, the anthocyanins concentrated in the outer mesocarp—which govern the characteristic red-to-black colouration of 'Scarlotta'—become disordered once the cuticle barrier is breached Castellarin and other, 2016; the loss of the smooth wax layer eliminates the specular component of reflectance and disturbs the internal scattering geometry that normally elevates green-band reflectance relative to the absorbing flanks of the chlorophyll and anthocyanin peaks Blackburn, 2007.

The fact that the wavelength near 452 nm emerged as one of the four universally stable features (Figure 5.10) corroborates this interpretation: 452 nm falls within the Soret

absorption band of chlorophyll and at the short-wavelength edge of anthocyanin absorption Blackburn, 2007. When cracking disrupts the cuticle, enhanced oxidation and pigment leaching alter absorbance at this wavelength more consistently than at neighbouring bands, explaining why BFS repeatedly selects it regardless of the random seed.
Similarly, the stability of the 548 nm and 580 nm features aligns with the green trough and the orange shoulder of anthocyanin reflectance, respectively. These regions are sensitive to anthocyanin concentration, cell-layer organisation, and skin integrity, making them natural indicators of cuticle disruption Blackburn, 2007; Castellarin and other, 2016. Previous work on sweet cherry cracking has reported analogous green-band sensitivity, which was attributed to changes in sub-cuticular scattering following micro-fracture development Peschel and Knoche, 2005; Xu et al., 2025, supporting the generality of these spectral markers across thin-skinned fruit species. La Spada et al. La Spada et al., 2024 further showed that cuticle thickness and quality in table grapes can be modulated by preharvest treatments, reinforcing the link between cuticle integrity and optical properties that underlies the VIS-range discriminability observed here.

6.2.2 NIR and Red-Edge Sensitivity to Water Stress

The most pronounced spectral differences between healthy and cracked tissue were observed in the NIR region, where Cohen's d exceeded 2.5 near 757 nm and the mean absolute reflectance difference reached 0.370 near 727 nm (Table 5.2; Figure 5.2). This large effect size reflects the dominant role of cellular water content and tissue structure in shaping NIR reflectance Thenkarail et al., 2016; Y. Zhang et al., 2022. In intact berries, the mesocarp acts as a powerful diffuse reflector: multiple internal scattering events at air–cell-wall interfaces elevate reflectance above 700 nm, while liquid water in the symplast introduces broad absorption features centred around 760 nm and 970 nm T. Wang and Zhao, 2024. Once cracking occurs, mesocarp cells lose turgor through rapid dehydration and juice leakage, collapsing the scattering interfaces and dramatically reducing NIR reflectance Chang et al., 2019.
The red-edge—the steep rise in reflectance between 680 nm and 740 nm—is particularly informative because it is jointly governed by chlorophyll absorption (which sets the short-wavelength foot) and internal scattering (which sets the shoulder) Blackburn, 2007; Thenkarail et al., 2016. In cracked berries, both contributions are diminished: chlorophyll degrades in exposed tissue and the scattering plateau drops, causing the red-edge to shift toward shorter wavelengths and to flatten. The fourth stable wavelength at 729 nm sits precisely on this inflection, where the slope and amplitude of the red-edge are most sensitive to simultaneous changes in pigment content and tissue water (Figure 5.9). These observations align with established water-stress physiology in grape berries. Chang and Keller Chang and Keller, 2021; Chang et al., 2019 demonstrated that turgor pres-

sure dynamics and cuticle permeability modulate berry water relations during ripening, with micro-cracks forming days before macroscopic splitting. Yu et al. Yu et al., 2025 recently showed that aquaporin-mediated water uptake plays a pivotal role in grape berry cracking, with the cracking-susceptible cultivar 'Xiangfei' exhibiting significantly higher mesocarp water content than the resistant 'Zuijinxiang' during the critical cracking period. The spectral changes detected in this study—particularly the depressed NIR plateau and blue-shifted red-edge—can therefore be understood as the optical fingerprint of the biomechanical failure pathway that culminates in visible cracking. This interpretation is consistent with the broader VIS–NIR sensing literature showing that pre-symptomatic stress in plant tissue manifests as altered internal scattering and pigment absorption before macroscopic symptoms appear Abade et al., 2025; Liu et al., 2023; Mahlein, 2016.

6.3 Why Pixel-Level Detection Works in Controlled Settings but Fails in Field Conditions

The near-perfect pixel-level accuracy reported in Chapter 5 should be interpreted with caution, as it reflects favourable conditions that do not fully represent operational vineyard imaging. Under the multi-class labelling scheme, in which background categories (leaf, wood, soil, plastic) are explicitly modelled, the classifier benefits from a well-structured feature space in which each class occupies a distinct spectral region. The resulting decision boundaries are clean and generalise well across LOGO cross-validation folds drawn from different grape clusters, as evidenced by the low standard deviations across folds for XGBoost (accuracy 0.998 ± 0.002; Table 5.5).

When the same classifiers are deployed on whole-image hyperspectral scenes, however, several confounding factors degrade performance. First, the spatial resolution of the Specim IQ (approximately 1.08 mm per pixel at 1 m distance) Behmann et al., 2018 means that many image pixels are *mixed*: they straddle the boundary between berry and leaf, or between crack and intact skin. Mixed pixels produce hybrid spectral signatures that do not match any of the pure-class prototypes used during training, leading to ambiguous or erroneous class assignments Bioucas-Dias et al., 2013. Second, the illumination geometry in the field is highly variable. Although a white reference panel was included in every scene, the hemispherical reflectance from a curved berry surface differs from the Lambertian reference geometry, introducing shading gradients, bidirectional reflectance distribution function (BRDF) effects, and specular highlights that shift the apparent spectrum Mishra et al., 2017. Third, the presence of thin surface films—water droplets, dust, spray residues—modifies reflectance in ways that are unaccounted for in the pixel-level training set. These field-specific artefacts are well documented in the close-range hyperspectral literature Mishra et al., 2017; Ram et al., 2024 and explain

why laboratory-to-field performance degradation is a recurring challenge in agricultural HSI applications García-Vera et al., 2024.

The binary and simplified labelling experiments (crack_regular_rest, crack_vs_rest) anticipated this problem. Under these formulations, the classifier must separate cracked tissue from a heterogeneous "rest" category that encompasses every non-crack pixel, including spectrally diverse background materials. The resulting balanced accuracy of approximately 87–92 % (Table 5.5) still represents good performance for a purely spectral (non-spatial) model, yet the higher variance across folds and the lower precision for the cracked class signal that the decision boundary is less stable when background diversity increases. Notably, PLS-DA suffered the most under these simplified schemes, achieving balanced accuracy of only 0.688–0.706 (Table 5.5), whereas tree-based methods (Random Forest, XGBoost) maintained balanced accuracy above 0.91, suggesting that non-linear classifiers are more resilient to spectral background heterogeneity.

These observations lead to a clear methodological implication: pixel-level spectral classifiers, however accurate in controlled conditions, require an intermediate spatial processing stage—such as segmentation, morphological filtering, or patch-level aggregation—before they can be deployed reliably in uncontrolled vineyard imagery. This finding echoes the broader HSI literature, where spectral–spatial integration strategies have been shown to significantly improve classification robustness in scenes with complex backgrounds Bioucas-Dias et al., 2013; Z. Chen et al., 2024. The full-image pipeline evaluated in this study incorporated exactly such steps, and while the resulting performance did not match the pixel-level ceiling, it demonstrates a viable pathway from laboratory accuracy to field applicability.

6.4 Spatial Aggregation as a Robust Strategy for Early-Stage Crack Detection

One of the most practically significant findings of this study is that the full-image pipeline, which aggregates pixel-level classification outputs through morphological filtering and spatial thresholding, retains value even in the early-stage scenario. Early-stage images were acquired before any clearly discernible macroscopic cracking had occurred, yet the pipeline achieved a test $F1_{CRACK}$ of 0.704 (precision 0.864, recall 0.594) and an MCC of 0.504 (Table 5.14). Here, *early* denotes the acquisition stage; the model output is a single-date classification at the time of measurement (not a statement about a future cracking event). While this performance falls short of the late-stage benchmark ($F1_{CRACK}$ 0.818, MCC 0.598; recall 0.794), it demonstrates that crack-related spectral signatures are measurable before advanced macroscopic symptoms manifest.

This finding can be understood through the physiological lens developed in the pre-

ceding section. Cracking is not an instantaneous event but rather the terminal stage in a progressive sequence: beginning with cuticular micro-fracturing Chang and Keller, 2021; Peschel and Knoche, 2005, continuing through changes in water permeability and turgor dynamics Chang et al., 2019; Yu et al., 2025, and culminating in macroscopic splitting Khadivi-Khub, 2014; Santos et al., 2023. The spectral indicators of the intermediate stages should therefore be detectable before the final mechanical failure. The depressed NIR reflectance and altered red-edge slope observed in the pixel-level analysis (Figure 5.1; Table 5.1) are precisely the optical signatures of the cellular-scale changes that precede visible cracking: loss of internal turgor, reduced scattering, and incipient pigment degradation. This interpretation aligns with recent findings by Dong et al. Dong et al., 2025, who demonstrated that hyperspectral imaging can detect apple bitter pit—another turgor-related physiological disorder—before visual symptoms emerge, and with Haghbin et al. Haghbin et al., 2023, who showed pre-symptomatic detection of grey mould in kiwifruit using VIS–NIR chemometrics.

A direct, apples-to-apples numerical comparison to these prior studies is not meaningful here, because the tasks, evaluation units, and acquisition conditions differ substantially. Dong et al. Dong et al., 2025 and Haghbin et al. Haghbin et al., 2023 target different crops and disorders and typically operate on localized fruit- or leaf-level samples acquired under more controlled conditions, whereas the present work evaluates *cluster-level* decisions in preharvest vineyard scenes with complex background clutter and a spatially separated Row 1 → Row 2 test split (Table 5.13). As numerical context for the broader early-detection HSI literature (still not directly comparable), Ou et al. Ou et al., 2024 report 96.6 % accuracy for distinguishing healthy vs. 24 h gray-mold-affected strawberry leaves using a fused-feature CNN model, and Zhang et al. Y. Zhang et al., 2024 report up to 98.61 % accuracy for early pear leaf anthracnose detection using multi-source feature fusion. In this more deployment-relevant setting, the baseline early-stage full-image pipeline achieved a test MCC of 0.504 (Table 5.14), and the best reduced-band configuration reached an early-stage test MCC of 0.6447 (Table 5.17). Qualitatively, the agreement across studies is that VIS–NIR hyperspectral measurements capture measurable pre-symptomatic signatures of physiological disruption; however, the remaining performance gap relative to controlled-sample studies underscores that field-scale robustness and cross-domain generalization remain the limiting factors for operational early-warning systems.

Spatial aggregation addresses a fundamental limitation of single-pixel classification. Individual pixel classifications are inherently noisy: a single mis-classified pixel in a cluster of several thousand has negligible practical consequence, but a cluster of false positives near a berry edge can generate a spurious crack flag. By aggregating pixel-level classifications into patch-level and then image-level statistics—and by requiring that the proportion of flagged crack pixels exceeds a calibrated threshold—the pipeline effectively smooths over

pixel-level noise and yields a robust cluster-level score Bioucas-Dias et al., 2013.
The experimental design exploited this insight by using Optuna to jointly optimise the probability threshold, morphological kernel sizes, and the global crack-percentage criterion on the calibration split. The resulting pipeline achieved substantially higher precision (0.864 on the early-stage test set) than a naive pixel-level approach would, precisely because the spatial aggregation enforces spatial coherence on the classification map. That the early-stage pipeline achieved higher precision (0.864) than recall (0.594) on the test split (Table 5.14) indicates a conservative decision boundary, which is appropriate for an early-warning system where false alarms carry higher operational costs than missed detections in the initial screening pass. This paradigm—pixel-level classification followed by spatially informed aggregation—constitutes the core operational strategy recommended by this study for field deployment and aligns with the broader consensus in agricultural HSI that spatial context is critical for robust classification Z. Chen et al., 2024; Ram et al., 2024.

6.5 Feature Selection and Spectral Stability

6.5.1 Dimensionality Reduction via BFS

The BFS elimination sequence revealed a highly non-linear relationship between the number of retained wavelengths and detection performance (Figure 5.4). CRACK PR–AUC remained within 0.5 % of its maximum (0.9948) down to 11 wavelengths, and within 1.0 % down to 9 wavelengths (Table 5.16). These results indicate that the vast majority of the 159 usable channels carry redundant spectral information for the specific task of crack detection, and that the discriminative signal is concentrated in a small number of spectral regions. This high redundancy is a well-known property of contiguous hyperspectral data, where adjacent bands are often correlated at $r > 0.99$ Bioucas-Dias et al., 2013; Liu et al., 2022.
The practical implication is substantial. A full hyperspectral line-scan camera typically costs between $30,000 and $100,000, requires specialised data handling, and generates datasets measured in hundreds of gigabytes per field campaign Bhargava et al., 2024. A multispectral sensor configured with 9–30 narrowband filters can be manufactured for a fraction of this cost, operates at higher frame rates, and produces data volumes that are orders of magnitude smaller Benelli et al., 2020. The BFS results provide a quantitative justification for the transition from hyperspectral research prototype to multispectral operational sensor, echoing the band-reduction strategies that have proven effective in other agricultural HSI applications Khaled et al., 2023; Liu et al., 2022; Z. Zhang et al., 2024.
It is noteworthy that the CRACK F1 metric exhibited a different optimisation landscape

from PR–AUC, with its maximum achieved only at 159 wavelengths and a more gradual decline as features were removed (Figure 5.5). This discrepancy reflects the fact that F1 penalises both false positives and false negatives equally, and that finer spectral resolution helps to separate crack signatures from spectrally similar background materials. For early-warning applications in which sensitivity (recall) is prioritised over specificity, the PR–AUC-oriented subset is the more appropriate choice; for applications demanding high precision, a larger wavelength subset may be warranted.

6.5.2 Stability Across Random Seeds and Sensor Design Implications

The stability analysis across five random seeds exposed a methodologically important finding: the *identity* of the selected wavelengths is moderately sensitive to the data partition, even when the *number and performance* of the selected bands remain stable (Table 5.19). The best CRACK PR–AUC ranged from 0.812 to 0.998 across seeds, and the optimal number of features varied between 64 and 153, revealing substantial sensitivity to the calibration–validation partition. Mean pairwise Jaccard similarity was 0.493 for the top-30 subsets and 0.398 for the top-11 subsets (Tables 5.20–5.21), indicating that roughly half of the selected wavelengths change from one random split to another.

This level of variability is not unexpected in wrapper-based feature selection on high-dimensional, correlated data Liu et al., 2022: when adjacent spectral channels are highly collinear, BFS can substitute one for another without measurable loss, producing different subsets that are functionally equivalent. Similar instability has been reported in filter-based hyperspectral band selection studies, where mutual-information and Fisher-score methods often yield non-unique solutions when inter-band correlation is high Ding et al., 2023; Gu et al., 2012; Vergara and Estévez, 2014. The key finding is that certain wavelengths resist this substitution entirely. The four universally stable wavelengths—452.25, 548.55, 580.90, and 729.53 nm—were retained by every seed at both the 11-feature and 30-feature levels (Figures 5.10–5.8).

These four wavelengths anchor the sensor design recommendation of this study. Their spectral locations correspond to physiologically interpretable regions: the Soret band (452 nm), the green reflectance trough (548 nm), the anthocyanin shoulder (580 nm), and the red-edge inflection (729 nm), as discussed in Section 6. A multispectral sensor incorporating these four channels, supplemented by additional bands drawn from the broader intersection set (13 common wavelengths at the 30-feature level), would capture the essential information for crack detection while minimising hardware complexity. This approach is consistent with the emerging trend in precision agriculture toward application-specific multispectral sensors that target physiologically meaningful bands rather than employing full hyperspectral coverage Benelli et al., 2020; Ram et al., 2024.

An important caveat is that this stability analysis was conducted on a single cultivar ('Scarlotta') in a single growing region (Lachish, Israel). Other cultivars with different anthocyanin profiles, cuticle thickness, or mesocarp water content may shift the optimal wavelength positions Chang and Keller, 2021; Khadivi-Khub, 2014. Cross-cultivar validation experiments would be needed before recommending a fixed filter configuration for commercial deployment.

6.6 Generalization Gaps Between Calibration and Test Sets

Across every experimental configuration examined in this study, test-set performance was consistently lower than calibration-set performance, revealing a generalization gap that warrants careful interpretation (Table 5.18). The gap was particularly pronounced in the late-stage scenario, where the MCC dropped from 0.877–0.897 on the calibration split to 0.605–0.665 on the test split, representing a reduction of more than 20 percentage points. The early-stage gap was narrower in absolute terms (approximately 6–15 percentage points), but the baseline performance was also lower, meaning that the test-set MCC hovered between 0.587 and 0.645.

Several factors contribute to this pattern. The most fundamental is the difference in data provenance between the calibration and test sets. By design, calibration images were drawn from Row 1 of the vineyard, while test images came from Row 2 (Table 5.13). Although both rows belonged to the same experimental vineyard and experienced the same irrigation treatments, they differed in vine age uniformity, canopy architecture, and micro-environmental conditions such as wind exposure and shading. These factors introduce a spatial domain shift—a systematic difference in the joint distribution of spectral features and labels—that is invisible during cross-validation within a single row but manifests as a performance drop when the model is applied to a new spatial domain. Such spatial domain shifts are increasingly recognised as a major challenge in agricultural remote sensing, where models trained on one field or plot often degrade when transferred to another, even within the same farm Fass et al., 2025; Ram et al., 2024. Kaltenborn et al. Kaltenborn et al., 2025 and Li et al. Li et al., 2023 have emphasised that proper data splitting is essential to avoid information leakage in hyperspectral classification, and the row-based spatial split used in this study represents a conservative strategy that exposes rather than conceals the generalization challenge Kaufman et al., 2012.

The interaction between the number of retained wavelengths and the generalization gap adds nuance (Table 5.18). For the early-stage scenario, the 30-wavelength subset produced the highest test MCC (0.6447) and a moderate gap (0.0785), whereas the 9-wavelength configuration yielded a larger gap (0.1508) and the full 159-wavelength cube

yielded a gap of 0.0560 but a lower absolute test MCC (0.6071). This non-monotonic pattern suggests that an intermediate level of spectral dimensionality strikes a balance between under-fitting (too few features to capture the signal) and over-fitting (too many features that encode row-specific noise). The 30-wavelength configuration may therefore represent a practically optimal compromise between signal retention and generalization stability, an observation consistent with well-known bias–variance trade-off principles Menze et al., 2009.

For the late-stage scenario, the generalization gaps were uniformly larger (0.21–0.29; Table 5.18), likely because the higher calibration MCC reflects over-optimisation of the post-processing thresholds on the more separable late-stage data. When these thresholds are applied to the test row, the mismatch between the calibration and test spectral distributions becomes more consequential.

For future operational systems, these generalization gaps have direct implications. Models calibrated on one section of a vineyard—or one season—should not be deployed without adaptation to a new section or a new season. Transfer-learning strategies, domain-adaptation techniques, or ensemble approaches that incorporate data from multiple rows and time points could mitigate this limitation and are recommended as a priority for future research.

6.7 Supervised Classification versus Anomaly Detection

A deliberate objective of this study was to compare supervised and unsupervised approaches to crack detection, both at the pixel level and within the full-image pipeline. The comparison yielded a clear and instructive conclusion: supervised classifiers consistently outperformed autoencoder-based anomaly detection, and the margin of superiority widened as the task complexity increased.

At the pixel level, the autoencoder trained exclusively on cracked pixels performed surprisingly well in the multi-class setting, achieving accuracy above 0.96 and PR–AUC of 0.9999 (Table 5.10). This success can be attributed to the narrow spectral manifold learned by the model: crack signatures occupy a well-defined region of the spectral space, and all other classes (leaf, wood, soil, plastic, healthy tissue) produce larger reconstruction errors precisely because they are spectrally dissimilar. This finding is consistent with the spectral separability analysis (Table 5.2), which showed that cracked tissue occupies a distinct low-reflectance region in both VIS and NIR, well separated from the other vineyard materials.

The reverse configuration—training on all classes except cracked and flagging high reconstruction error as anomalous—failed almost completely, with cracked-class recall of 0.000

under balanced sampling and 0.011–0.111 under unbalanced sampling (Table 5.12). This failure is not incidental; it reflects a fundamental property of the spectral space. Because the non-crack classes span a much wider spectral range (from soil and plastic in the VIS to leaf and wood in the NIR), the autoencoder learns a reconstruction manifold that is broad enough to accommodate crack spectra as well. The reconstruction error for crack pixels is therefore no larger than for normal tissue, eliminating the anomaly-detection signal. This finding aligns with the theoretical analysis of anomaly detection in high-dimensional spaces: when the normal class is heterogeneous, the learned representation often generalises to anomalous samples that fall within the convex hull of the training manifold Gewali et al., 2022.

At the whole-image level, the autoencoder-based pipeline achieved a test MCC of only -0.058 in the early-stage scenario (Table 5.15), indicating performance indistinguishable from—or slightly worse than—chance. Even in the late-stage scenario, where cracks are macroscopically visible, the autoencoder pipeline underperformed the supervised classifier by approximately 22 MCC points (0.375 vs. 0.598; cf. Tables 5.15 and 5.14). The degradation from pixel to whole-image level was substantially more severe for the autoencoder than for the supervised model, because the autoencoder's pseudo-probability scores—derived from an exponential mapping of reconstruction errors (e.g., $p_{\text{CRACK}}(x) = \exp(-e(x)/\tau)$)—are less calibrated than the true posterior probabilities produced by the supervised XGBoost classifier T. Chen and Guestrin, 2016. When these poorly calibrated scores are propagated through the same spatial post-processing pipeline, the resulting image-level decisions become unreliable.

These results lead to a clear recommendation: for crack detection in table grapes, the supervised classification paradigm is strongly preferred. Anomaly detection approaches may remain relevant for applications in which labelled training data are genuinely unavailable, but in the context of this study—where SAM2-assisted annotation Ravi et al., 2024 made large-scale pixel-level labelling feasible—the investment in labelled data pays dividends in detection accuracy.

An additional insight emerges from the asymmetry between the two autoencoder training strategies. The crack-trained autoencoder's success suggests that cracked tissue possesses a coherent, low-dimensional spectral signature that is well-separated from other vineyard materials. This property is itself a validation of the spectral distinguishability hypothesis (Hypothesis 1) and reinforces the argument that cracking induces a characteristic and physically interpretable spectral alteration.

6.8 Practical Implications for Precision Viticulture

The results of this study translate into several actionable recommendations for the grape industry, situated within the broader context of precision agriculture and data-driven

crop management Mgendi, 2024; Soussi et al., 2024.

The first and most immediate implication is that hyperspectral imaging, even in its current portable configuration (Specim IQ; Behmann et al., 2018), can provide a practical early-warning screening signal for cracking susceptibility. A grower who images grape clusters during the early ripening period and processes each scene through the whole-image spatial aggregation pipeline described in this study can obtain a conservative warning signal weeks earlier than visual scouting alone. This lead time could be exploited to adjust irrigation scheduling—a well-established lever for managing berry turgor and cracking risk Chang et al., 2019; Khadivi-Khub, 2014—apply targeted calcium or sorbitol-based spray treatments Guirao et al., 2025; La Spada et al., 2024, or advance the harvest of at-risk sections. The economic significance of such advance warning is considerable: cracking causes not only direct yield losses but also facilitates secondary fungal infection, particularly sour rot, which further reduces marketability Hall et al., 2018; Owoyemi et al., 2024.

From an operational perspective, the most plausible near-term deployment workflow supported by the present data is *non-destructive single-acquisition screening with conservative, calibrated warnings*. Concretely, each imaged cluster scene would be processed end-to-end with the same spectral model *and* the spatial aggregation stage (morphological filtering and crack-percentage decision) that was tuned on the calibration split (Section 6.3; Table 5.14). The output should be interpreted as a cluster-level screening score for that acquisition, recognizing that the whole-image pipeline is explicitly designed to suppress background-induced false positives that dominate field scenes. The data support two implementable refinements: (i) a reduced-band configuration can be used without sacrificing—and in the early-stage case even improving—independent Row 2 performance (Table 5.17), and (ii) the BFS stability results provide a physically grounded starting point for a future multispectral device (452.25, 548.55, 580.90, 729.53 nm; Figures 5.10–5.8) that could make such screening cheaper and higher-throughput. By contrast, moving from this calibrated workflow to *standalone* decision thresholds that generalize across rows, cultivars, and seasons remains future work, given the observed calibration-to-test generalization gaps (Table 5.18) and the current reliance on calibration-tuned post-processing.

The second implication concerns sensor cost. The BFS analysis demonstrates that 9–30 carefully chosen wavelengths capture essentially the same information as the full 159-channel spectrum (Table 5.16). This finding opens the door to custom multispectral cameras—potentially mounted on unmanned aerial vehicles (UAVs) or tractor-mounted platforms—that combine high throughput with low per-unit cost Benelli et al., 2020; Ram et al., 2024. The four universally stable wavelengths identified by the stability analysis (452, 548, 580, 729 nm) provide a concrete starting point for filter specification. This transition from hyperspectral to multispectral is an active frontier in precision agriculture,

where application-specific band selection has been shown to yield cost-effective screening solutions without sacrificing performance Fass et al., 2025; Khaled et al., 2023. The CrackSense project Alchanatis et al., 2022, a Horizon Europe initiative focused on real-time sensing and early warning of fruit cracking, shares this vision of scalable sensing for cracking management.

The third implication relates to the full-image pipeline architecture. The study demonstrates that pixel-level classifiers, however accurate in isolation, require spatial post-processing (morphological filtering, patch aggregation, threshold optimisation) to translate spectral classification outputs into actionable vineyard-level decisions. This multi-stage architecture—pixel classification, spatial aggregation, and calibrated thresholding—constitutes a deployable decision-support system that can be embedded in existing vineyard management platforms Ahmed and Shakoor, 2025; Krisnawijaya et al., 2022.

Finally, the observed sensitivity to water-related spectral features suggests that hyperspectral sensing could serve a dual purpose: screening cracking risk and simultaneously assessing vine water status. These two applications are physiologically linked through berry turgor and cuticle permeability Chang et al., 2019; Yu et al., 2025, and a single imaging survey could inform both irrigation management and harvest-timing decisions. This synergy between cracking early-warning screening and water-status assessment represents a compelling value proposition for growers considering investment in spectral sensing infrastructure.

6.9 Limitations of the Study

Despite the breadth of the experimental programme, several limitations should be acknowledged because they constrain how the reported metrics should be interpreted and how the system could be deployed.

- **Single cultivar, site, and season.** All experiments were conducted on a single cracking-susceptible cultivar ('Scarlotta Seedless') in one region and one growing season. The wavelength subsets and performance levels reported here may shift under different anthocyanin profiles, cuticle properties, and phenological timing Chang and Keller, 2021; Khadivi-Khub, 2014. *Implication:* results should be treated as cultivar- and site-conditional evidence; operational use would require re-validation (and potentially re-calibration) across cultivars and seasons.

- **Observed spatial domain shift (Row 1 → Row 2) limits transfer.** The experimental design intentionally used a spatially separated test row, and the resulting calibration-to-test drops (Table 5.18) demonstrate that performance is sensitive to spatial domain shift even within a single vineyard. *Implication:* a model tuned on

one block/row should not be assumed to transfer unchanged to another; deployment should incorporate periodic re-calibration, multi-row training data, or explicit domain-adaptation strategies.

- **Field illumination and scene complexity are a dominant error source.** Whole-image performance was substantially lower than pixel-level performance (Tables 5.3–5.4 vs. Table 5.14), consistent with uncontrolled illumination geometry, BRDF/specular effects on curved berries, and background clutter in vineyard scenes (Section 6.3). *Implication:* reported whole-image metrics already reflect these real-world factors, but robustness in new lighting/canopy conditions may require stricter acquisition protocols (e.g., standardized geometry, shading control) and/or improved radiometric and spectral–spatial normalization.

- **Pixel-level labels are not perfectly objective.** Although SAM2-assisted annotation enabled scale Ravi et al., 2024, boundaries between crack and intact tissue are ambiguous at the pixel scale (mixed pixels, sub-pixel fissures, and stain/shadow artefacts). This introduces label noise that can inflate or depress pixel-level metrics and can propagate into the full-image pipeline. *Implication:* pixel-level "near-ceiling" results should be interpreted as conditional on the labeling protocol; future work should quantify inter-annotator consistency or use uncertainty-aware labels for boundary regions.

- **Sensor spatial resolution imposes a detection floor.** The Specim IQ resolution (approximately 1.08 mm per pixel at 1 m; Behmann et al., 2018) limits sensitivity to micro-fissures and increases mixed-pixel ambiguity at crack edges Bioucas-Dias et al., 2013. *Implication:* early-stage cracking that is smaller than a few pixels may be missed even if a physiological signal exists; higher-resolution imaging, closer working distances, or patch-based spectral–spatial models are likely required for reliable micro-crack detection.

- **Post-processing and threshold tuning were optimized on a small calibration set.** The whole-image decision depends on probability thresholds, morphological kernels, and crack-percentage criteria optimized via Optuna on Row 1 (Table 5.13). The fact that these parameters did not eliminate the generalization gap (Table 5.18) indicates residual sensitivity to distribution shift. *Implication:* in deployment, thresholds should be monitored for drift and re-tuned as conditions change; conservative operating points (higher precision, lower recall) may be preferable for early-warning screening.

6.10 Future Research Directions

The findings and limitations of this study suggest several concrete directions for future investigation, ordered by scientific priority and practical impact.

The highest priority is multi-season validation. The models should be re-trained and tested on data from at least two additional growing seasons to assess cross-season generalization and to determine whether the calibration-to-test gap can be reduced through more diverse training data and improved calibration protocols. Given that environmental forcing, vine physiology, and cracking incidence vary inter-annually Chang et al., 2019; Khadivi-Khub, 2014, robustness cannot be assumed from a single-season study.

A second priority is cross-cultivar generalisation. Experiments on cultivars with contrasting skin properties—thin-cuticle varieties prone to cracking versus thick-cuticle varieties that are resistant—would reveal whether the four stable wavelengths have universal relevance or are cultivar-specific. Santos et al. Santos et al., 2023 reviewed the molecular mechanisms underlying fruit cracking across species, and cross-cultivar spectral studies would establish whether common physiological pathways produce transferable spectral signatures.

Third, the integration of spatial models deserves attention. The current pipeline treats each pixel independently and relies on post-hoc morphological filtering for spatial coherence. Convolutional or transformer-based architectures that jointly reason over spatial neighbourhoods and spectral channels Z. Chen et al., 2024; Dhanya et al., 2022 could learn to distinguish true crack boundaries from background edges, potentially eliminating the need for hand-tuned post-processing parameters and improving robustness under variable field conditions.

Fourth, the complementary thermal data acquired during this study offer an opportunity for multi-modal fusion. A combined spectral-thermal model could exploit the distinct failure signatures captured by each modality: spectral changes in reflectance associated with pigment and water loss, and thermal anomalies associated with altered evaporative cooling at crack sites Mahlein, 2016.

Fifth, the BFS-derived wavelength subsets should be validated using a physical multispectral sensor rather than by computationally subsetting the hyperspectral cube. A true hardware validation would account for differences in filter bandwidth, signal-to-noise ratio, and radiometric calibration that are abstracted away in a simulation-based feature selection Benelli et al., 2020. This validation step is essential before recommending the four-wavelength configuration for commercial sensor manufacturing.

Sixth, the autoencoder-based anomaly detection framework could be revisited with more expressive generative models. Variational autoencoders with spectral-specific priors, normalizing flows, or diffusion-based models could provide sharper reconstruction boundaries and improved anomaly scoring, particularly in the non-crack training configuration that

failed comprehensively in the present study.
Finally, the operational deployment of the pipeline on UAV-mounted or tractor-mounted multispectral platforms should be piloted. Such a deployment would test the end-to-end system under realistic throughput, altitude, and illumination conditions, and would provide the evidence base needed for commercial adoption by the viticulture industry Alchanatis et al., 2022; Mgendi, 2024.

6.11 Concluding Perspective

This study began with a straightforward question: can hyperspectral imaging detect grape cracking? The answer—emphatically supported at the pixel level and cautiously affirmed at the whole-image level—opens a broader vista.
The spectral markers identified here are not arbitrary correlates; they reflect the physical and physiological processes that precede and accompany cuticle failure: pigment degradation Blackburn, 2007; Castellarin and other, 2016, water loss Chang et al., 2019; Yu et al., 2025, altered scattering, and red-edge suppression Thenkarail et al., 2016. The fact that these markers are detectable before macroscopic cracking appears transforms the paradigm from reactive visual inspection to proactive, non-destructive early-warning detection—a shift with immediate consequences for vineyard management.
The pathway from a 159-channel research camera to a compact multispectral sensor with fewer than a dozen filters is now quantitatively justified by the BFS and stability analyses (Tables 5.16–5.21; Figures 5.10–5.9). The four universally stable wavelengths provide a minimal spectral fingerprint that is both physiologically grounded and computationally robust, offering a bridge between laboratory science and vineyard operations.
At the same time, the generalization gaps documented in this study (Table 5.18) serve as a necessary reminder that spectral models, like all empirical tools, require continued validation as cultivars, seasons, and management practices change García-Vera et al., 2024; Ram et al., 2024. The contribution of the present work lies not only in the specific models and wavelengths reported, but in the methodological framework—from pixel-level spectral analysis through spatially informed aggregation to stability-guided sensor design—that can be adapted and extended as new data become available.
In the broader context of precision viticulture, this research demonstrates that early, non-destructive crop screening using spectral sensing is not merely a theoretical possibility but an operational strategy within reach Alchanatis et al., 2022; Mgendi, 2024. Closing the remaining gaps—multi-season validation, cross-cultivar testing, multi-modal fusion, and hardware integration—will bring this strategy from the research vineyard to the commercial field.

Chapter 7

Conclusions and Future Work

7.1 Summary of Main Contributions

This research addressed a critical challenge in viticulture: the early detection of grape cracking under realistic field conditions using non-destructive hyperspectral imaging technology. The investigation yielded four principal contributions that advance both the scientific understanding of spectral crack detection and its practical feasibility for agricultural deployment.

First, at the pixel level, this study demonstrated that visible–near-infrared (VIS–NIR) hyperspectral imaging in the 450–925 nm range, combined with Standard Normal Variate (SNV) normalization and supervised machine learning, can distinguish cracked from healthy grape tissue with exceptional precision. An XGBoost classifier achieved approximately 97 % accuracy and an area under the ROC curve (AUC) of 0.99 on carefully labelled spectral signatures. This finding establishes a clear physical and algorithmic foundation: the spectral reflectance properties of cracked and healthy berry skin differ measurably and consistently within the VIS–NIR region, validating the use of hyperspectral sensing for crack-related tissue characterization.

Second, recognizing that pixel-level performance alone is insufficient for practical deployment, this work developed and validated a full-image crack-detection pipeline that bridges the gap between controlled spectral classification and complex field-scene inference. By aggregating pixel-level outputs through spatial post-processing—including probability thresholding, morphological filtering, and patch-based decision rules—the pipeline achieved meaningful detection performance on independent test data under early- and late-stage acquisition conditions. On a held-out test row, the system attained $F1_{CRACK}$ of 0.704 (MCC = 0.504) for early-stage images, where cracking is minimal or incipient, and $F1_{CRACK}$ of 0.818 (MCC = 0.598) for late-stage images, where cracks are macroscopically visible. These results demonstrate that crack-related spectral signatures remain detectable even in the presence of complex background clutter, mixed pixels, and vari-

able illumination, provided that spatial context is appropriately leveraged.

Third, backward feature selection (BFS) experiments revealed that the 159-wavelength hyperspectral cube can be reduced to as few as 11 bands with minimal loss in crack-detection performance, and that a 30-wavelength subset can match or even exceed full-spectrum results on independent test data. Stability analysis across multiple random seeds identified four wavelengths—452.25, 548.55, 580.90, and 729.53 nm—that were selected universally, corresponding to physiologically interpretable regions (chlorophyll Soret band, green reflectance trough, anthocyanin shoulder, and red-edge inflection). This finding provides a quantitative foundation for transitioning from costly, data-intensive hyperspectral line-scan cameras to compact, cost-effective multispectral sensors optimized for grape crack detection, thereby supporting a pathway toward scalable agricultural deployment.

Fourth, a systematic comparison of supervised classification and unsupervised anomaly detection approaches exposed a critical asymmetry. Whereas supervised models trained on labelled cracked and healthy spectra generalized robustly, autoencoder-based anomaly detectors—when trained exclusively on non-crack tissue—failed catastrophically at the system level, achieving an MCC of -0.058 under early-stage conditions. This negative result clarifies the algorithmic requirements for field deployment: effective crack detection in grape clusters demands explicit representation of crack-class spectral signatures, rather than reliance on generic outlier-detection frameworks.

Taken together, these contributions represent the first comprehensive demonstration of early-stage crack detection in table grapes using hyperspectral imaging under realistic vineyard conditions. The research establishes both the scientific feasibility and the practical constraints of spectral crack sensing, offering a foundation for future precision viticulture technologies.

7.2 Direct Answer to the Research Question

The central research question posed in Chapter 1 was:

> *Can hyperspectral imaging detect spectral signatures of grape cracking at the time of measurement under field conditions, and if so, to what extent can detection be achieved during the early stages of crack development?*

The answer is **yes, with important operational qualifications**.

Hyperspectral imaging in the VIS–NIR range can reliably detect crack-related spectral signatures in grape berries at the time of measurement. At the pixel level, where individual spectra are drawn from well-defined tissue regions, the discrimination between cracked and healthy signatures is near-perfect. This establishes that cracking induces measurable and consistent changes in reflectance properties—most notably, depressed

near-infrared reflectance and altered red-edge characteristics—that are attributable to turgor loss, cellular dehydration, cuticle disruption, and pigment degradation.

However, the transition from pixel-level spectral classification to full-image field detection introduces substantial challenges. Mixed pixels, variable illumination geometry, and spectrally confounding background materials (leaves, woody tissue, plastic supports) all degrade performance when models are deployed on whole hyperspectral scenes. The solution developed in this work—spatial aggregation through morphological filtering and patch-based decision criteria—demonstrates that these challenges are surmountable, but not trivial. System-level performance is markedly lower than pixel-level benchmarks, yet it remains operationally meaningful.

Regarding early-stage detection, the results are encouraging but tempered by realism. Early-stage acquisitions, corresponding to absent-to-minimal cracking (the first recorded small-crack stage for individual cluster identities), yielded test-set $F1_{\text{CRACK}}$ of 0.704 and MCC of 0.504. These values fall short of the late-stage benchmark ($F1_{\text{CRACK}} = 0.818$, MCC = 0.598) yet confirm that crack-related physiological changes—including incipient turgor disruption and micro-fracturing—produce detectable spectral shifts before macroscopic splitting becomes visually obvious. Early-stage detection is therefore *feasible*, but requires careful system design, robust spatial processing, and acceptance of higher false-negative rates relative to late-stage scenarios.

In summary, hyperspectral imaging can detect grape cracking under field conditions, including at early developmental stages, provided that pixel-level classification is coupled with spatial aggregation strategies tailored to the operational constraints of vineyard imaging.

7.3 Validation of Research Hypotheses

The five research hypotheses stated in Chapter 3 were systematically evaluated against the experimental results reported in Chapter 5 and interpreted in Chapter 6. A concise summary follows.

- **Hypothesis 1 (Spectral distinguishability): CONFIRMED.** Clear and statistically significant differences were observed between healthy and cracked grape tissue across the 450–925 nm range. Mean reflectance, Cohen's d separability scores, and Fisher discriminant ratios all confirmed strong spectral separation, with the most pronounced differences concentrated in the red-edge and NIR regions. This provides the physical basis for algorithmic discrimination.

- **Hypothesis 2 (Pixel-level classification feasibility): CONFIRMED.** Supervised machine learning models, particularly XGBoost, achieved near-ceiling performance on pixel-level spectral classification under both balanced and unbalanced

class regimes. Accuracy exceeded 97 %, and ROC–AUC reached 0.99, demonstrating that the spectral decision boundary is well-defined and learnable.

- **Hypothesis 3 (Whole-image robustness): CONFIRMED.** When deployed on full hyperspectral scenes containing complex background content, the end-to-end detection pipeline retained meaningful precision and recall on an independent held-out test row. While performance degraded relative to pixel-level benchmarks, the system achieved operationally relevant F1 scores and MCC values, confirming that crack signatures can be distinguished from background clutter when spatial aggregation is applied.

- **Hypothesis 4 (Early detection capability): PARTIALLY CONFIRMED.** Early-stage images, acquired when cracking was minimal or incipient, were classified above chance on the held-out test set, with $F1_{\text{CRACK}} = 0.704$ and MCC = 0.504. These values are lower than late-stage performance but demonstrate that crack-related spectral changes are detectable before macroscopic symptoms become clearly visible. The hypothesis is therefore supported with the qualification that early-stage detection operates at reduced sensitivity compared to late-stage scenarios.

- **Hypothesis 5 (Spectral efficiency): CONFIRMED.** Backward feature selection demonstrated that strong crack-detection performance can be maintained with drastically reduced wavelength subsets. An 11-band configuration matched the full 159-band spectrum within 0.5 % PR–AUC, and a 30-band subset exceeded the full-spectrum baseline on the independent test set. This confirms that hyperspectral redundancy can be exploited to support compact, cost-effective multispectral sensor designs.

In aggregate, the experimental evidence supports the core hypotheses of this research, with the notable caveat that early-stage detection—while feasible—requires acceptance of higher uncertainty relative to late-stage detection. The findings validate the proposed methodological framework and establish hyperspectral imaging as a viable tool for non-destructive grape crack assessment.

7.4 Practical Implications and Applications

The findings of this research have direct implications for viticulture practitioners, sensor manufacturers, and the broader precision agriculture community.

For viticulture practitioners, the demonstrated feasibility of early-stage crack detection opens a pathway toward non-destructive, proactive vineyard management. Current practice typically relies on visual inspection, which is labor-intensive, subjective, and

occurs only after macroscopic damage is evident. By the time cracking is visually obvious, secondary infections such as sour rot may already be underway, reducing both yield and marketable quality. A hyperspectral-based early-warning system could enable growers to identify at-risk clusters days or weeks before visible splitting, facilitating targeted interventions such as protective sprays, adjusted irrigation schedules, or selective early harvest. The economic value of such interventions is substantial: grape cracking and associated rots account for losses exceeding 20 % of marketable yield in susceptible cultivars under favorable climatic conditions. Even modest reductions in loss rates would justify the deployment costs of spectral monitoring systems.

For sensor manufacturers and agricultural technology developers, the wavelength-selection results provide concrete design specifications for next-generation crack-detection sensors. Rather than deploying full hyperspectral line-scan cameras—which are expensive, data-intensive, and require specialized handling—manufacturers can develop compact multispectral imagers incorporating the identified optimal bands (452, 548, 580, 729 nm, supplemented by additional red-edge and NIR channels). Such sensors would be smaller, lighter, cheaper to produce, and capable of higher frame rates than research-grade hyperspectral systems, making them suitable for integration with robotic vineyard platforms, unmanned aerial vehicles (UAVs), or handheld assessment tools. The reduced data volume would also simplify real-time processing requirements, enabling on-device inference rather than cloud-based post-processing.

For precision agriculture more broadly, this work exemplifies a generalizable strategy for translating laboratory-grade spectroscopic measurements into field-deployable sensing systems. The documented gap between pixel-level classification success and whole-image field performance is not unique to grape crack detection; it recurs across agricultural HSI applications targeting disease detection, nutrient stress, and fruit quality assessment. The spatial aggregation framework developed here—morphological filtering, patch-based decision rules, and Optuna-driven hyperparameter optimization—represents a reusable template for bridging that gap in other crops and other physiological disorders.

Scalability and deployment pathway. Transitioning from the research prototype demonstrated here to operational vineyard deployment will require addressing several practical constraints. First, acquisition speed must increase: the push-broom line-scan configuration used in this study is effective for controlled field sampling but would require motorized translation stages or integration with vineyard rovers for systematic row-by-row coverage. Snapshot multispectral cameras offer a faster alternative, sacrificing spectral resolution for higher spatial throughput. Second, computational requirements for real-time inference must be minimized. The XGBoost classifier used here is computationally lightweight and amenable to embedded deployment, but the full post-processing pipeline (including morphological operations on megapixel-scale probability maps) may require GPU acceleration or edge-computing hardware. Third, environmental robustness must

be validated: the models presented here were trained and tested under specific vineyard conditions (single cultivar, specific phenological stages, particular illumination and weather patterns). Generalization to other cultivars, regions, and growing conditions will require transfer learning, domain adaptation, or expanded training datasets.

Nonetheless, the technical foundation established by this work supports a clear pathway: wavelength-optimized multispectral imaging, coupled with spatial aggregation and supervised classification, can deliver operationally useful crack detection under realistic field constraints. The next step is engineering translation: ruggedizing sensors, optimizing inference pipelines, and validating performance across diverse operational contexts.

7.5 Limitations of the Study

The findings reported in this thesis must be interpreted within the context of several methodological and operational constraints.

First, the study focused exclusively on a single table grape cultivar ('Scarlotta') grown under specific vineyard management practices in a defined climatic region. While this cultivar exhibits pronounced cracking susceptibility—making it an appropriate target for proof-of-concept work—the spectral signatures of cracking may differ in other grape varieties due to variations in skin pigmentation (anthocyanin content and distribution), cuticle thickness, berry size, and physiological response to water stress. Generalization of the trained models to red versus white grapes, table versus wine varieties, or cultivars grown under different soil, irrigation, or canopy-management regimes has not been validated. The extent to which the identified optimal wavelengths (452, 548, 580, 729 nm) remain universally informative across cultivars is an open empirical question.

Second, the temporal scope of data acquisition was constrained to specific phenological stages during the ripening period. No attempt was made to track individual clusters longitudinally from véraison through harvest, and consequently, the study does not model crack *progression* over time. The early-stage and late-stage acquisition subsets used for evaluation reflect snapshots at different crack-severity levels, not temporal sequences from the same biological entity. This design choice—driven by logistical and labeling constraints—precludes direct modeling of crack development dynamics and limits the ability to make statements about *forecasting* future cracking events.

Third, the dataset size, while sufficient for demonstrating proof-of-concept, remains modest relative to the scale typical of modern deep-learning computer-vision applications. The whole-image evaluation involved 60 unique clusters per test row under each acquisition-stage condition, and pixel-level training utilized spectra sampled from a similarly limited biological sample. Larger datasets, drawn from multiple vineyards, seasons, and cultivars, would improve model robustness and enable more rigorous assessment of generalization.

Fourth, the spatial resolution and field-of-view of the Specim IQ hyperspectral camera

(approximately 1.08 mm per pixel at 1 m working distance) introduce mixed-pixel effects at tissue boundaries and limit the detection of micro-cracks smaller than a few millimeters. Finer spatial resolution would improve early-stage sensitivity but at the cost of increased data volume and processing time. The trade-off between spatial resolution, spectral resolution, and acquisition speed remains a fundamental constraint in field HSI applications.

Fifth, the full-image detection pipeline demonstrated here operates on post-processed hyperspectral cubes and requires iterative hyperparameter tuning (via Optuna on a calibration split). Real-time deployment in a moving vineyard platform would necessitate either pre-calibrated fixed thresholds (which may not generalize across rows or vineyard blocks) or adaptive threshold estimation, introducing additional algorithmic complexity. These limitations do not invalidate the core findings but rather define the boundary conditions within which the results hold. Future work extending the approach to additional cultivars, regions, and operational scenarios will clarify the extent to which the demonstrated performance generalizes.

7.6 Future Research Directions

The findings of this research open multiple avenues for follow-on investigation, spanning immediate technical validation, medium-term algorithmic development, and long-term integration into operational precision viticulture systems.

7.6.1 Short-Term Extensions: Validation and Robustness

The most immediate priority is to validate the spectral crack-detection framework across a broader range of grape cultivars and growing conditions. Repeating the pixel-level classification and full-image detection experiments on red versus white table grapes, wine grape varieties, and cultivars exhibiting varying degrees of crack susceptibility would clarify the extent to which the identified spectral signatures and optimal wavelengths generalize. Similarly, testing the approach across multiple vineyard sites—encompassing different soil types, irrigation regimes, canopy-management practices, and climatic conditions—would expose environmental factors that modulate reflectance properties and detection performance.

A second short-term extension involves refining the spatial aggregation pipeline for real-time deployment. The current implementation relies on post-hoc hyperparameter tuning via Optuna on a calibration split. Developing adaptive thresholding strategies that adjust probability cutoffs, morphological kernel sizes, and patch-aggregation criteria based on per-image statistics (e.g., overall crack prevalence, illumination uniformity, background clutter density) would improve robustness when the system encounters vineyard blocks

or acquisition conditions that differ from the calibration set. Additionally, exploring alternative spatial processing frameworks—such as superpixel segmentation, graph-based label propagation, or conditional random fields—may yield further performance gains.
A third priority is to extend temporal coverage by acquiring hyperspectral data throughout the entire ripening trajectory, from véraison through late harvest, for longitudinally tracked individual grape clusters. Such data would enable analysis of crack *progression* dynamics and could support models that predict the likelihood of future cracking based on current spectral measurements combined with environmental covariates (temperature, humidity, rainfall events). This would move the system from reactive *detection* toward proactive *forecasting*, substantially increasing its operational value.

7.6.2 Medium-Term Opportunities: Multi-Modal Integration and Transfer Learning

At the medium term, integrating hyperspectral imaging with complementary sensing modalities offers the potential to capture a richer representation of grape physiological state. Thermal infrared imaging, for example, measures canopy and berry surface temperature and can infer transpiration rates and water stress—physiological precursors to cracking. Combining VIS–NIR reflectance with thermal emissivity in a multi-modal classification framework could improve early-stage detection sensitivity by jointly modeling optical and thermal signatures of turgor loss.
Similarly, high-resolution RGB-D cameras (combining color imaging with depth sensing) could provide detailed surface geometry, enabling detection of micro-topographic irregularities (surface roughening, incipient cuticle fractures) that precede full mechanical failure. Fusing spectral, thermal, and geometric features within a unified deep-learning architecture—such as a multi-stream convolutional neural network—represents a natural evolution of the supervised-classification approach demonstrated here.
Transfer learning offers another promising direction. Rather than training separate models for each cultivar or vineyard, a base model trained on a diverse multi-cultivar dataset could be fine-tuned with a small number of target-specific samples. This would reduce the labeling burden when deploying the system in new vineyards and accelerate adoption by practitioners lacking the resources to collect large annotated datasets. Recent advances in self-supervised pre-training for hyperspectral imagery and few-shot learning frameworks could be leveraged to this end.
Additionally, the wavelength-selection experiments conducted here identified a compact subset of informative bands. Follow-on work should validate these findings by physically constructing a custom multispectral sensor incorporating the optimal wavelengths and comparing its field performance directly against the full hyperspectral baseline. Such an applied-engineering validation step is essential before commercial sensor manufacturers

will commit to production.

7.6.3 Long-Term Vision: Autonomous Systems and Decision Support

The ultimate long-term vision is a fully autonomous vineyard monitoring system that integrates crack detection with broader precision viticulture decision support. Such a system would combine:

- Robotic ground platforms or UAVs equipped with multispectral cameras, traversing vineyard rows on scheduled or on-demand missions;
- Real-time on-board inference using embedded classifiers (e.g., quantized XGBoost models or lightweight convolutional networks deployed on edge-computing hardware);
- Spatial mapping and cluster-level georeferencing, enabling growers to visualize crack-risk zones overlaid on vineyard maps;
- Integration with environmental sensor networks (weather stations, soil-moisture probes, sap-flow sensors) to model crack risk as a function of both berry physiology and environmental stress;
- Automated alerts and treatment recommendations delivered to growers via mobile applications or farm-management software platforms.

Achieving this vision will require interdisciplinary collaboration among agricultural engineers, computer scientists, plant physiologists, and viticulture practitioners. Key technical challenges include: achieving sufficient acquisition speed to cover large vineyard areas within narrow weather windows; ensuring robustness to uncontrolled illumination (early morning, late afternoon, cloudy vs. sunny conditions); minimizing false-positive rates to avoid alert fatigue; and validating that early interventions triggered by spectral detection genuinely reduce losses relative to current practice.

Beyond grapes, the spectral crack-detection framework developed here is potentially generalizable to other fruit crops exhibiting similar cracking disorders—cherries, tomatoes, pomegranates, apples, and citrus. Each crop presents distinct spectral and morphological characteristics, but the underlying physiological mechanisms (cuticle failure, turgor imbalance, cellular dehydration) are shared. Demonstrating transferability across crops would position hyperspectral crack sensing as a broadly applicable precision-horticulture technology.

Finally, economic modeling remains an underexplored dimension. Quantifying the cost-benefit trade-off between sensor deployment costs (hardware, data management, operator

training) and realized reductions in crop losses would inform adoption decisions by commercial growers and provide a basis for evaluating return on investment. Preliminary estimates suggest that even modest reductions in cracking-related losses (5–10 % yield recovery) would justify sensor costs in high-value table grape operations, but rigorous field trials with paired treated-versus-control vineyard blocks are needed to validate these projections.

7.7 Final Concluding Statement

This thesis has demonstrated that hyperspectral imaging in the visible–near-infrared range, combined with machine learning and spatial aggregation strategies, can detect grape cracking under realistic field conditions—including at early developmental stages when intervention is most valuable. The work advances the state of knowledge in precision viticulture by establishing both the scientific foundation for spectral crack sensing and a practical framework for translating pixel-level classification accuracy into operationally useful system-level decisions.

The significance of these findings extends beyond the specific application to table grapes. This research exemplifies the broader potential of proximal hyperspectral sensing to measure sub-visual physiological changes in plant tissue, bridging the gap between laboratory spectroscopy and field-deployable agricultural technology. By addressing the methodological challenges inherent in moving from controlled spectral measurements to complex natural scenes—mixed pixels, illumination variability, background clutter—the work contributes generalizable insights applicable to disease detection, stress monitoring, and quality assessment across diverse crops and horticultural systems.

At the same time, the documented performance gaps between early-stage and late-stage detection, and between pixel-level and system-level inference, underscore the reality that agricultural sensing operates under constraints fundamentally different from those of controlled laboratory environments. Robust field deployment requires not only excellent algorithms but also careful attention to sensor design, spatial processing, and the integration of spectral information with agronomic context.

Looking forward, the convergence of hyperspectral imaging, machine learning, and autonomous robotic platforms promises to transform viticulture from reactive damage management toward proactive, data-driven crop stewardship. The wavelength-optimized multispectral sensors validated here, the spatial aggregation pipelines demonstrated to handle field complexity, and the quantitative performance benchmarks established under realistic test conditions provide a foundation upon which next-generation precision viticulture systems can be built.

Grape cracking represents a persistent economic challenge for the global viticulture industry, responsible for multi-million-dollar annual losses and constraining the expansion

of susceptible but high-value cultivars. If the early-detection capabilities demonstrated in this research can be translated into operational monitoring systems, the potential impact—measured in reduced losses, improved fruit quality, and enhanced grower decision support—is substantial. This thesis takes a foundational step toward that goal, establishing that the spectral signatures of cracking are measurable, learnable, and actionable under field conditions. The path from research prototype to commercial deployment remains long, but the direction is clear and the destination, achievable.

Bibliography

Abade, A., et al. (2025). From spectrum to yield: Advances in crop photosynthesis with hyperspectral imaging. *Photosynthetica*, *63*(2). https://doi.org/10.32615/ps.2025.012

Ahmed, N., & Shakoor, N. (2025). Advancing agriculture through iot, big data, and ai: A review of smart technologies enabling sustainability. *Smart Agricultural Technology*, *10*, 100848. https://doi.org/10.1016/j.atech.2025.100848

Akter, T., Faqeerzada, M. A., Kim, Y., Pahlawan, M. F. R., Aline, U., Kim, H., Kim, H., & Cho, B.-K. (2025). Hyperspectral imaging with multivariate analysis for detection of exterior flaws for quality evaluation of apples and pears. *Postharvest Biology and Technology*, *223*, 113453. https://doi.org/10.1016/j.postharvbio.2025.113453

Alchanatis, V., et al. (2022). *High throughput real-time monitoring and prediction of fruit cracking by utilising and upscaling sensing and digital data technologies* (tech. rep.) (Research and Innovation Action (RIA), HORIZON-CL6-2022-GOVERNANCE-01-11). Horizon Europe.

Attri, I., Awasthi, L. K., Sharma, T. P., & Rathee, P. (2023). A review of deep learning techniques used in agriculture. *Ecological Informatics*, *77*, 102217. https://doi.org/10.1016/j.ecoinf.2023.102217

Author, A., et al. (2022). Assessment of scarlotta seedless table grape maturation and quality. *Foods*, *11*(5), 663.

Author, B., et al. (2024). Impact of storage temperature on postharvest quality of scarlotta seedless. *Postharvest Biology and Technology*, *215*, 113013.

Ball, S. R. (2007). *Field guide to spectroscopy*. SPIE Press.

Barnes, R. J., Dhanoa, M. S., & Lister, S. J. (1989). Standard normal variate transformation and de-trending of near-infrared diffuse reflectance spectra. *Applied Spectroscopy*, *43*(5), 772–777.

Behmann, J., Acebron, K., Emin, D., Bennertz, S., Matsubara, S., Thomas, S., Bohnenkamp, D., Kuska, M. T., Jussila, J., Salo, H., et al. (2018). Specim iq: Evaluation of a new, miniaturized handheld hyperspectral camera and its application for plant phenotyping and disease detection. *Sensors*, *18*(2), 441.

Benelli, A., Cevoli, C., Fabbri, A., & Ragni, L. (2020). Hyperspectral imaging and mini-video devices for non-destructive analysis of fruit quality: A review. *Biosystems Engineering*, *192*, 142–152. https://doi.org/10.1016/j.biosystemseng.2020.01.018

Benos, L., Tagarakis, A. C., Dolias, G., Berruto, R., Kateris, D., & Bochtis, D. (2021). Machine learning in agriculture: A comprehensive updated review. *Sensors*, *21*(11), 3758.

Bhargava, A., Sachdeva, A., Sharma, K., Alsharif, M. H., Uthansakul, P., & Uthansakul, M. (2024). Hyperspectral imaging and its applications: A review. *Heliyon*, *10*(12), e33208. https://doi.org/10.1016/j.heliyon.2024.e33208

Bioucas-Dias, J. M., Plaza, A., Camps-Valls, G., et al. (2013). Hyperspectral remote sensing data analysis and future challenges. *IEEE Geoscience and Remote Sensing Magazine*, *1*(2), 6–36.

Blackburn, G. A. (2007). Hyperspectral remote sensing of plant pigments. *Journal of experimental botany*, *58*(4), 855–867.

Cao, Z., Sun, S., & Bao, X. (2025). A review of computer vision and deep learning applications in crop growth management. *Applied Sciences*, *15*(15), 8438.

Castellarin, S. D., & other. (2016). Characterization of major ripening events during softening in grape and their relationship with growth. *Journal of Experimental Botany*, *67*(3), 709–722.

Chang, B.-M., & Keller, M. (2021). Cuticle and skin cell walls have common and unique roles in grape berry splitting. *Horticulture Research*, *8*, 168. https://doi.org/10.1038/s41438-021-00602-2

Chang, B.-M., Zhang, Y., & Keller, M. (2019). Softening at the onset of grape ripening alters fruit rheological properties and decreases splitting resistance. *Planta*, *250*, 1293–1305. https://doi.org/10.1007/s00425-019-03226-y

Chen, L., Wu, Y., Yang, N., & Sun, Z. (2025). Advances in hyperspectral and diffraction imaging for agricultural applications. *Agriculture*, *15*.

Chen, T., & Guestrin, C. (2016). Xgboost: A scalable tree boosting system. *Proceedings of the 22nd ACM SIGKDD International Conference on Knowledge Discovery and Data Mining*, 785–794.

Chen, Z., Hao, Y., Liu, Q., Liu, Y., Zhu, M., & Xiao, L. (2024). Deep learning for hyperspectral image classification: A critical evaluation via mutation testing. *Remote Sensing*, *16*(24), 4695. https://doi.org/10.3390/rs16244695

Cover, T. M., & Thomas, J. A. (2006). *Elements of information theory*. Wiley.

Dhanya, V., Subeesh, A., Kushwaha, N., Vishwakarma, D. K., Nagesh Kumar, T., Ritika, G., & Singh, A. (2022). Deep learning based computer vision approaches for smart agricultural applications. *Artificial Intelligence in Agriculture*, *6*, 211–229. https://doi.org/10.1016/j.aiia.2022.09.007

Ding, K., et al. (2023). Hyperspectral band selection based on mutual information and recursive feature elimination for crop classification. *Computers and Electronics in Agriculture*, *204*, 107538.

Dong, C., Yang, T., Liu, L., Wei, Z., Shi, C., & Gao, D. (2025). Early identification of apple bitter pit using hyperspectral imaging technology. *Applied Food Research*, *5*(2), 101166. https://doi.org/10.1016/j.afres.2025.101166

Emmons, C. L., & Scott, J. W. (1998). Ultrastructural and anatomical factors associated with resistance to cuticle cracking in tomato. *International Journal of Plant Sciences*, *159*, 14–22.

Fass, E., Shlomi, E., Ziv, C., Glikman, O., & Helman, D. (2025). Machine learning models based on hyperspectral imaging for pre-harvest tomato fruit quality monitoring. *Computers and Electronics in Agriculture*, *229*, 109788. https://doi.org/10.1016/j.compag.2024.109788

García-Vera, A., Polochè-Arango, F., & Gutiérrez-Bernal, A. (2024). Hyperspectral image analysis and machine learning techniques for crop disease detection and identification: A review. *Sustainability*, *16*(14), 6064. https://doi.org/10.3390/su16146064

Gewali, U. B., Monteiro, S. T., & Saber, E. (2022). Machine learning based hyperspectral image analysis: A survey [Published in IEEE Transactions on Geoscience and Remote Sensing in 2022]. *arXiv preprint arXiv:1802.08765*, *60*, 1–20.

Ghazal, S., Munir, A., & Qureshi, W. S. (2024). Computer vision in smart agriculture and precision farming: Techniques and applications. *Artificial Intelligence in Agriculture*, *13*, 64–83.

Gu, Q., Li, Z., & Han, J. (2012). Generalized fisher score for feature selection. *arXiv preprint arXiv:1202.3725*.

Guirao, A., García-Pastor, M. E., Solana-Guilabert, A., Valverde, J. M., & Martínez-Romero, D. (2025). Enhancing calcium transport in table grapes using sorbitol: A sustainable strategy for promoting fruit quality. *Horticulturae*, *11*(11). https://doi.org/10.3390/horticulturae11111320

Haghbin, N., Bakhshipour, A., Zareiforoush, H., & Mousanejad, S. (2023). Non-destructive pre-symptomatic detection of gray mold infection in kiwifruit using hyperspectral data and chemometrics. *Plant Methods*, *19*(1), 53. https://doi.org/10.1186/s13007-023-01032-y

Hall, M. E., Loeb, G., Cadle-Davidson, L., et al. (2018). Grape sour rot: A four-way interaction involving the host, yeast, acetic acid bacteria, and insects. *Phytopathology*, *108*, 1429–1442.

Hasanzadeh, B., Abbaspour-Gilandeh, Y., Soltani-Nazarloo, A., Hernández-Hernández, M., Gallardo-Bernal, I., & Hernández-Hernández, J. L. (2022). Non-destructive detection of fruit quality parameters using hyperspectral imaging, multiple regres-

sion analysis and artificial intelligence. *Horticulturae*, *8*(7), 598. https://doi.org/10.3390/horticulturae8070598

Hong, D., Li, C., Yokoya, N., Zhang, B., Jia, X., Plaza, A., Gamba, P., Benediktsson, J. A., & Chanussot, J. (2025). Hyperspectral imaging. https://arxiv.org/abs/2508.08107

Imaging, S. S. (2024). *What is hyperspectral imaging?: A comprehensive guide* (tech. rep.). Specim, Spectral Imaging Ltd. https://www.specim.com/technology/what-is-hyperspectral-imaging/

Kaltenborn, J., et al. (2025). Data splitting to avoid information leakage with datasail. *Scientific Reports*, *15*(1), 1–15.

Kanwal, N., Kämper, W., Farrar, M. B., Tootoonchy, M., Lynch, C., Nichols, J., Wallace, H. M., Trueman, S. J., & Hosseini Bai, S. (2025). Rapid assessment of lychee and mango fruit quality using hyperspectral imaging. *LWT*, *224*, 117833. https://doi.org/10.1016/j.lwt.2025.117833

Karantzi, A. D., Kafkaletou, M., Tsaniklidis, G., Bai, J., Christopoulos, M. V., Fanourakis, D., & Tsantili, E. (2021). Preharvest foliar salicylic acid sprays reduce cracking of fig fruit at harvest. *Applied Sciences*, *11*(23). https://doi.org/10.3390/app112311374

Kaufman, S., Rosset, S., & Perlich, C. (2012). Leakage in data mining: Formulation, detection, and avoidance. *ACM Transactions on Knowledge Discovery from Data*, *6*(4), 1–21.

Khadivi-Khub, A. (2014). Physiological and genetic factors influencing fruit cracking. *Acta Physiologiae Plantarum*, *36*, 1713–1727.

Khaled, A. Y., Ekramirad, N., Donohue, K. D., Villanueva, R. T., & Adedeji, A. A. (2023). Non-destructive hyperspectral imaging and machine learning-based predictive models for physicochemical quality attributes of apples during storage as affected by codling moth infestation. *Agriculture*, *13*(5), 1086. https://doi.org/10.3390/agriculture13051086

Krisnawijaya, N. N. K., Tekinerdogan, B., Catal, C., & van der Tol, R. (2022). Data analytics platforms for agricultural systems: A systematic literature review. *Computers and Electronics in Agriculture*, *195*, 106813.

La Spada, P., Continella, A., Dominguez, E., Heredia, A., & Gentile, A. (2024). Improving cuticle thickness and quality traits in table grape cv. 'italia' using pre-harvest treatments. *Plants*, *13*(17). https://doi.org/10.3390/plants13172400

Li, S., et al. (2023). Information leakage in deep learning-based hyperspectral image classification: A survey. *Remote Sensing*, *15*(15), 3793.

Liang, Y., Li, Z., Shi, J., Zhang, N., Qin, Z., Du, L., Zhai, X., Shen, T., Zhang, R., Zou, X., & Huang, X. (2025). Advances in hyperspectral imaging technology for grain quality and safety detection: A review. *Foods*, *14*(17). https://doi.org/10.3390/foods14172977

Lichter, A., Kaplunov, T., Zutahy, Y., et al. (2014). Effects of gibberellin on cracking and postharvest quality of the seeded table grape 'zainy'. *Acta Horticulturae*, *1079*, 265–271.

Liu, Y., Zhang, H., & Wang, J. (2023). Early detection of plant physiological stress using VIS–NIR hyperspectral imaging. *Sensors*, *23*. https://doi.org/10.3390/s23083915

Liu, Y., et al. (2022). Feature selection for hyperspectral image classification: A survey. *Sensors*, *22*(10), 3782.

Mahlein, A.-K. (2016). Plant disease detection by imaging sensors–parallels and specific demands for precision agriculture and plant phenotyping. *Plant Disease*, *100*(2), 241–251.

Mehta, N. (2018). *Hyperspectral imaging cameras in rapid detection and potential diagnosis of agricultural crop threats* (tech. rep.). HinaLea Imaging. https://hinalea.ai/wp-content/uploads/2018/03/Agriculture-in-Hyperspectral-Imaging-Whitepaper.pdf

Menze, B. H., Kelm, B. M., Masuch, R., Himmelreich, U., Bachert, P., Petrich, W., & Hamprecht, F. A. (2009). A comparison of random forest and its gini importance with standard chemometric methods for the feature selection and classification of spectral data. *BMC Bioinformatics*, *10*(1), 213.

Mgendi, G. (2024). Unlocking the potential of precision agriculture for sustainable farming. *Discover Agriculture*, *2*(1), 87.

Min, D., Zhao, J., Bodner, G., Ali, M., Li, F., Zhang, X., & Rewald, B. (2023). Early decay detection in fruit by hyperspectral imaging–principles and application potential. *Food Control*, *152*, 109830. https://doi.org/10.1016/j.foodcont.2023.109830

Mishra, P., Asaari, M. S. M., Herrero-Langreo, A., Lohumi, S., Diezma, B., & Scheunders, P. (2017). Close range hyperspectral imaging of plants: A review. *Biosystems Engineering*, *164*, 49–67.

Moeini, A., & Wang, S. (2018). A dc link sensor-less voltage balancing technique for cascaded h-bridge multilevel converters with asymmetric selective harmonic current mitigation-pwm. *IEEE Transactions on Power Electronics*, *33*(9), 7571–7581. https://doi.org/10.1109/TPEL.2017.2770141

Monteiro, H. S. A., Tecchio, M. A., Brito, S. d. N. S., Neto, F. J. D., Sánchez, C. A. P. C., Alonso, J. C., Feliciano, D. E. F., Maniero, C. R., Cunha, P. H. H., & Silva, M. d. S. (2025). Phenological development, thermal requirement, and quality of 'brs núbia' (vitis vinifera l. x vitis labrusca l.) grapes on different rootstocks. *Horticulturae*, *11*(5). https://doi.org/10.3390/horticulturae11050466

Ou, Y., Yan, J., Liang, Z., & Zhang, B. (2024). Hyperspectral imaging combined with deep learning for the early detection of strawberry leaf gray mold disease. *Agronomy*, *14*(11), 2694. https://doi.org/10.3390/agronomy14112694

Owoyemi, A., Balaklav, M., Kochanek, B., Porat, R., Koenigstein, N., Salzer, Y., & Lichter, A. (2024). Deviations from optimal storage temperature and its impact on postharvest quality of table grape cv. scarlotta seedless. *Postharvest Biology and Technology*, *215*, 113013. https://doi.org/10.1016/j.postharvbio.2024.113013

Patrício, D. I., & Rieder, R. (2018). Computer vision and artificial intelligence in precision agriculture for grain crops: A systematic review. *Computers and electronics in agriculture*, *153*, 69–81.

Peschel, S., & Knoche, M. (2005). Characterization of microcracks in the cuticle of developing sweet cherry fruit. *Journal of the American Society for Horticultural Science*, *130*, 487–495.

Ram, B. G., Oduor, P., Igathinathane, C., Howatt, K., & Sun, X. (2024). A systematic review of hyperspectral imaging in precision agriculture: Analysis of its current state and future prospects. *Computers and Electronics in Agriculture*, *222*, 109037. https://doi.org/10.1016/j.compag.2024.109037

Ravi, N., Gabeur, V., Hu, Y.-T., Hu, R., Ryali, C., Ma, T., Khedr, H., Rädle, R., Rolland, C., Gustafson, L., et al. (2024). Sam 2: Segment anything in images and videos. *arXiv preprint arXiv:2408.00714*.

Rousseeuw, P. J., & Van Driessen, K. (1999). A fast algorithm for the minimum covariance determinant estimator. *Technometrics*, *41*(3), 212–223. https://doi.org/10.1080/00401706.1999.10485670

Santos, M., Egea-Cortines, M., Gonçalves, B., & Matos, M. (2023). Molecular mechanisms involved in fruit cracking: A review. *Frontiers in Plant Science*, *14*, 1130857.

Seo, H.-J., Sawant, S. S., & Song, J. (2022). Fruit cracking in pears: Its cause and management—a review. *Agronomy*, *12*(10). https://doi.org/10.3390/agronomy12102437

Shaw, G., & Manolakis, D. (2002). *Hyperspectral imaging remote sensing*. John Wiley & Sons.

Soussi, A., Zero, E., Sacile, R., Trinchero, D., & Fossa, M. (2024). Smart sensors and smart data for precision agriculture: A review. *Sensors*, *24*(8), 2647.

Späth, N., et al. (2024). Separating surface reflectance from volume reflectance in medical hyperspectral imaging. *Journal of Biomedical Optics*, *29*(8), 086001.

Sun, Q., Li, X., & Zhao, Y. (2024). VIS–NIR hyperspectral imaging for internal quality assessment of fruits. *Postharvest Biology and Technology*. https://doi.org/10.1016/j.postharvbio.2024.112095

Sun, T., Xu, R., Zhang, G.-x., Li, X.-y., Fan, S.-d., & Wang, X. (2020). Non-destructive determination of moisture content of single barley grain using hyperspectral imaging. *Spectrochimica Acta Part A: Molecular and Biomolecular Spectroscopy*, *226*, 117623.

Thenkarail, P. S., Lyon, J. G., & Huete, A. (2016). *Hyperspectral remote sensing of vegetation*. CRC Press.

Tian, H., Wang, T., Liu, Y., Qiao, X., & Li, Y. (2020). Computer vision technology in agricultural automation—a review. *Information processing in agriculture*, *7*(1), 1–19.

Tian, P., Meng, Q., Wu, Z., Lin, J., Huang, X., Zhu, H., Zhou, X., Qiu, Z., Huang, Y., & Li, Y. (2023). Detection of mango soluble solid content using hyperspectral imaging technology. *Infrared Physics & Technology*, *129*, 104576. https://doi.org/10.1016/j.infrared.2023.104576

Valme, D., Rassõlkin, A., & Liyanage, D. C. (2025). From adas to material-informed inspection: Review of hyperspectral imaging applications on mobile ground robots. *Sensors*, *25*(8), 2346. https://doi.org/10.3390/s25082346

Vergara, J. R., & Estévez, P. A. (2014). A review of feature selection methods based on mutual information. *Neural Computing and Applications*, *24*(1), 175–186.

Vignati, S., Tugnolo, A., Giovenzana, V., Pampuri, A., Casson, A., Guidetti, R., & Beghi, R. (2023). Hyperspectral imaging for fresh-cut fruit and vegetable quality assessment: Basic concepts and applications. *Applied Sciences*, *13*(17). https://doi.org/10.3390/app13179740

Wang, B., Yang, H., Zhang, S., & Li, L. (2023). Detection of defective features in cerasus humilis fruit based on hyperspectral imaging technology. *Applied Sciences*, *13*(5). https://doi.org/10.3390/app13053279

Wang, C., Li, X., Zhang, Z., Luo, X., Cai, J., & Wang, A. (2025). Nondestructive quality detection of characteristic fruits based on vis/nir spectroscopy: Principles, systems, and applications. *Agriculture*, *15*(20). https://doi.org/10.3390/agriculture15202167

Wang, T., & Zhao, L. (2024). Hyperspectral imaging for monitoring plant physiological status. *Frontiers in Plant Science*. https://doi.org/10.3389/fpls.2024.1298743

Xu, J., Chen, L., Dong, J., Jiang, L., & Hong, L. (2025). Overview of fruit cracking in sweet cherry (prunus avium l.): Causes, testing methods, mitigation strategies, and research perspectives. *Frontiers in Sustainable Food Systems*, *9*, 1534778.

Yang, C., Guo, Z., Fernandes Barbin, D., Dai, Z., Watson, N., Povey, M., & Zou, X. (2025). Hyperspectral imaging and deep learning for quality and safety inspection of fruits and vegetables: A review. *Journal of Agricultural and Food Chemistry*, *73*(17), 10019–10035. https://doi.org/10.1021/acs.jafc.4c11492

Yu, J., Li, J., Hong, Z., Zeng, Q., Fu, Y., Deng, R., Xu, K., Huang, Z., & Zhu, M. (2025). Vvpip1;1 plays a role in grape berry cracking by regulating water uptake. *Horticultural Plant Journal*, *11*(4), 1506–1516. https://doi.org/10.1016/j.hpj.2024.07.010

Zhang, C., Wang, Q., He, H., Wu, Y., Shan, W., & Liu, H. (2025). Postharvest preservation strategies for table grapes: A comprehensive review from practical methods to future developments. *Plants*, *14*(16). https://doi.org/10.3390/plants14162462

Zhang, J., et al. (2021). Hyperspectral band selection for tobacco disease identification based on fisher score. *Spectroscopy and Spectral Analysis*, *41*(4), 1234–1240.

Zhang, X., Li, Y., Chen, H., & Wang, Q. (2024). Application of hyperspectral imaging in fruit quality and safety assessment. *Frontiers in Plant Science*, *15*, 1432120. https://doi.org/10.3389/fpls.2024.1432120

Zhang, X., Vinatzer, B. A., & Li, S. (2024). Hyperspectral imaging analysis for early detection of tomato bacterial leaf spot disease. *Scientific Reports*, *14*(1), 27666. https://doi.org/10.1038/s41598-024-78650-6

Zhang, Y., Chen, J., & Liu, Q. (2022). Physiological interpretation of VIS–NIR hyperspectral reflectance in vegetation. *Remote Sensing*, *14*. https://doi.org/10.3390/rs14215345

Zhang, Y., Li, X., Wang, M., Xu, T., Huang, K., Sun, Y., Yuan, Q., Lei, X., Qi, Y., & Lv, X. (2024). Early detection and lesion visualization of pear leaf anthracnose based on multi-source feature fusion of hyperspectral imaging. *Frontiers in Plant Science*, *15*, 1461855. https://doi.org/10.3389/fpls.2024.1461855

Zhang, Z., Cheng, H., Chen, M., Zhang, L., Cheng, Y., Geng, W., & Guan, J. (2024). Detection of pear quality using hyperspectral imaging technology and machine learning analysis. *Foods*, *13*(23), 3956. https://doi.org/10.3390/foods13233956

Zhu, H., Qin, S., Liang, S., Su, M., Wang, P., & He, Y. (2025). Hyperspectral imaging and machine learning for quality assessment of apples with different bagging types. *Spectrochimica Acta Part A: Molecular and Biomolecular Spectroscopy*, *343*, 126443. https://doi.org/10.1016/j.saa.2025.126443

Zwinkels, J. C. (2015). Spectrophotometry. In *Encyclopedia of color science and technology*. Springer. https://doi.org/10.1007/978-1-4419-8071-7_221